Molecular Organisation in “de Vries” Smectic Liquid Crystals: Characterisation and Theory

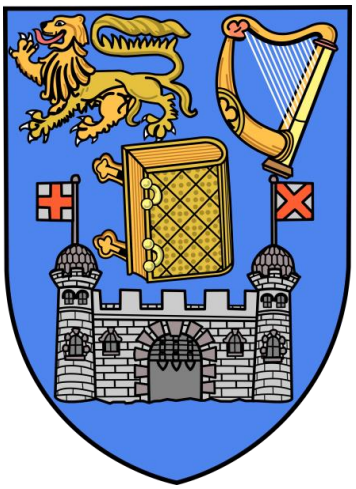

by

Vigneshwaran Swaminathan

A thesis submitted for the degree of Doctor of Philosophy

Laboratory of Advanced Electronic Materials

Department of Electronic and Electrical Engineering

Trinity College Dublin

The University of Dublin

July 2018

Declaration of Authorship

I, Vigneshwaran Swaminathan declare that this thesis is written by me and is entirely my own work, unless stated otherwise. The use of any author's work has been duly acknowledged at their point of use. I declare that:

- This thesis has not been submitted as an exercise for a degree at this or any other university.
- I agree to deposit this thesis in the University's open access institutional repository or allow the Library to do so on my behalf, subject to Irish Copyrights Legislation and Trinity College Library conditions of use and acknowledgement.

Sign: _____

Date: _____

Acknowledgements

My journey towards Ph.D. started from 20th of November 2014 by successfully securing a position in Trinity College Dublin. This journey would not have been possible without the support and help of so many people.

First and foremost I am heartily thankful to my supervisor, **Prof. J. K. Vij**, whose constant support and guidance from the beginning till the end helped me in every aspect of my research. I am always grateful to my supervisor for providing the opportunity to peruse Ph.D. abroad.

I have been blessed with wonderful post-docs and colleagues in my group whose support is immeasurable. My deepest gratitude to **Dr. Yu. P. Panarin** for his help and support. I am very grateful to **Dr. V. Panov** who has made his contribution to my Ph.D. in every possible way by passing on his knowledge. I am very thankful to **Dr. S. P. Sreenilayam** for her constant support and providing a family like environment in the lab. I am very thankful to **Prof. A. Kocot** for his valuable support. I would like to thank **Dr. T. Perova** and **Prof. A D. L. Chandani** for their support and care. I am very thankful to **Dr. N. Yadav** for her constant motivation and support as a friend.

I would like to thank the whole Electronic and Electrical Engineering department. I am very thankful to my co-supervisor **Prof. W. Dowling** for his support. I am grateful to the department head **Prof. A. Kokaram** for his support. I would like to thank **Mr. S. Hunt** for his help and support.

I am very thankful to Trinity College Dublin and Science Foundation Ireland for the Postgraduate studentship award under the US-Ireland Research and Development partnership program project 13/US/I2866. I am very thankful to **Prof.**

S. Kumar for coordinating the project and for his contribution. My deepest gratitude to the Queens University Belfast Chemistry group for providing the liquid crystal samples. I am thankful to **Prof. E. Gorecka** for providing the access to X-ray equipment.

Finally, this thesis would not have been existed without the love and care from my family and friends. I am very thankful to my parents and sisters for their constant love and care. I am heartily thankful to my father **Mr. S. Swaminathan** for his never-ending encouragement. I am thankful to all my friends back in India for their love.

I would like to thank 'Dublin Tamil Makkal' group for providing unbelievable support and care throughout my Ph.D. I owe a special thanks to **Dr. A. Vasudevan** and **Dr. R. Sridharan** for the love and care during the final stage of my Ph. D. My special thanks to all my friends in Dublin.

Summary

The study of anomalous temperature dependence of smectic layer thickness began some fifty years ago. Liquid crystals exhibiting such properties were later classified as de Vries type smectic liquid crystals, due to the seminal contributions of the American crystallographer Adriaan de Vries. In the recent years de Vries type liquid crystals attained a renewed focus as promising candidates for the ferroelectric liquid crystal based device applications. In this thesis, I have carried out a number of experimental and theoretical approaches to understand the nature of de Vries type liquid crystals. A brief summary of the research work undertaken is described below:

It is known that the cost effective and efficient way of achieving ferroelectricity in the liquid crystalline system is by adding a chiral dipolar additive to an achiral liquid crystalline material. The effect of chiral doping in the achiral de Vries type liquid crystals is studied here. The de Vries characteristics of the mixtures have been investigated using various experimental techniques. The chiral dopant is mixed in varying weight percentages to study the influence of doping as function of concentration (Chapter 3).

As a result of the continued research on de Vries type liquid crystals there are few classic examples of chiral de Vries smectic liquid crystals in the literature. Therefore as a starting point, the study of two well-known de Vries materials is presented. We adopt the famous electro-optic model from the literature in order to investigate these two materials. This electro-optic modelling displays the validity of the diffuse cone theory originally proposed by de Vries. These materials were also studied using infra-red spectroscopy. It is shown that the model under consideration

can also be used to fit the data obtained from infra-red spectroscopic measurements (Chapter 4).

Based on the knowledge of chemical structure of the de Vries materials our chemistry partners from Belfast designed a number of novel structures. The following work in this thesis is entirely based on such new compounds. We investigate one of the compounds exhibiting de Vries characteristic based on phenyl-pyrimidine benzoate core. It is shown that the temperature dependent physical parameters such as the birefringence and the layer thickness show a characteristic trend reversal. Based on these experimental facts we modify the existing electro-optic model. As a result a good fit to the experimental data is obtained. Later, another epoxyhexoxy backbone based compound exhibiting de Vries characteristics is studied. Here we propose a new mean-field based electro-optic model addressing the shortcomings of the previous model (Chapter 5).

A comparative study of the two new chiral liquid crystals is carried out. A detailed high resolution measurements shows that both liquid crystals show excellent de Vries type liquid crystalline properties. A simple method is shown to correct the optical thickness obtained from the free standing film (bulk) to the X-ray smectic layer thickness; from the results of materials mentioned above. As a final refinement of the electro-optic model we upgrade the previous models to produce more physical and meaningful results. From the updated model the orientational order parameter is estimated for the liquid crystalline systems under study. It is shown that, the temperature dependence of molecular organisation in de Vries smectic liquid crystal is responsible for the characteristic huge electro-optic effect (Chapter 6).

Abbreviations

LC	Liquid Crystals
LCD	Liquid Crystal Display
Iso	Isotropic Phase
Cryst	Crystalline Solid
SmA	Smectic A phase
SmC	Smectic C phase
SmA*/C*	Chiral Smectic Phase
N*	Chiral Nematic phase
FLC	Ferroelectric Liquid Crystal
EO	Electro-Optics
LCoS	Liquid Crystal on Silicon
$\boldsymbol{P_S}$	Spontaneous Polarisation
POM	Polarising Optical Microscope
ITO	Indium Tin Oxide
DSC	Differential Scanning Calorimetry
XRD	X-ray Diffraction
2D	Two Dimensional
3D	Three Dimensional
FSF	Free Standing Film
ATP	Automated Time-resolved Polarimetry
LED	Light Emitting Diode
DAQ	Data Acquisition Board
DC	Direct Current
AC	Alternating Current

PC	Personal Computer
SSFLC	Surface Stabilised Ferroelectric Liquid Crystal
NMR	Nuclear Magnetic Resonance
DFT	Density Functional Theory
CCD	Charge Coupled Device
GLD	Generalised Langevin-Debye
ODF	Orientational Distribution Function
IR	Infra-Red
MCT	Mercury Cadmium Telluride
MFLD	Mean-Field Langevin-Debye
MSLD	Maier-Saupe Langevin-Debye

Table of Contents

List of Figures

List of Tables

Chapter 1

1. Introduction

1.1 Introduction to Liquid Crystals

Fundamentally, matter in nature exists in three different states (or phases). Based on the mobility of individual atoms or molecules matter is categorised as solid, liquid or gas. Though characteristics of these three major states of matter are well defined, boundary between these states might exhibit some anomalies. Several intermediate phases have been identified especially in the last 30 years. Liquid Crystal (LC) is one of the intermediate states of matter that appears between states of solid and liquid in some materials [1]. Mechanical and symmetry properties of a LC are intermediate between those of a conventional liquid and of a crystalline solid. The fluidity of a liquid crystal resembles that of a liquid while properties like, molecular ordering and anisotropy are those of a solid [2]. Liquid crystal phases are otherwise known as mesophase (meso, 'middle') and the LC molecules can be called as mesogens.

History of the LCs began in 1880's; when an Austrian botanical physiologist Friedrich Reinitzer [3] while studying the properties of cholesteryl benzonate observed that, unlike other materials cholesteryl benzonate showed two different melting points, a cloudy liquid state appeared before a clear transparent liquid as increasing the temperature. In order to understand this unusual phenomenon, he contacted the German physicist, Otto Lehmann. Lehmann found that these materials possess mechanical properties of a liquid (it flows like a liquid), but also exhibits some physical properties of solid crystal like the optical anisotropy, etc. Eventually Lehmann realised that the cloudy liquid was a new state of matter and coined the name "Liquid Crystal". This new idea challenged the scientific community of the time. However, some scientists claimed that the newly-discovered state probably was just a mixture of solid and liquid components. In 1930's several definitive theories

and experiments supported the 'liquid crystal' as a new state of matter; at the same time within this state of matter, many types of liquid crystalline phases has now been discovered.

LCs can broadly be classified into two types: lyotropic and thermotropic. Lyotropic LCs depend mainly on the solvent's concentration, temperature and pressure while on the other hand, thermotropic LCs exhibit different phases purely as a function of temperature and the latter have greater impact in technological applications [4]. In this thesis we mainly focus on studying the various properties of thermotropic LCs.

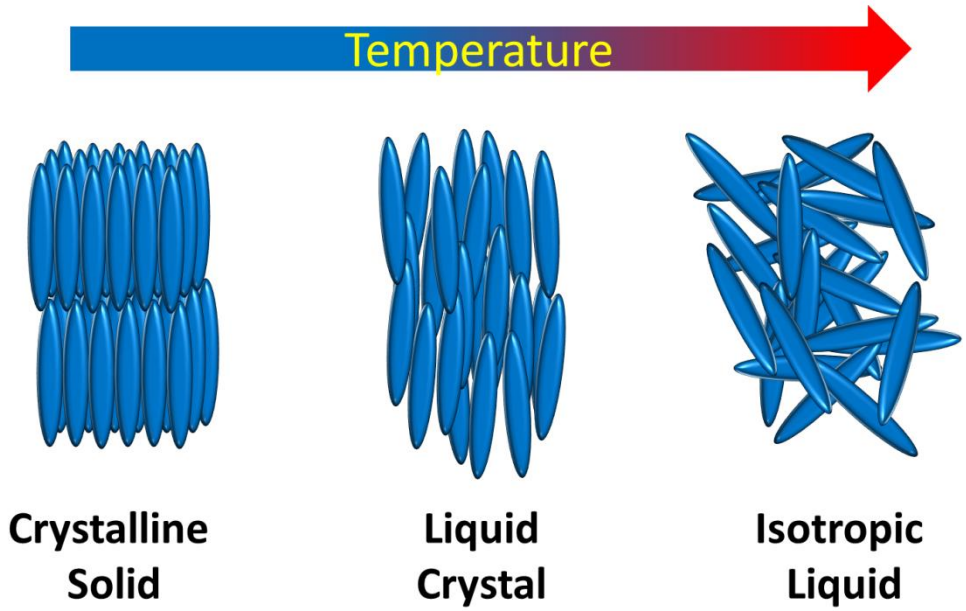

Figure 1.1 Schematic representation of solid, liquid and the intermediate LC states of matter.

The macroscopic properties of LCs are directly linked to their microscopic arrangements; also the molecular shape has large impact on the formation of the state of LC [5]. Based on their molecular shape the mesogens can be categorised as (i)

calamatic/rod-shaped, (ii) bent-core/banana-shaped, (iii) discotics, (iv) bimesogens or dimer/nunchaku-shaped LCs.

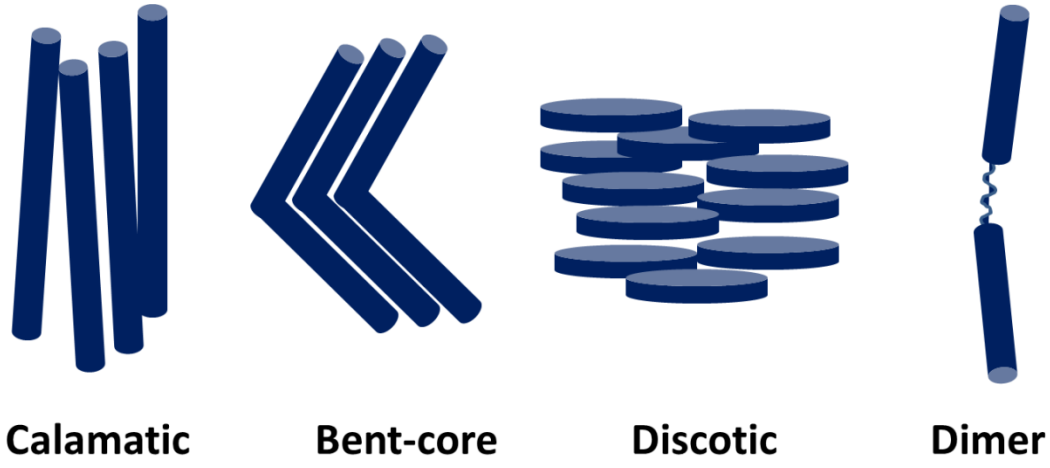

Figure 1.2 Molecular shape dependent LC phases

1.2 Different phases of liquid crystals

Different liquid crystal phases can generally be characterised on the basis of molecular ordering. Brief explanations for a few important phases of LC are given below:

1.2.1 Nematic phase:

The nematic liquid crystal phase is formed when the long axis of the constituent molecules on the average point towards a specific direction, molecules align themselves approximately parallel to each other in space (i.e. it exhibits orientational order) [5]. A dimensionless unit vector can represent average local orientation of molecules within the medium. This vector is known as the director and usually denoted by the symbol $\vec{n}$ [2]. Further details of the definitions of director and order parameter are given in the following section.

If the constituent molecules having a chiral centre forms a nematic phase known as cholesteric or chiral nematic (N*) phase, here the director is twisted in space and forms a helical or a spiral structure. Cholesteric nematic phase can be characterised by a physical parameter called the 'pitch' (*p*). The pitch is defined as the distance required for the director to undergo one complete rotation in space, along the helical axis (Figure 1.3).

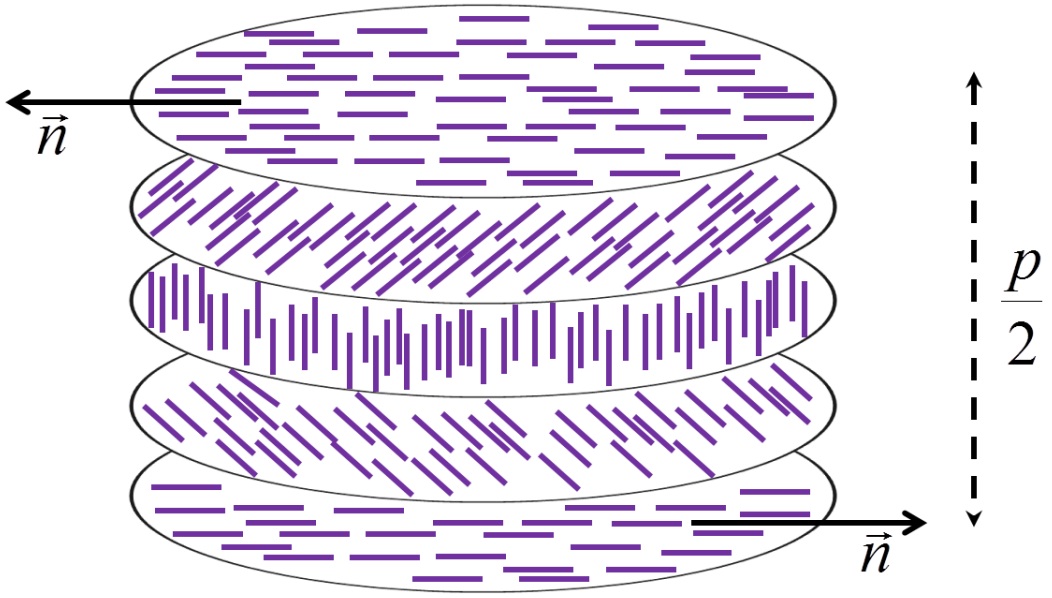

Figure 1.3 Schematic representation of cholesteric nematic phase.

1.2.2 Smectic phase:

Smectic phase is a layered arrangement of molecules and exhibits both positional and orientational order. Molecules packed parallel to each other form a single layer. Each layer is a two dimensional fluid and thickness is of the order of the length of the molecule. This thesis focuses on to the study of calamatic smectic liquid crystals.

1.2.3 Other phases:

Blue phase: This phase is found in a narrow range of temperatures between the isotropic and the chiral nematic phase. Blue phase is optically isotropic due to its double twist packing arrangement [5].

Twist-Bent nematic phase: Bimesogens under certain conditions form highly twisted and bent phase, producing a complicated double helical structure. This phase is generally found below a conventional nematic phase on cooling for certain types of dimers and bent-core LCs. N_{TB} or Twist-Bent nematic phase is of significant current interest in the liquid crystal research community [6-9].

1.3 Applications of liquid crystals:

Liquid crystals make a significant contribution to the many areas of science, engineering and device technology. Today LCs are well known for their exceptional impact on the flat panel displays. However, their unique complexity and interesting properties offer tremendous potential for advancing the fundamental science and for laying the foundation of the ground breaking innovative applications in addition to displays. Some of the applications are being listed below:

LCD – A liquid crystal display consists of a matrix of tiny segments called pixels. The LC material is sandwiched between the two glass plates, the inside of each glass plate is coated with a conducting ITO layer, which in turn is coated with an alignment layer. LC medium can be manipulated by the electric field and this enables the LC to work as an optical shutter. Different colours can be produced with the help of colour filters. Each and every pixel in the matrix is then operated individually to display the required information.

Liquid Crystal Thermometers – Chiral nematic liquid crystals selectively reflect wavelength of light that matches the pitch length. The pitch varies as a function of temperature. By mixing different compounds, a device for a given

temperature range can be fabricated. Temperature is calibrated in terms of the reflected colours.

Optical Imaging – A liquid crystal cell is placed between two layers of a photoconductor. The conductivity of the photoconductor depends on the intensity of the incident light. Thus an electric field across the LC cell directly depends on the intensity of the light shone at a particular point. Thus a pattern is formed in the photoconductor and the LC medium based on the intensity of incident light. The signal is transmitted by enabling the electrode on which the image is recorded. This technology is still being developed and is one of the most promising areas of prospective research in the field of liquid crystals.

Other liquid crystal applications – Liquid crystals have a multitude of other applications. Some of them are listed below;

- Spatial Light modulators
- Liquid Crystal Lasing
- Liquid Crystal on Silicon (LCoS)

1.4 Physics of Liquid crystals:

1.4.1 Director and the Order parameter:

Each molecule is assumed to have the simple shape of a rod. In the given space of LC medium, a dimensionless vector '$\vec{n}$' is defined as the director this gives the preferred orientation of the long axis of the rod shaped molecule. The anisotropy of the liquid crystalline phase can be quantified using the director definition. Here β is defined as the angle between the molecular long axis 'z' and the director $\vec{n}$ (Figure 1.4). Statistical average over the second term of the Legendre polynomial

expansion of the function $\cos\beta$, gives the degree of the orientational order (i.e. order parameter) of the system.

$$S = \langle P_2 \rangle = \frac{1}{2}\langle 3\cos^2\beta - 1 \rangle \tag{1.1}$$

Mostly the order parameter is denoted as S or $\langle P_2 \rangle$. The value of the order parameter varies from 0 to 1, S = 0 infers no order. In other words it implies a complete disorder and this corresponds to the isotropic liquid phase. S = 1 defines the perfect order of the system, in which each and every molecule is aligned perfectly parallel to the director $\vec{n}$ [2]. Experimental values of the order parameters in general vary from 0.3 to 0.9 and this strongly depends on the temperature and the phase.

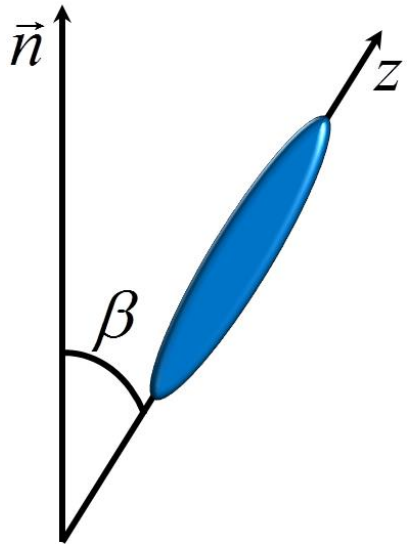

Figure 1.4 Schematic representation of molecule tilted by an angle β with the director.

Some optical and x-ray methods can be used to determine the order parameters. The order parameter is a function of temperature. In general, on cooling from the Isotropic state, the order parameter slowly increases and tends to saturate on further cooling in a LC phase usually nematic.

1.4.2 Optical anisotropy:

The liquid crystal molecules orient themselves along a specific preferred direction and the physical properties are different along different directions and such a difference can be expressed in terms of the anisotropy [10]. Due to the anisotropy, the polarised light interacts with the molecules of liquid crystals in different ways compared to the isotropic liquid. The light polarised along the director propagates at a different velocity than the light polarised perpendicular to the director. This phenomenon is known as the birefringence.

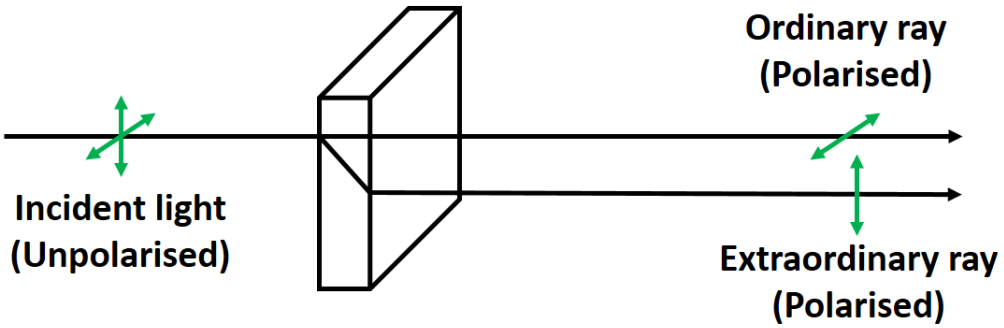

Figure 1.5 Schematic representation of birefringence.

The electric field polarisation of the light parallel and perpendicular to the director is defined with two principle refractive indices n_e and n_o known as extraordinary and ordinary refractive indices respectively. The difference between these two refractive indices is quantified as birefringence Δn as given below,

$$\Delta n = n_e - n_o \tag{1.2}$$

The difference in velocity of the incident light causes a phase difference between the two rays as they travel along the crystal. Due to this reason the transmitted light has a different polarisation state compared to the incident light.

Therefore, we can consider the LC sample to act as a retarder, and the retardation angle can be defined as,

$$\delta = \frac{2\pi \Delta n d}{\lambda} \tag{1.3}$$

where λ is the wavelength of the incident light and d is the sample thickness.

The transmission axis of the light will be at an angle α between slow and fast axis of the LC medium. For the birefringent materials the incident linearly polarised light can be given by,

$$I_{incident} = \begin{pmatrix} I_x \\ I_y \end{pmatrix} = \begin{pmatrix} I_0 \cos\alpha \\ I_0 \sin\alpha \end{pmatrix} \tag{1.4}$$

becomes elliptically polarised after passing through the sample,

$$I_{sample}(z) = \begin{pmatrix} I_x \exp(ik_e z) \\ I_y \exp(ik_o z) \end{pmatrix} \tag{1.5}$$

where $k_{o,e}$ is the wave vector given by $k_{o,e} = n_{o,e} 2\pi/\lambda$, we can use the corresponding Jones calculus for the polarised light through a retarder, given by,

$$\hat{J} = \begin{pmatrix} \sin^2\alpha & -\cos\alpha \sin\alpha \\ -\cos\alpha \sin\alpha & \cos^2\alpha \end{pmatrix} \tag{1.6}$$

the light through the analyser can be obtained from,

$$I_{out} = \hat{J} I_{sample}(z = d) \tag{1.7}$$

$$I_{out} = I_0 \sin(2\alpha) \sin(\Delta k d / 2) \exp[i(k_o + k_e) d / 2] \begin{pmatrix} \sin\alpha \\ \cos\alpha \end{pmatrix} \tag{1.8}$$

therefore the output intensity can be described as,

$$I_{intensity} = |I_{out}|^2 = I_0^2 \sin^2(2\alpha) \sin^2\left(\frac{\Delta n d}{2}\right) \tag{1.9}$$

$$I_{intensity} = I_0 \sin^2(2\alpha) \sin^2\left(\frac{\pi \Delta n d}{\lambda}\right) \tag{1.10}$$

The above Equation (1.10) can be used to obtain the transmitted light intensity as a function of wavelength for the LC (retarder) kept between the crossed polarisers.

1.4.3 Dielectric anisotropy:

An applied electric field induces a polarisation P in dielectric medium like liquid crystals, which is defined as dipole moment per unit volume [11]. For low applied field the polarisation is proportional to the electric field E,

$$P = \varepsilon_0 \chi E \tag{1.11}$$

where ε_0 is the permittivity of free space and χ is the second rank susceptibility tensor. If we assume that the director is along the z-axis in the laboratory frame, then the Equation (1.11) can be rewritten in the tensor form as,

$$\begin{pmatrix} P_x \\ P_y \\ P_z \end{pmatrix} = \varepsilon_0 \begin{pmatrix} \chi_\perp & 0 & 0 \\ 0 & \chi_\perp & 0 \\ 0 & 0 & \chi_{\|} \end{pmatrix} \begin{pmatrix} E_x \\ E_y \\ E_z \end{pmatrix} \tag{1.12}$$

From Maxwell's equations the electric displacement is given by,

$$D = \varepsilon_0 E + P \tag{1.13}$$

$$D = \varepsilon_0 (1 + \chi) E = \varepsilon E \tag{1.14}$$

where $\varepsilon = \varepsilon_0 \varepsilon_r$ and $\varepsilon_r = (1 + \chi)$ is the relative permittivity of the dielectric material. Equation 1.11 can also be rewritten as,

$$P = \varepsilon_0 (\varepsilon_r - 1) E \tag{1.15}$$

The polarisation is contributed by different mechanisms relative to each other:

- The displacement of the atoms shifts the cloud of electron due to the applied external electric field and this is called as electronic polarisation. But this contribution is relatively weak.
- The presence of permanent electric dipole moment in the molecules. Along with the rotational freedom the molecules are aligned parallel to the applied electric field which gives the major contribution to the polarisation for the LC molecular system.

The components of permittivity depend on the direction for LC system which gives rise to the dielectric anisotropy. The two principal components can be defined as $\varepsilon'_{\|}$ which is parallel to the director and $\varepsilon'_{\perp}$ which is perpendicular to the director. The dielectric anisotropy can be then written as,

$$\Delta\varepsilon' = \varepsilon'_{\parallel} - \varepsilon'_{\perp} \tag{1.16}$$

Depending on the LC molecular structure the dielectric anisotropy can be either positive or negative. A LC molecule will exhibit positive $\Delta\varepsilon'$ (*i.e.* $\varepsilon'_{\parallel} > \varepsilon'_{\perp}$) if the net dipole moment of the molecule is parallel to the long molecular axis. Likewise the LC molecule will exhibit negative $\Delta\varepsilon'$ (*i.e.* $\varepsilon'_{\parallel} < \varepsilon'_{\perp}$) if the net dipole moment of the molecule is perpendicular to the long axis of the molecule. In the first case, the director will align along the applied field while in the latter case the director tends to align normal to the applied field. Therefore the sign of $\Delta\varepsilon'$ will decide the director reorientation with respect to the applied field.

Also the refractive indices of a dielectric medium can be related to the permittivity components as given below (If the measurements are made at the same frequency):

$$n_{\parallel}^2 = \varepsilon_{\parallel} \quad \& \quad n_{\perp}^2 = \varepsilon_{\perp} \tag{1.17}$$

which shows that any external field induced change in permittivity will include a change in the birefringence of the LC system. However, in general the permittivity is measured at radio frequencies. The above given relation holds true only if the frequency of the measurement matches. (Note: here $n_e = n_{\perp}$ and $n_o = n_{\parallel}$). This field induced change in birefringence or dielectric permittivity will accompany a tilt with an angle α in the optical axis (director) of the LC system with respect to the polarisation of the light. Therefore the effective refractive index in terms of ordinary and extraordinary refractive indices can be given by,

$$n_{eff}(\alpha) = \frac{n_o n_e}{\sqrt{n_e^{\,2}\cos^2\alpha + n_o^{\,2}\sin^2\alpha}} \tag{1.18}$$

The field induced change in the physical parameters (such as birefringence) is the essence of this thesis. Detailed explanations, experimental results and discussions are given in the following chapters.

1.5 Structures and Properties of Smectic liquid crystals

Smectic (Greek meaning 'soap') is the name coined by Georges Friedel for certain mesophases with physical properties that resembles soaps. All smectic phases are layered in nature with a well-defined interlayer spacing that can be measured by X-ray diffraction [10]. In general, the layer thickness in smectic LCs can vary from values close to full length of the constituent molecules to twice of the molecular length (bilayer structure). Earlier, there was only one type of smectic phase known as Smectic A (SmA), but later several different phases were identified with distinct properties. The different types of smectic phases formed by calamatic shaped molecules are listed below with its nomenclature;

1. Smectic A (SmA) – orthogonal phase
2. Smectic C (SmC) – tilted phase
3. Smectic B (SmB) – hexatic phase
4. Smectic C_A^* (SmC_A^*) – Anti-ferroelectric phase
5. Smectic C_α^* (SmC_α^*) – Unwound Anti-ferroelectric phase with a short helical pitch.
6. Smectic C_γ^* (SmC_γ^*) – Ferrielectric Phase

7. There are number of sub phases in SmC* temperature range which are represented as SmC^*_A (q_T). where q_T can have values like 1/2, 1/3, .. etc These numbers define the number of tilt correlated layers.
8. Smectic I (SmI) – pseudo-hexagonal tilted phase
9. Smectic F (SmF) – pseudo-hexagonal orthogonal phase

Note: The phase denoted with by * symbol represents chiral phase. Influence of chirality in smectic LC's is discussed later in this section.

1.5.1 Structures of Orthogonal and tilted smectic phases:

The entire work in this thesis is purely based on SmA and SmC phase. Hence here we will see a detailed description of these phases.

The layered molecular arrangements are characterised in terms of the molecular long axis ***z*** and layer normal **Z** (sometimes layer normal is denoted by $\vec{k}$). Here we can define **X,Y,Z** and ***x,y,z*** as the laboratory and molecular frames of reference respectively. In SmA phase the molecular long axis ***z*** is almost parallel to the layer normal **Z**, i.e. the director $\vec{n}$ is parallel to the layer normal. It is also known as orthogonal phase since in SmA the molecules are almost perpendicular to the layer plane. The SmA phase is optically uniaxial, where the optical axis is also parallel to the layer normal. X-ray results shows that the in SmA phase the layer thickness is almost equal to the calculated molecular length [5]. Mostly in the LC phase sequence the orthogonal phase is followed by a tilted phase (SmC) on cooling. In SmC phase the molecular long axis is tilted with respect to the layer normal with an angle θ, correspondingly the director and optical axis is also tilted with respect to the layer normal. As evidence, the experimentally measured layer thickness measured in a tilted phase is almost always less than the molecular length in SmC phase. This is

due to the fact, that in SmC phase a molecular tilt appears which in turns reduces the layer thickness.

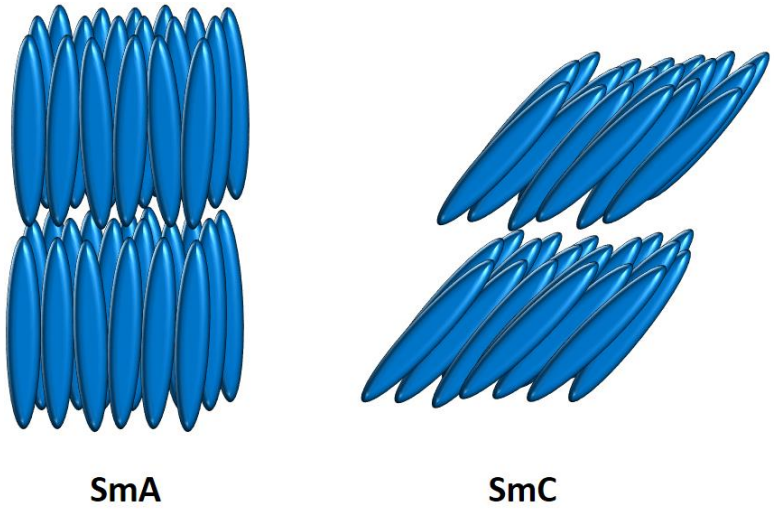

Figure 1.6 Idealised representation of SmA and SmC phase.

1.5.2 Effect of chirality in smectic phases:

Presence of chirality in the molecular structure can greatly influence the macroscopic properties of the liquid crystals [1]. The chiral centre in the molecule is responsible for an intermolecular force which leads the molecules to align with a slight twist angle with respect to the others. As we have seen earlier, that the chiral molecules form cholesteric nematic phase, thus exhibiting unique properties compared to the conventional nematics. Similarly chiral molecules forming smectic phases exhibit some interesting properties.

Chiral molecules lack mirror symmetry. The tilted smectic phase of chiral molecules forms helical structures with a defined pitch and these phases are denoted with an asterisk (*) symbol. These phases are optically active compared to the non-chiral tilted smectic phases. As shown in Figure 1.7, in SmC* phase the molecular tilt can be visualised with a cone, and it varies azimuthally in space. Here pitch is

defined as the length taken for one complete rotation in azimuthal angle around the cone (360 deg) along the long axis of the helical structure.

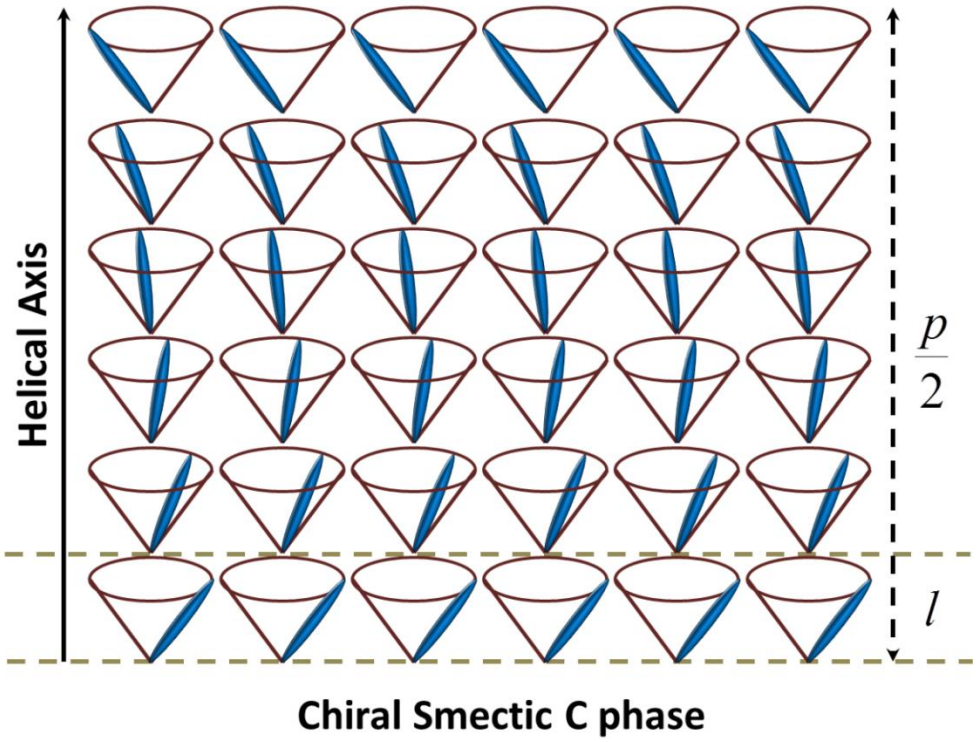

Figure 1.7 Schematic representation of chiral SmC* phase. (*l*-layer)

1.5.3 Ferroelectric Liquid Crystals:

In 1974, Meyer *et al.* on the basis of symmetry arguments demonstrated that the tilted smectic phases consisting of chiral LC molecules must exhibit ferroelectricity [12]. It was shown that the chirality couples with the molecular tilt (θ) to exhibit macroscopic spontaneous polarisation ($\boldsymbol{P_S}$) in each layer, normal to the tilt plane. Followed by this discovery, a new class of liquid crystals emerged known as Ferroelectric Liquid Crystals (FLCs).

In general, FLCs respond to applied electric field by reorienting the director over their variable azimuthal orientation ϕ about the layer normal. The application of

external electric field will unwind the helical structure. The polar nature of FLC enables it to switch faster (sub microsecond) than nematics [13,14].

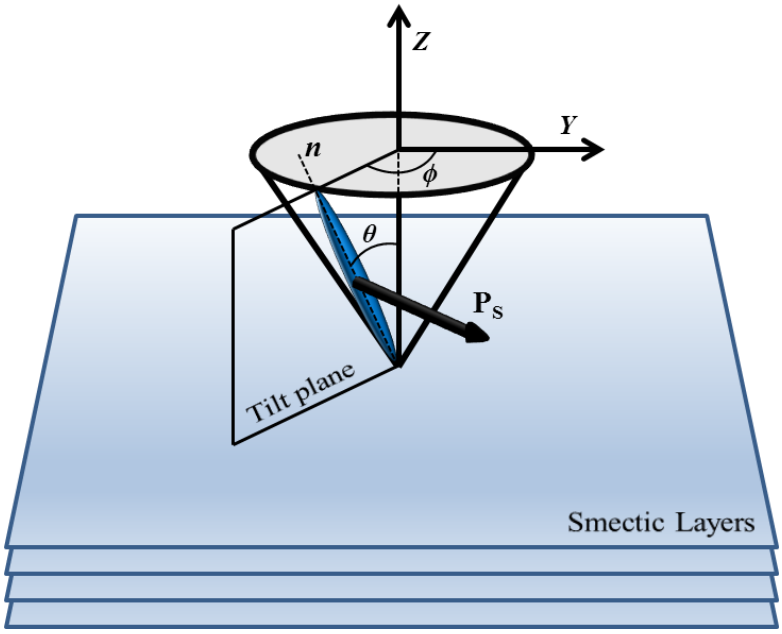

Figure 1.8 Schematic representation of spontaneous polarisation (P_S) normal to the tilt plane in FLC.

1.5.4 Research statement:

After the demonstration of sub microsecond electro-optical switching, FLCs gained huge attention for display applications. FLCs promised 1000 times faster switching, high contrast ratio and bistability compared to nematics. These properties would allow approximately 70% of energy savings under colour sequential mode and almost power-free operation for bi-stable and multi-stable modes. The fast switching speed can be used in ever expanding field of optical communications. In spite of the extensive research by several groups in this field, FLC based display is yet to become a commercial reality. This is mainly due to the following reason, the transition from SmA* to SmC* phase is associated with the appearance of molecular tilt θ with respect to the layer normal. This tilt angle can be as large as ~30° and the consequent

layer contraction [15] could be as high as ~13% [16]. A combined effect of layer shrinkage and surface anchoring results in buckling of layers which leads to a chevron structure [17]. Opposite folds of chevron structure gives rise to zigzag line defects which severely degrade the optical quality of the FLC display [15]. Inevitable defects became the limitation for a successful technological exploitation of these materials. One of the plausible solutions for the above problem is to develop FLCs with minimal or zero layer shrinkage [16].

An unexpected discovery of low layer shrinkage almost 30 years ago in some materials sparked an interest in the research community. Since then, several models were postulated in order to explain the anomalous phenomena. The most prominent and earliest model was developed by the American crystallographer Adriaan de Vries. At that time, the idea did not gain much importance, as most of SmC materials showed substantial layer shrinkage. Later in 1990s, due to the serious problems in the FLC device applications the low layer shrinkage materials and de Vries models attained renewed focus. This rendered many questions for smectic LC materials exhibiting low layer shrinkage. Also, in the literature this special class of smectics are referred as “de Vries smectics”, due to the pioneering contributions made by Adriaan de Vries. Thus “de Vries smectics” eventually become one of the hot topics in the liquid crystal research community in recent years.

1.6 History of de Vries smectic liquid crystals:

Based on the experimental evidence the SmA phase is uniaxial, which means that the optical axis or director is parallel to the layer normal. Due to this fact, we can employ a naïve picture that the long axis of the calamatic molecules are pointed along the layer normal, which makes the layer thickness in SmA phase (d_A) to be

equal to the molecular length (l) under hard-rod approximation. On cooling the sample and on reaching SmC, the molecular tilt θ appears and the layer spacing in SmC phase is reduced to [18,19]:

$$d_C = d_A \cos\theta \tag{1.19}$$

However, in 1972 Diele *et al.* [20] reported a number of smectic LCs with layer thickness (d) lower than the molecular length (l) in SmA phase from X-ray measurements. Here the measured layer thickness was 5-10% lower than the calculated molecular length. Diele *et al.* explained these phenomena based on conformational disorder and the interdigitation of the molecules from neighbouring layers. De Vries in 1977 [21] studied one of the compounds reported by Diele *et al.* showing no significant change in d at Sm*A* to Sm*C* transition. Initially de Vries proposed that the molecules are already tilted in SmA phase with a fixed angle θ_A and tilt direction (ϕ) varies from layer to layer in a random fashion preserving the uniaxial nature of SmA phase. This is now referred as the 'non – correlation model' or 'hollow-cone model'. Though this intuitive model could explain the experimental finding of $d_A < l$, accuracy of it was critically debated. The basic idea of this model appeared in the literature [22].

Later, in 1978 [23], Leadbetter *et al.* reported a low orientational order parameter and broad orientational molecular distribution in SmA from X-ray diffraction studies. Inspired by these results, de Vries in 1979 [24-26] gave a refined model. He described that in SmA phase, molecules are already tilted but distributed over a cone having a long range correlation in azimuthal angle ϕ and a short range correlation in tilt θ across the layers. This model is now commonly known as 'diffuse-cone model'. In addition to this, de Vries also showed that these materials

exhibit first order SmA – SmC phase transition. Materials that possess the above mentioned dissimilarities from conventional smectics are classified as 'de Vries smectics'. The low layer contraction in de Vries smectics sparked an interest as these materials can be promising candidates for FLC display applications [27].

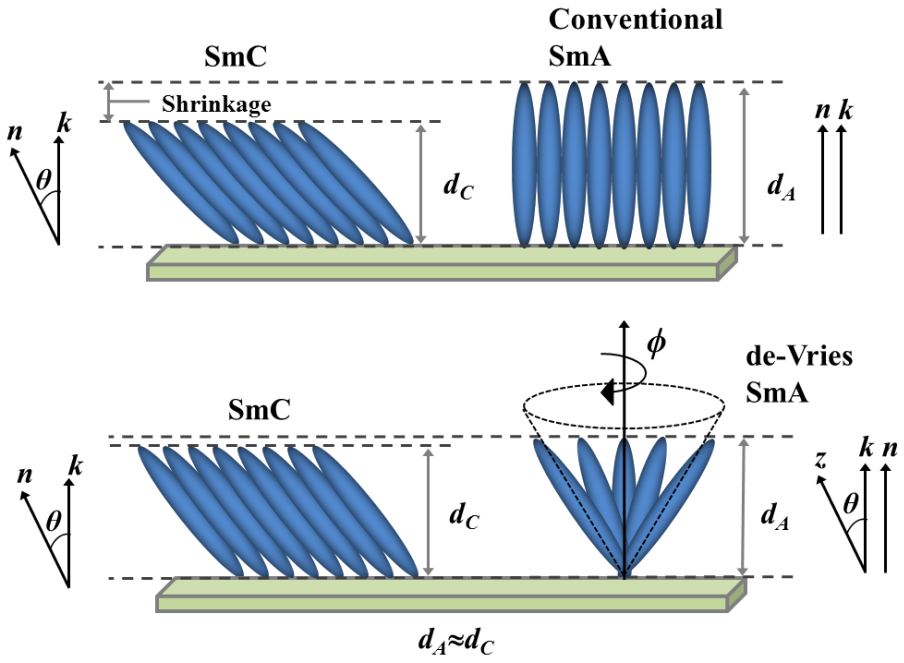

Figure 1.9 A comparison between the conventional and de Vries type LC.

Subsequent experimental work in chiral de Vries smectics revealed other non-conventional properties apart from the low layer shrinkage and the first order phase transition. Those are listed below,

- Large electro-clinic co-efficient [28,29].
- Field induced change in the birefringence in SmA* phase [22,30,31].
- Non-monotonic trend in layer thickness and birefringence as a function of temperature [31-36].
- Lack of nematic phase [16,37].

The diffuse-cone model qualitatively explains the low layer shrinkage. However, it fails to explain the unique electro-optic response and the origin of first order phase transition of de Vries smectics. Apart from the diffuse –cone model several other theoretical approaches were carried out. Initially the difference ($d < l$) was anticipated as a result of kinked molecular conformation and interdigitation which leads to the low order parameter [20]. Bahr *et al.* used simple Landau theory to explain the electro-clinic effect [38]. Saunders *et al.* developed a model based on field induced biaxiality for explaining the electro-optic response in de Vries Sm*A* using the generalized Landau theory [39]. Lim *et al*. explained the non-monotonic trend in temperature dependent birefringence as a result of enhanced critical fluctuations [40]. While these models successfully explain the specific phenomena, they do not provide full depiction of 'unconventionalities' of de Vries smectics.

Clark *et al*. in 2002 modelled the electro-optic response of the de Vries smectics in terms of Langevin-Debye based Mean-Field potential, assuming that the molecules in Sm*A** phase is confined in a cone with a fixed angle [41]. Although this model could qualitatively reproduce many features of de Vries electro-optics, it does not fit to the experimentally observed unique sigmoidal shape of the electro-optic response. Therefore, Shen *et. al*. in 2013 proposed an updated version of the original model known as the 'generalised Langevin-Debye model', in which the tilt of the molecule is allowed to vary within a limited range [42]. Later, Kost-Smith *et al*. proposed that diffuse cone model can also explain the origin of the first order phase transition in de Vries smectics [43].

Recently Merkel *et. al.* [44] gave a compensation model for explaining the anomalous temperature dependence of layer thickness in achiral de Vries type liquid

crystals. Various molecular modelling approaches were carried out to explain the low layer shrinkage and the huge electro-optic response [45-48].

1.7 Research objectives:

The primary aim of this thesis is to study the properties of de Vries type of ferroelectric liquid crystalline systems. The main objectives are:

- To investigate the effect of chiral doping in achiral de Vries type smectic liquid crystals.
- To characterise the novel chiral de Vries type smectic liquid crystals and to understand the chemical structural dependence of de Vries properties.
- To examine and improvise the EO modelling of the de Vries type liquid crystals.

1.8 Thesis preface:

Chapter 1 contains the general introduction to Liquid Crystals, which briefly outlines the basic concepts such as the various types of LC phases, molecular shape dependent LC phases, physical properties and theoretical approaches for LC systems. Moreover we present a detailed history of the origin of de Vries type LCs and related review of that subject.

Chapter 2 presents a brief introduction to all the experimental methods used to investigate properties of the liquid crystalline systems under study in this thesis.

Chapter 3 describes the effect of chiral doping in achiral de Vries type smectic LC belonging to a homologues series. This study provides useful insights into how does the dopant induce the ferroelectricity in the host system without altering the characteristic properties of the host.

Chapter 4 involves the characterisation study of known de Vries type smectic LC using X-ray, EO and IR experimental techniques. The diffuse EO modelling from the literature is used to fit the experimental results of materials under study.

Chapter 5 presents characterisation of novel de Vries type LCs that were designed based on the knowledge from literature. Also we begin to improvise the EO modelling based on the speculations from experimental results.

Chapter 6 focuses on a comparison of two structurally analogues de Vries type smectics. Detailed high resolution measurements were carried out to characterise de Vries properties of these two LCs. A well refined version of the EO modelling is proposed to understand the microscopic origin of the huge EO effect and to reveal the molecular organisation in de Vries SmA* phase.

Chapter 7 contains a summary of the results and the general conclusions that have been drawn from work presented in this thesis. Also some possible future work is also been outlined.

\

Chapter 2

2. Experimental Methods

2.1 Polarising Optical Microscopy

Polarising optical microscope (POM) is a regular optical microscope equipped with a pair of polarisers and other accessories. It has been designed to observe the optical properties of birefringent materials such as crystals. The polarising microscope was originally developed for studying the crystalline structures of rocks and minerals. However, POM is now used in medical and biological fields for research and examination purposes. It also has many industrial applications like asbestos identification, fibril defect analysis, electronics and forensics. Improved performance of polarising microscope can be achieved by combining a full range of accessories. This would help us to perform operations like detecting minute double refraction and measure retardation.

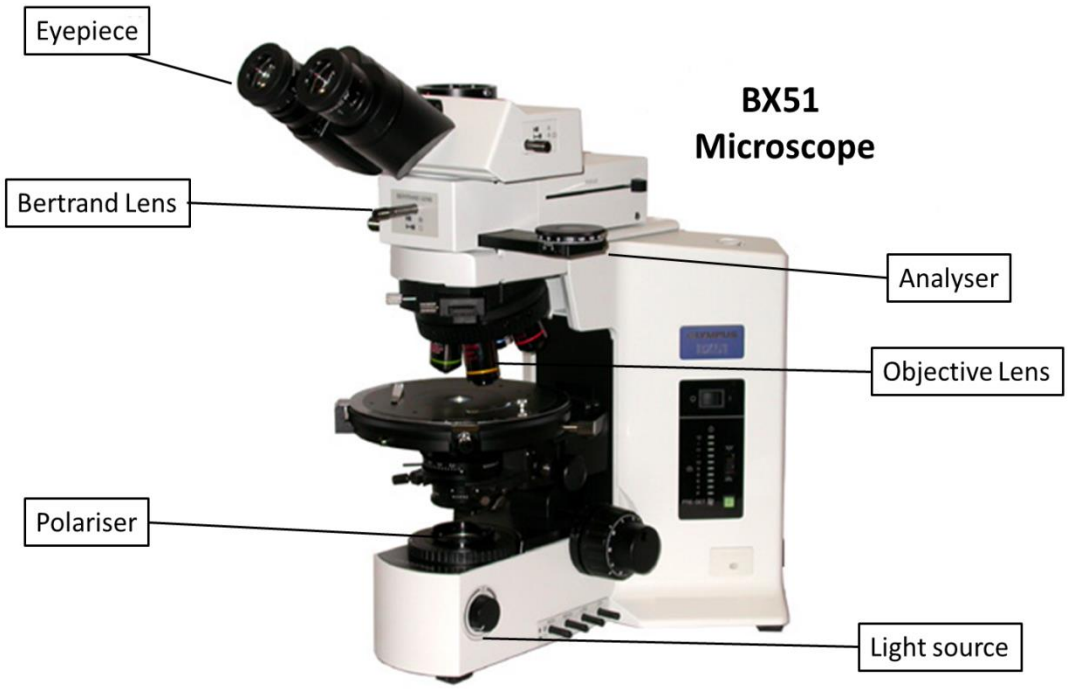

Figure 2.1 Olympus BX51 microscope.

2.1.1 BX51 equipment details

Polarising microscope is one of the main characterisation tools in liquid crystal research field. All the POM studies mentioned in thesis are performed using Olympus BX51 microscope (Figure 2.1). This microscope is comprised of the following sections:

- **Base:** (a) voltage indication, (b) light intensity pre-set switch, (c) filters
- **Focusing block:** (a) fine adjustment knob, (b) coarse adjustment knob tension, (c) pre-focusing lever
- **Stage:** (a) place for the specimen, (b) X- and Y-axis knob tension, (c) rotation of the stage, (d) adjustment of the stage height
- **Observation Tube:** (a) adjustment of the inter pupillary distance, (b) dioptre, (c) eye shades, (d) eyepiece micro meter disk, (e) trinocular tube
- **Condenser**
- **Bertrand Lens:** A specialised lens mounted in an intermediate tube or within the observation tubes. Bertrand lens projects an interference pattern formed at the objective rear focal plane into focus at the microscope image plane. The lens is designed to enable easy examination of the objective rear focal plane, to allow accurate adjustment of the illuminating aperture diaphragm and to view interference figures.

2.1.2 Types of liquid crystal cells:

In most of the LC experiments, a mono-domain sample is required. In general, the LC orientation is random on macroscopic scale and has to be constrained in one direction by an external force. One of the most common methods to achieve such condition is to sandwich the LC sample between the two glass-substrates. The

preferred orientation is usually obtained by coating a suitable layer of polymer to the glass-substrates. Also, the glass-substrates are coated with a thin Indium Tin Oxide (ITO) layer in order apply electric field. In this thesis, all the experimental results are obtained using a commercially available LC cells produced by E.H.C Co. Ltd., Japan. A schematic representation of a LC cell is shown in Figure 2.2.

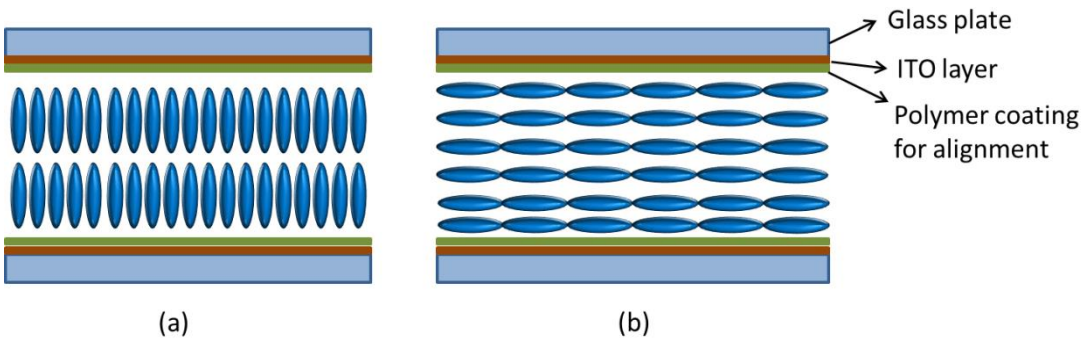

Figure 2.2 Idealised representations of alignments of LC cell. a) Hometropic b) Planar

The LC cells are basically classified into two types, based on the sample orientation geometries. They are,

- **Homeotropic geometry:** In homeotropic geometry or alignment, the optical axis or long axis of the molecule is aligned perpendicular to the glass substrate. This implies that, under the POM the optical axis of the LC sample is aligned along the direction of the incident light, thus a uniaxial LC sample with homeotropic geometry should appear dark under the crossed polariser state. Homeotropic alignment is usually attained by coating the substrates with a surfactant such as carboxylate chromium complexes (Chromolane).
- **Planar geometry:** Planar geometry or alignment is complementary to homeotropic, where the optical axis or long axis of the molecule is aligned parallel to the glass substrate. For example in SmA phase, the layers are

arranged perpendicular to the substrate. Planar-aligned cells under POM show birefringence colours, the order of interference colour depends on the thickness of the cell. The planar alignment is also known as homogeneous alignment. Planar geometry can be obtained by coating the substrates with a thin layer of polymer (polyimide or polyamide) followed by heating in order to cure the polymer. After the coating process the glass substrates are rubbed with a velvet cloth along a single direction in order to impose a uniform director orientation.

2.2 Differential Scanning Calorimetry

Differential Scanning Calorimetry (DSC) is a rapid method to measure the heat capacities of materials. The thermal analysis of a sample using DSC is obtained based on the difference in the amount of energy required to increase or decrease the temperature between sample and reference, as a function of temperature. DSC technique is widely used by LC research community as a preliminary characterisation tool in order to obtain the phase transition temperatures of a LC sample. It is possible to observe very small energy changes that occur as the sample undergoes different LC phase transitions. In this thesis, all the DSC thermograms were obtained using Perkin-Elmer DSC 8000.

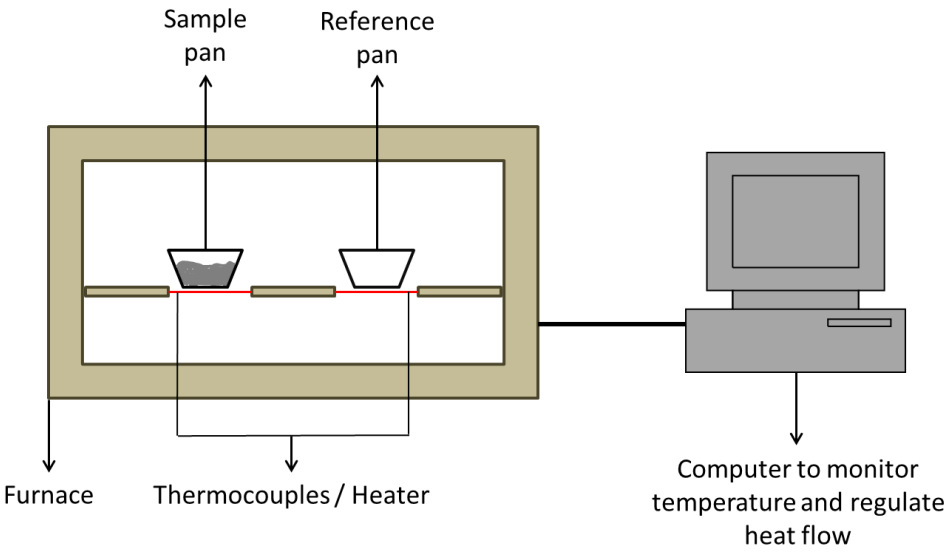

Figure 2.3 Schematic representation of DSC setup.

2.2.1 DSC experimental methodology:

- 4-5 mg LC sample is filled and sealed in an aluminium pan.
- An empty aluminium pan is used as reference.
- The sample and reference is maintained in a static nitrogen atmosphere.
- The heating and cooling cycles were performed at 10^{o} C/min.

2.3 Layer thickness measurements:

2.3.1 X-ray diffraction studies:

The most commonly used technique to determine the molecular packing, smectic layer spacing and order of a LC sample is X-ray diffractometry (XRD). A typical X-ray set-up is shown in Figure 2.4.

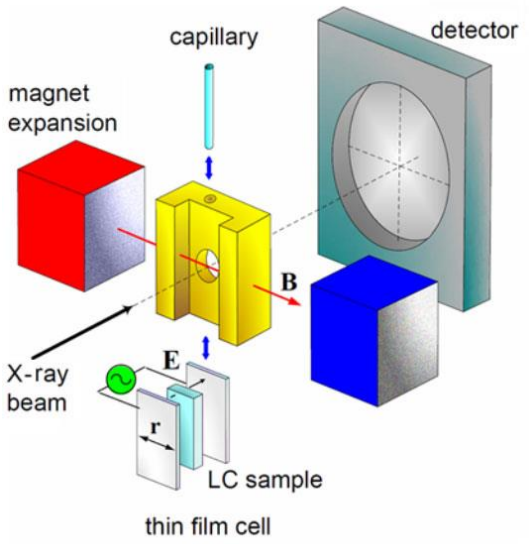

Figure 2.4 Schematic representation of XRD set-up for LC sample (From Ref [49]).

The fundamental principal behind XRD technique is Bragg's law. Bragg's law describes that, a constructive interference is formed when the path difference of rays reflected from the adjacent crystal lattice is equal to an integral multiple of the incident X-ray's wavelength. The Bragg's equation can be expressed as,

$$n\lambda = 2d\sin\theta \tag{2.1}$$

where d is the separation between the lattice planes, θ is the angle of the incidence, n is an integer and λ is the wavelength of X-rays. Bragg's law gives an inverse relation between the distance between the lattice plane and the diffraction angle; however it does not provide information about the intensities of the various peaks. The total scattered intensity is independent of the positional order, and depends only on the total number of scattering centres, consisting of any periodic distribution of electron density, and their scattering power. When an X-ray beam with an initial wave vector k_i, whose direction specifies the direction of propagation and modulus $|k_i| = 2\pi/\lambda$ is scattered, the wave vector k_i changes to k_f with a momentum transfer. Since the scattering is elastic (no change in energy), the magnitude of the wave

vectors are equal. By the de Broglie relation, the scattering vector is defined by $Q = k_f - k_i$. Its modulus is given by:

$$|Q| \equiv Q = \frac{4\pi \sin\theta}{\lambda} \tag{2.2}$$

The Bragg's law equivalent of above equation is:

$$Q = n\left(\frac{2\pi}{\lambda}\right) \tag{2.3}$$

The diffracted intensity is hence most conveniently plotted as a function of the scattering vector. For a system containing *N* molecules, the total scattered intensity at a point is expressed by the product of the form factor $F(\vec{q})$ and the structure factor $S(\vec{q})$. The form factor is determined by the molecular structure of the mesogen and depends only on the single particle distribution function, while structure factor includes both orientational and spatial correlations. The total intensity is given by,

$$I(Q) = F(\vec{q}) \times S(\vec{q}) \tag{2.4}$$

In order to observe a particular diffraction peak, the planes must be aligned at angle θ_n to the incident beam. The LC sample can be aligned by either a magnetic field for the material in a glass capillary or an electric field applied across a LC thin film in the planar cell configuration. Examples of scattering from Isotropic, N, SmA and SmC are shown in figure 2.5

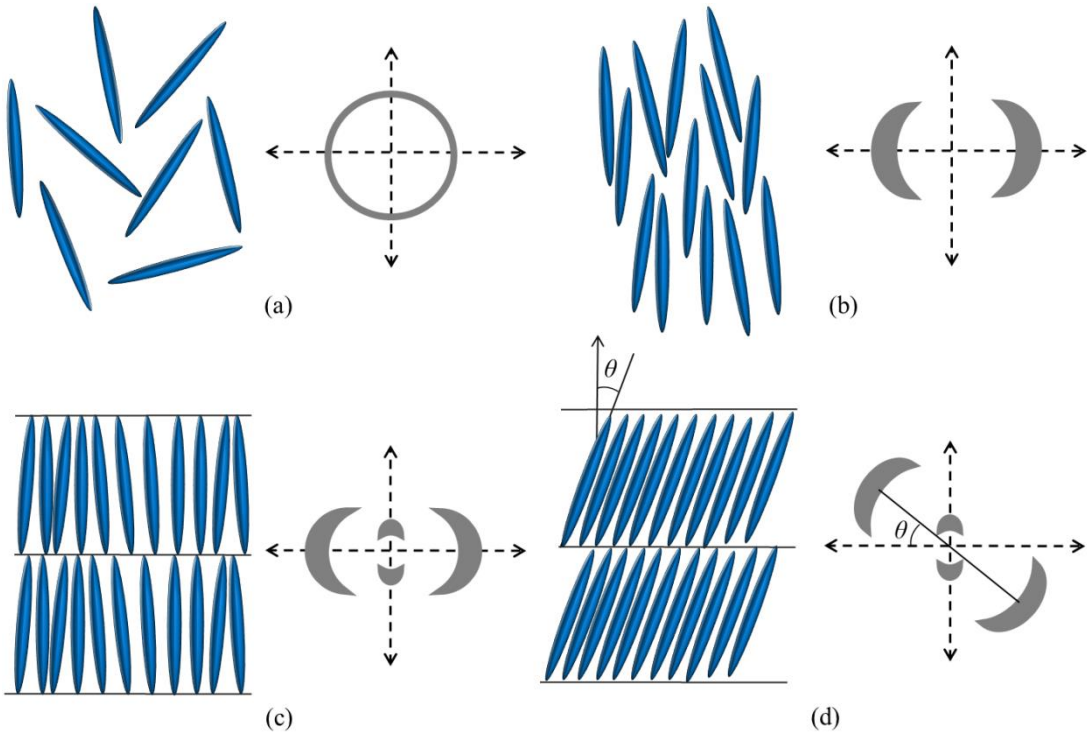

Figure 2.5: Schematic representation of 2D X-ray patterns of (a) Isotropic (b) Nematic (c) SmA (d) SmC, phases

The isotropic phase is characterised by the absence of the long range orientational or positional order. The isotropic phase cannot be aligned; hence its diffraction pattern consists of weak, diffuse ring (Figure 2.5 (a)). For an aligned nematic LC sample the XRD patterns consist of two sets of diffuse arcs (Figure 2.5 (b)). The intensity of these arcs is indicative of the extent of alignment within the sample; generally represented by the order parameter, *S*. While in SmA phases, two sets of diffuse peaks are seen in diffraction pattern (Figure 2.5 (c)); the diffuse peak at a small angles condense into sharp quasi-Bragg peaks. In SmC phases, where the molecules are tilted with respect to the layer normal, the diffuse peaks at smaller and larger angles are no longer orthogonal to each other (Figure 2.5 (d)).

2.3.2 Free-standing Film studies:

The layered nature of smectic LC phases can be used to form freely-suspended film similar to soap bubbles. We employ a homemade high resolution

interferometric technique to estimate the thickness of a uniform thin smectic LC film. A detailed explanation is given below,

A hole with a diameter of 3mm is drilled in a 200µm thick stainless steel plate used as a film template. A small quantity of the LC sample is placed on the template mounted over a hot-stage to maintain stability of temperature. A clean spatula is used to the draw the LC material over the hole to form a free-standing film (FSF) as shown in the schematic representation Figure 2.5.

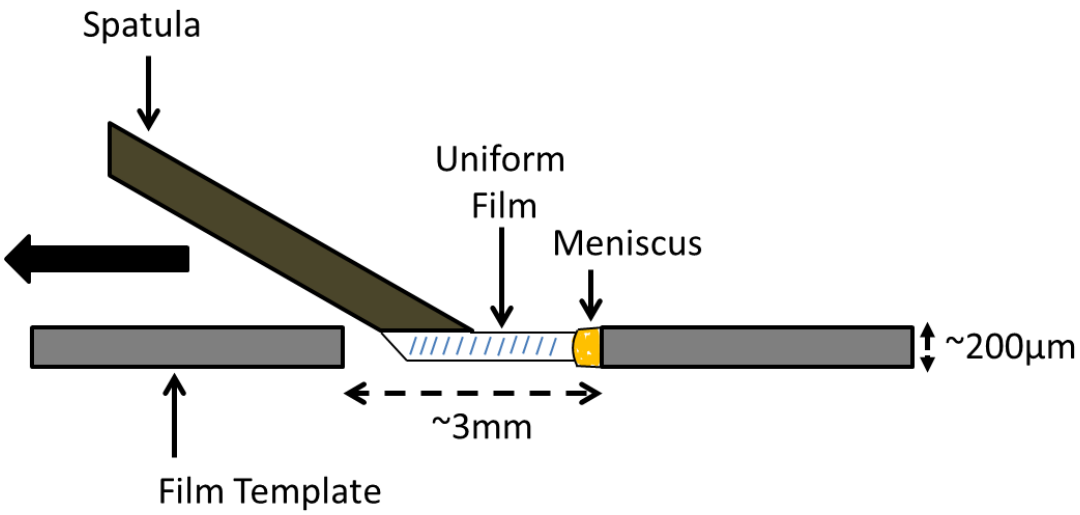

Figure 2.5 Schematic representation showing the preparation FSF film.

The temperature to attain the film will be optimized depending on the viscous nature of the material. Usually temperature close to SmA-Iso is ideal to achieve a uniform film. Due to the capillary action, a thick meniscus is formed around the wall leading to the formation of stacked layers in the middle. A typical example of a FSF in SmA phase is shown in Figure 2.6.

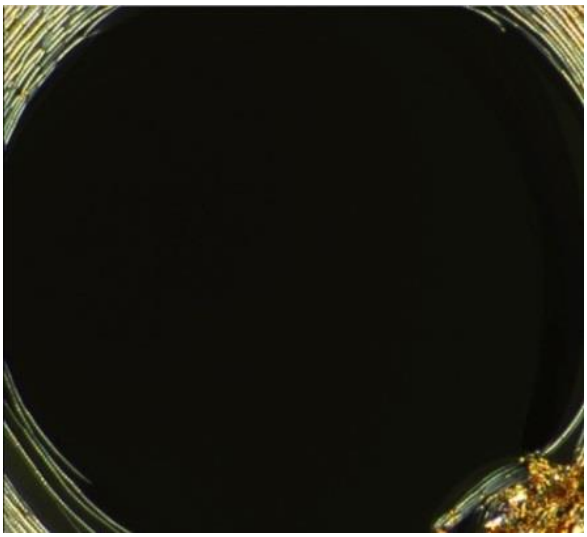

Figure 2.6 POM image of SmA phase of a FSF.

A uniform homeotropic alignment is achieved by adopting several heating and cooling cycles with different rates which help in attaining equilibrium in the collective motion of molecules in the FSF. Once a uniform film is made, the smectic FSF has a tendency to keep the number of layers constant regardless of the change in temperature.

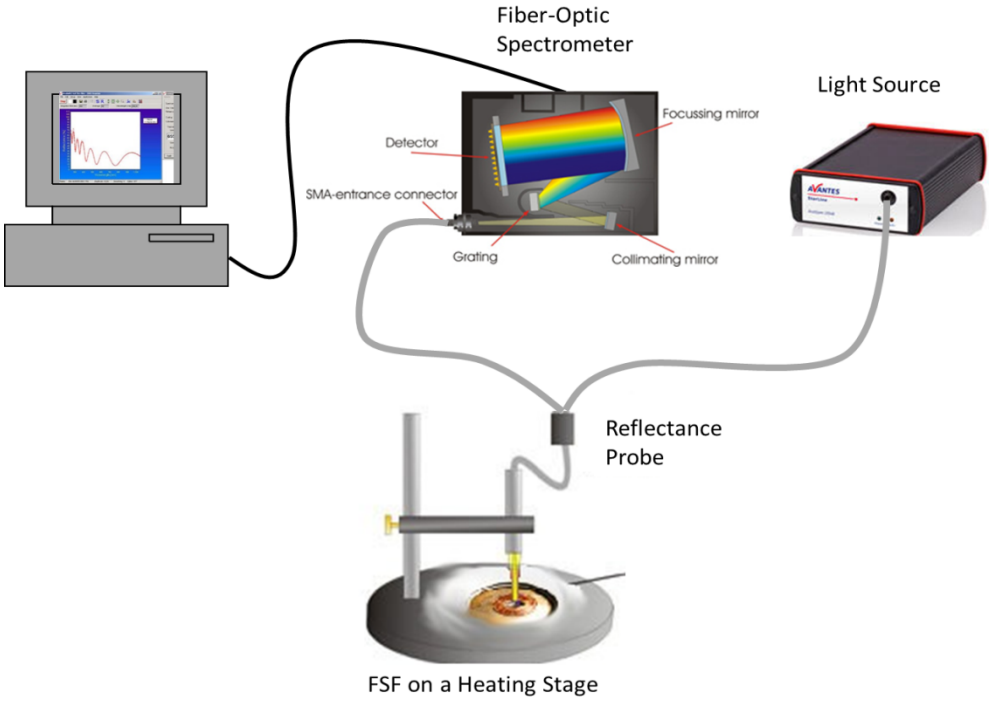

Figure 2.7 Schematic representation of FSF measurement setup

Interferometric method allows us to estimate the optical thickness of the FSF. The optical thickness of a FSF can be expressed as,

$$d_{opt} = n_{eff} L d_{layer} \tag{2.5}$$

where n_{eff} is the effective refractive index, L is the number of smectic layers in FSF and d_{layer} is the thickness of a single smectic layer. In order to estimate the optical thickness of the film, a non-polarised white light is incident normal to the film. Reflected light rays from the top and the bottom of film surface produce an interference fringe, directly related to the optical thickness of the film. The reflectance spectra are recorded and analysed using Avaspec® - 2048. This spectrometer contains no moving parts and is capable of acquiring thousands of spectra with a rate better than 1 spectrum per minute. The FSF is mounted on a hot-stage which is operated by a Eurotherm® 2604 temperature controller. The temperature can be stabilized with an accuracy of 0.01° C.

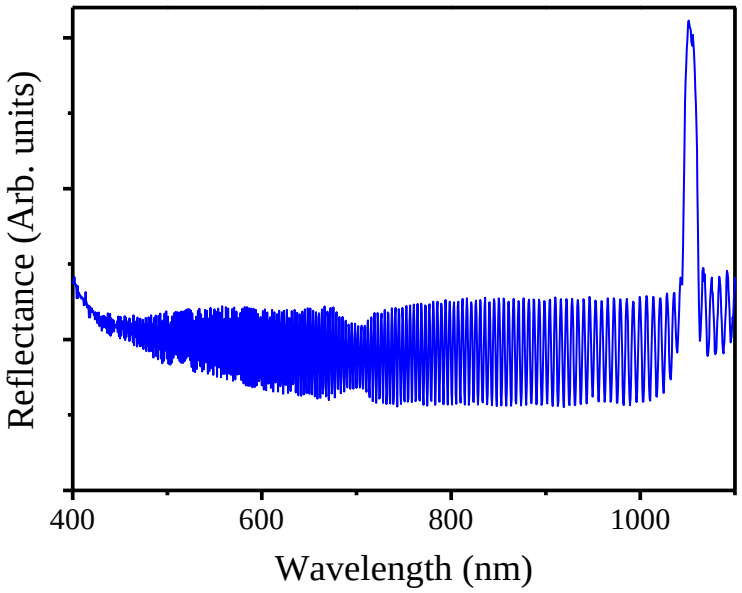

Figure 2.8 A typical reflectance spectrum of a FSF.

A constructive interference (maximum) of the reflected intensity occurs for the following condition,

$$2n_{eff}d_f = N\lambda_1 \tag{2.6}$$

where d_f is the physical thickness of the film (also $d_f = Ld_{layer}$), N is an integer and λ_1 is the corresponding wavelength of the peak. While another maximum occurs after an integral number (k) of maximum can be defined as,

$$2n_{eff}d_f = (N+k)\lambda_2 \tag{2.7}$$

Solving the system of Equations (2.6) and (2.7) gives:

$$N = \frac{2n_{eff}d_f}{\lambda_1} \tag{2.8}$$

$$2n_{eff}d_f = \left(\frac{2n_{eff}d_f}{\lambda_1} + k\right)\lambda_2 \tag{2.9}$$

$$2\lambda_1 n_{eff}d_f = 2n_{eff}d_f\lambda_2 + k\lambda_2\lambda_1 \tag{2.10}$$

We can obtain the optical thickness,

$$n_{eff}d_f = \frac{k\lambda_1\lambda_2}{2(\lambda_1 - \lambda_2)} \tag{2.11}$$

A special program is utilised in order to automate the entire process. As a result, we can capture the spectrum every 0.01 °C change in the temperature for any defined range of temperatures. This highly automated setup can provide a resolution better than 0.01%.

2.4 Electro-Optic experiments

2.4.1 Automated Time-resolved Polarimetry:

Birefringence Δn and the induced optical axis tilt θ_{ind} is measured using a technique of automated time-resolved polarimetry (ATP) developed in our laboratory. The basic principle of the method was given by Park *et al.* [50]. The experimental setup for the ATP includes Polarising Optical Microscope (POM), in which the polarizer and the analyser are individually rotated automatically. Intensity of the transmitted light (Red LED wavelength $\lambda = 633nm$) through the LC sample is recorded using a 16-bit data acquisition board (Keithley® KUSB-3116). A triangular wave electric field signal is applied across the planar-aligned sample. The procedure starts by fixing the polarizer position (α_P) with respect to the reference direction and then acquiring transmitted intensity (a dataset corresponding to one cycle of the applied voltage waveform) for at least 3 different positions of the analyser (α_A). At the given instant of time, the intensity, $I(\alpha_A)$, as a function of the position of the analyser, is given by a sine wave function with the bias *B*, amplitude $(S^2 + C^2)^{\frac{1}{2}}$ and an initial phase angle of $\tan^{-1}(C/S)$:

$$I(\alpha_A) = I_0(S\sin 2\alpha_A + C\cos 2\alpha_A + B) \qquad (2.12)$$

Here I_0 is the intensity of the light source. Each of the coefficients *S*, *C* and *B*, is also a biased sine wave and is a function of the polarizer position α_P as given below:

$$S = S_S \sin 2\alpha_P + C_S \cos 2\alpha_P + B_S \tag{2.13}$$

$$C = S_C \sin 2\alpha_P + C_C \cos 2\alpha_P + B_C \tag{2.14}$$

$$B = S_B \sin 2\alpha_P + C_B \cos 2\alpha_P + B_B \tag{2.15}$$

Therefore, by repeating the above procedure for at least three different positions of the polariser, α_P, we can obtain the desired nine coefficients (S_S, C_S, B_S, S_C, C_C, B_C, S_B, C_B, B_B) by fitting the recorded data to Equations (2.12) to (2.15). The experimental error can be reduced by increasing the number of polariser/analyser positions used in the data acquisition for an experiment. Note that, this will not require any changes to the data treatment algorithm. On assuming that a liquid crystalline cell can be represented by a plate of uniform retardation of magnitude, Δnd_{cell}, we can relate the retardation value to the coefficients by using either the Jones or the Mueller matrix [51]:

$$\cos\left(\frac{\pi \Delta n d_{cell}}{\lambda}\right) = \sqrt[2]{\frac{C_C + S_S}{2B_B}} \tag{2.16}$$

$$\tan 4\theta_{ind} = \frac{C_S + S_C}{C_C - S_S} \tag{2.17}$$

Since the signal applied to the sample is periodic (triangular wave is used in most experiments), the response to the applied waveform can be acquired sequentially for each set of the polariser/analyser position. Therefore, we can obtain these nine coefficients for every point on the waveform thus the real-time response of the birefringence and apparent tilt angle to an applied electric field can be measured.

Table 2.1 shows the sample data set from an experiment. Figure 2.9 shows the Δn and θ_{ind} as a function of applied voltage for a single temperature.

Table 2.1 Sample fit parameters to obtain Δn using ATP measurement technique.

E (V/µm)	S_S	C_S	B_S	S_C	C_C	B_C	S_B	C_B	B_B	Δn
5.5	0.952	-0.353	0.003	-0.558	1.250	-0.013	0.002	-0.039	1.594	0.0604
10.5	1.056	-0.477	0.003	-0.630	0.974	-0.010	0.002	-0.041	1.584	0.0658
16.5	1.113	-0.512	0.002	-0.636	0.816	-0.008	0.001	-0.041	1.576	0.0688

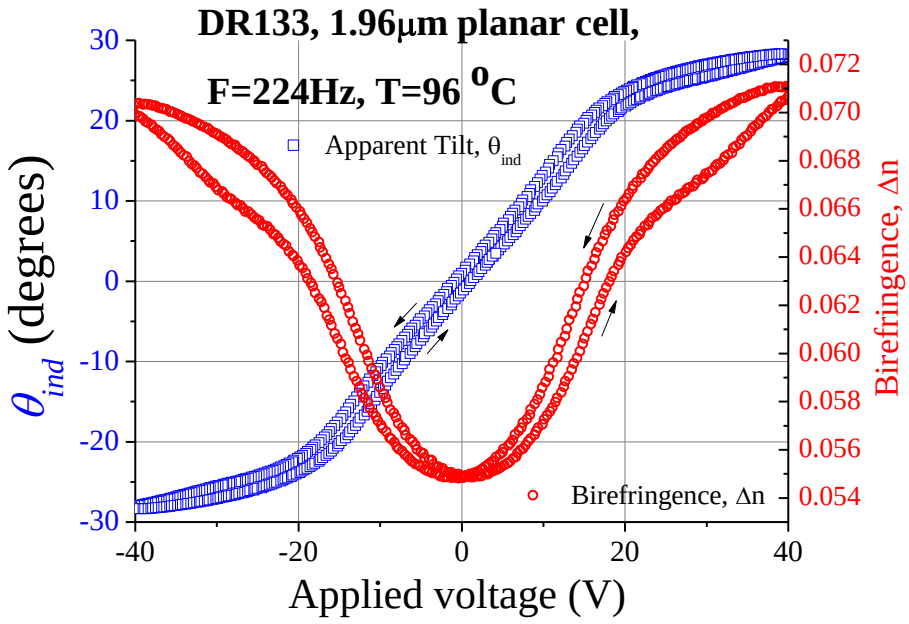

Figure 2.9 Voltage dependent Δn and θ_{ind} obtained using ATP technique.

2.4.2 High resolution Electro-Optic Spectrometer:

The set-up for investigation of harmonics of electro-optic (EO) properties of the liquid crystals includes POM with crossed polarisers, a photodiode detector,

oscilloscope, and/or lock-in amplifiers. The photodiode detector is mounted on top of the microscope as shown in the Figure 2.10. A multifunctional data acquisition board (DAQ) (National Instruments® NI-USB-6216) is configured and programmed to act both as function generator and an oscilloscope. Any type of periodic waveform can be applied to the LC cell, however in general a sinusoidal wave form is applied to the LC cell for EO experiments. The LC cell is placed at an angle of 22.5° from the polariser. The corresponding optical transmittance of the system is measured by the photodiode which is then fed to DAQ. Special software with lock-in amplifier algorithm allows simultaneous extraction of the DC component and the first four harmonics of the photodiode current. The harmonic signals are locked to the reference channel (applied periodic waveform). The constituents of the output are recorded as a function of temperature and of applied electric field. This high resolution method detects the switching properties of the LC which is not visible by conventional oscilloscope or visual observation.

Analysing the EO harmonics should infer the phase properties of LC, switching properties, phase transitions. In case of linear (polar) EO response, only the fundamental (first) harmonic should be present, while even harmonics should be zero. If the response is linear and its switching time is much less than the period of the applied wave, the amplitude ratio between the first and third harmonic of the signal should be equal, for applied square wave. Alternatively, if the material does not show fast enough response the amplitude of the higher odd harmonics will be lower compared to the previous condition. However for asymmetric (non-linear) EO responses, even harmonics should also be present.

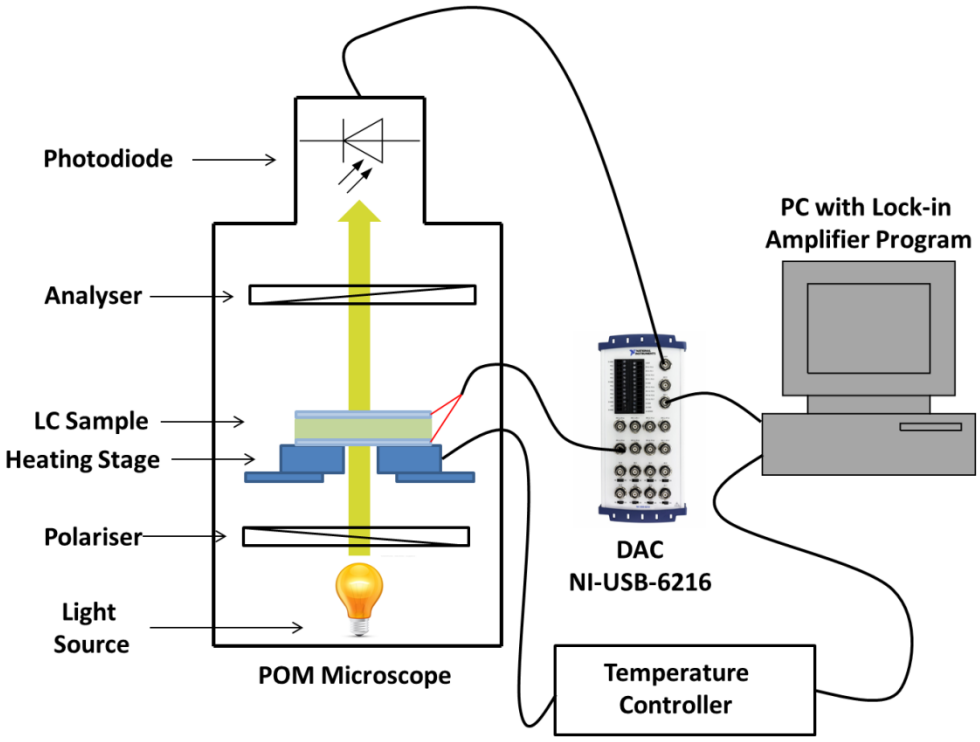

Figure 2.10 Schematic representation of Electro-Optic spectrometer setup.

The transmitted intensity I without application of the electric field across the cell is given by (ref),

$$I = I_0 \sin^2(2\alpha)\sin^2\left(\frac{\pi \Delta n d}{\lambda}\right) \tag{2.18}$$

where I_0 is the intensity of the light source, α is the angle that the rubbing direction of the LC makes with the polariser, Δn is the birefringence, d is the cell gap and λ is the wavelength of the light source. When an electric field is applied, the transmitted intensity varies linearly with the apparent tilt (θ_{ind}) induced by the applied field, $\delta\alpha = \theta_{ind}$. On differentiating Equation (2.18) with respect to the α, leads to,

$$\delta I = 2I_0 \sin 4\alpha \sin^2\left(\frac{\pi \Delta n d}{\lambda}\right)\theta_{ind} \tag{2.19}$$

On dividing Equation (2.19) by Equation (2.18) and by setting $\alpha = 22.5°$,

$$\theta_{ind} = \frac{\delta I}{4I} \tag{2.20}$$

In this thesis we mainly focus on measuring the high resolution field induced optical axis tilt as a function of temperature for understanding the nature of the phase transition in FLCs. Detailed studies and results are given in the following chapters.

2.5 Measurements of the Spontaneous polarisation:

2.5.1 Square wave technique:

A schematic diagram of the circuit used for the field induced polarisation of a FLC is shown in Figure 2.11. The current *i* passing through the LC cell is integrated by a capacitor C_1 connected in series with the cell and a signal generator. During the measurement a rectangular (Square) wave form of alternating signal is applied [52,53].

Let us assume that the LC is in the smectic phase and the molecules are orientated parallel to the ITO electrodes of the cell. When a voltage *U* is applied to the electrodes, the polarisation vector tends to directed in the direction of the electric field *E*, while the azimuthal angle ϕ between them tends to be zero. In the process of the reorientation of the polarisation (*P*), there occurs a repolarisation current i_p associated with a change in the surface charge on the electrodes [52,53]. In addition, through the cell, there passes a current i_r which is associated with the ionic conduction of LC. The third component is the displacement current i_c, related to the cell capacity recharging, consequently, the instantaneous value for the total current through the cell can be presented as the sum of the three currents such that:

$$I = i_r + i_c + i_p = \frac{U}{R} + C\frac{dU}{dt} + A\frac{dP}{dt} \tag{2.21}$$

where C is the capacitance of the cell. A and R are the area and the resistance of the cell, respectively.

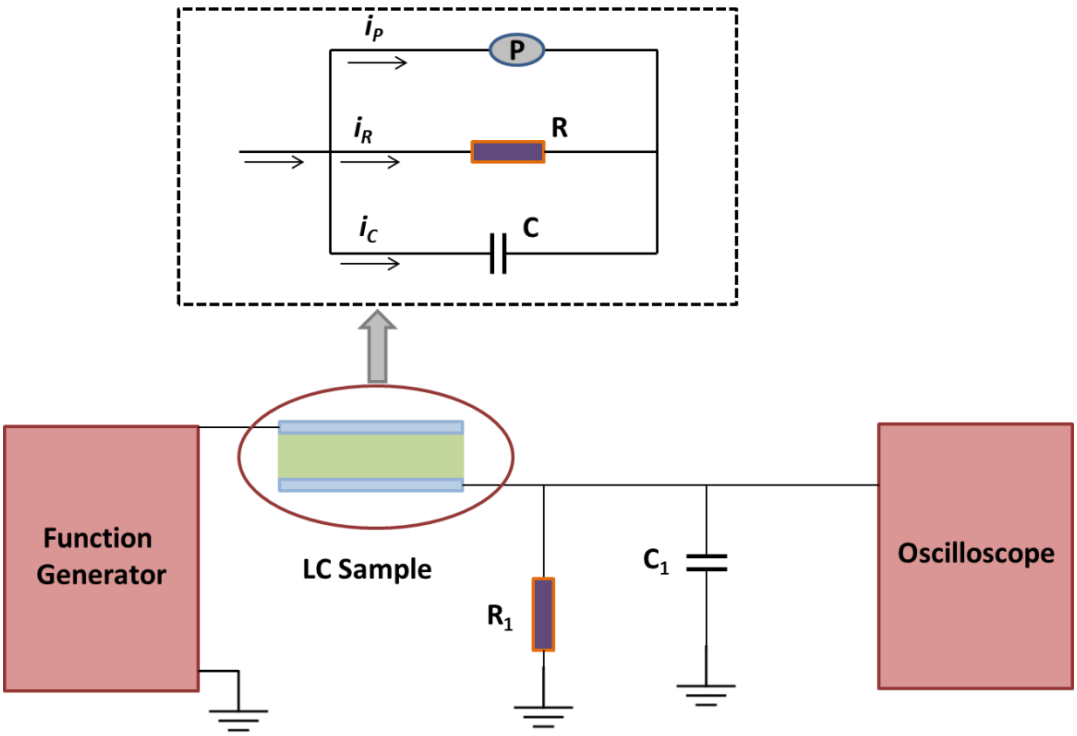

Figure 2.11 Schematic of Polarisation Measurement setup

The instantaneous value for the voltage across the capacitor C_1 is,

$$U_{out} = -\frac{1}{C_1}\int_0^t idt = \frac{U}{RC_1} + \frac{2UC}{C_1} + \frac{PA}{C_1}\cos(\phi(t)) = U_r + U_c + U_p \tag{2.22}$$

where $t = 0$ represents the moment of reversing the sign of the electric field applied across the cell. Figure 2.12 shows the output voltage across the capacitor C_1.

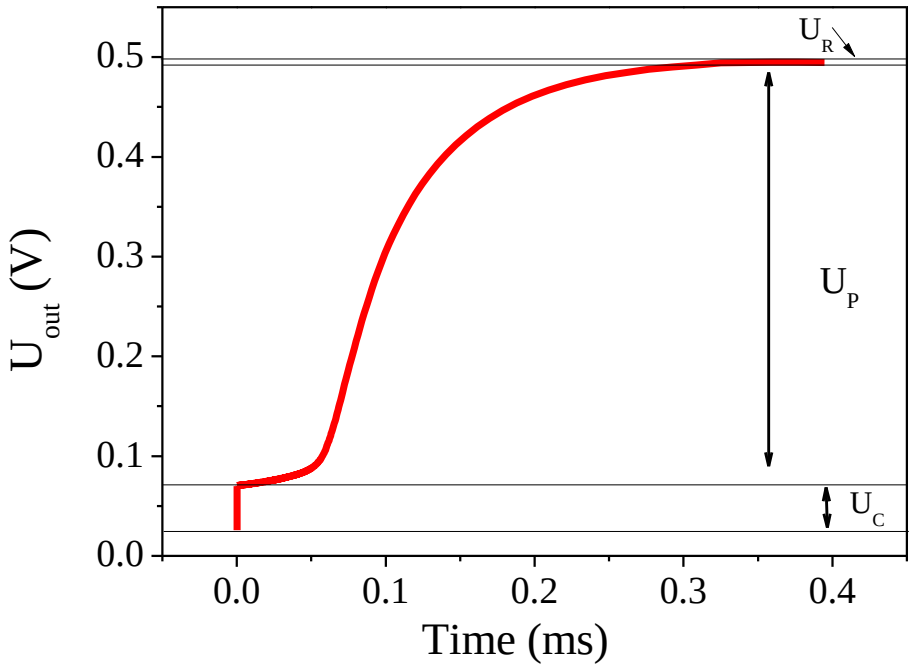

Figure 2.12 Representative oscillogram of the output signal from the capacitor.

The voltage generator time constant is much shorter than the oscilloscope sweep time; as a result, the oscillogram shows U_c as an instantaneous jump. U_c is followed by a smooth rise in the voltage due to integration of the repolarisation current I_p and the conductivity I_r. The effect of I_r can be eliminated by introducing a variable resistance R_1 into the measuring circuit as shown in the Figure 2.11. By measuring the value of U_p we can find the polarisation using the formula,

$$P = \frac{U_p C_1}{2A} \tag{2.23}$$

Chapter 3

3. Effects of Chiral Doping

3.1 Introduction

The origin of spontaneous polarisation ($\boldsymbol{P_S}$) in SmC* phase of a FLC is due to the presence of chirality in the constituent molecules and the presence of permanent dipole moment normal to molecular long axis, which is responsible for the symmetry breaking, leading to a formation of a helical structure [54]. Such condition can also be achieved in SmC phase of an achiral LC by mixing one or two suitable chiral dipolar additives [55-57]. Such mixtures will exhibit the same point symmetry ($\mathbf{C_2}$) as the single component chiral FLC. Thus, by doping a chiral agent to an achiral liquid crystal host we can induce the ferroelectricity; with same order of magnitude of $\boldsymbol{P_S}$, or even higher than that of a single component FLC [58]. The position of the chiral centre in the dopant plays an important role in inducing the ferroelectricity in the mixture, detailed studies and review is given in Ref [55]. In this work we have chosen a dopant having the chiral centre located in the flexible chain attached to the rigid molecular core, similar to Type 1 in Ref [55].

From an industrial point of view, it is much easier and cost effective to synthesize achiral LC having SmC phase and mix with chiral dipolar additives [54]. The chiral dipolar additive determines the $\boldsymbol{P_S}$ value, in some cases the dopant possess a complicated molecular structure, or the dopant may not be mesogenic [54]. It also depends on the molecular tilt of the host matrices, chiral moiety of the additives and the mutual compatibility of molecular lengths of the host and the additive. The mixture should satisfy the required temperature range, stability and the optical properties. In terms of temperature range adding an additive can be useful to lower the phase transition temperature of the host LC, mostly this is used to bring the phase transition near room temperature for convenience. For a small concentration of the chiral additive, $\boldsymbol{P_S}$ is proportional to the doping concentration (x_d). The induced

chirality naturally twists the director of the achiral SmC matrix and the corresponding twist is also proportional to the x_d. In this case, the situation is similar to the induced chirality in the nematic mixtures [59].

Various achiral LCs showing low layer shrinkages have been reported [20,37]. Also studies of chiral FLCs with chiral dopant for stabilising low pitch SmC* phase and inducing low layer shrinkage can be found in [60]. Such materials are excellent candidates for de Vries type LCs. However, chiral mixture studies with such achiral de Vries type LC is seriously lacking. In this chapter we present the experimental results of two known achiral de Vries type LC (C4 and C9) mixed with a chiral additive (DR98S) in varying weight percentages. We study the influence of chiral additive in achiral host through various different characterisation techniques [61]. We analyse the temperature dependent layer thickness, Electro-Optics (EO), $\boldsymbol{P_S}$, birefringence and the induced optical tilt angle measurements.

3.2 Materials under investigation

Achiral materials studied in this chapter, C4 and C9, are constituted by a 5-phenylprimidine core with a trisiloxane terminated undecycloxy chain on one side and the alkoxy chain in the opposite side that belongs to a homologous series. This series was originally synthesised by Stuttgart group [37] in 2010. They studied the layer thickness of the homologous series of 8 compounds and effect of frustration between the structural element promoting SmC phases and to that promoting the SmA phase. The low values of the layer shrinkage and reduction factor '**R'** (defined later in this chapter) show that these compounds belong to de Vries type LC. Later in 2011, X-ray group in Kent, carried out a high resolution X-ray studies for C4 and C9 [62,63]. Their studies showed the direct observation of diffuse cone behaviour in

SmA phase. In this chapter we used the compounds C4 and C9 which was re-synthesised by our project collaborator research group in Queens University Belfast.

The molecular structure of C4 and C9 is given in Figure 3.1 and the phase transition temperatures are given in Table 3.1.

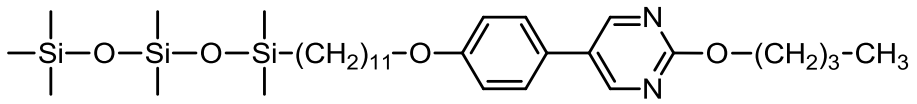

(a)

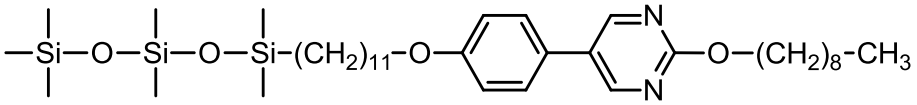

(b)

Figure 3.1 Molecular structures of (a) C4 and (b) C9.

Table 3.1 Transition temperatures in °C of achiral C4 and C9. Abbreviations: Cryst = crystalline solid; Iso = isotropic liquid.

Material	Phase sequence
C4	Cryst 35 ^{o}C SmC 57 ^{o}C SmA 79 ^{o}C Iso
C9	Cryst 51 ^{o}C SmC 73 ^{o}C SmA 76 ^{o}C Iso

The above shown achiral compounds are individually mixed with a chiral additive named DR98S in different weight percentages. The molecular structure of DR98S is shown in Figure 3.2. The structure of DR98S is very similar to the achiral ones. A chiral centre in introduced in the alkoxy chain for the C6 structure from the homologous series. This dramatically changes the phase transition temperatures of the compound and mesogenic property of the system. DR98S exhibits isotropic liquid phase in the room temperature and when cooled down it crystallises at 21 °C

as shown in the DSC thermogram (Figure 3.3). The 'S' in DR98S implies the major composition is S isomer. The enantiomeric ratio of DR98S is 98.5% of S and 1.5% of R.

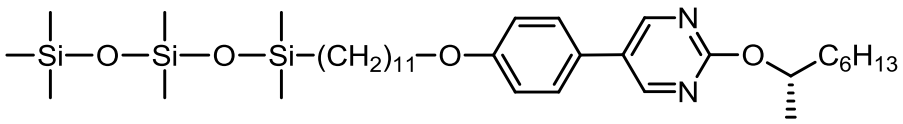

Figure 3.2 The molecular structure of the chiral dopant DR98S.

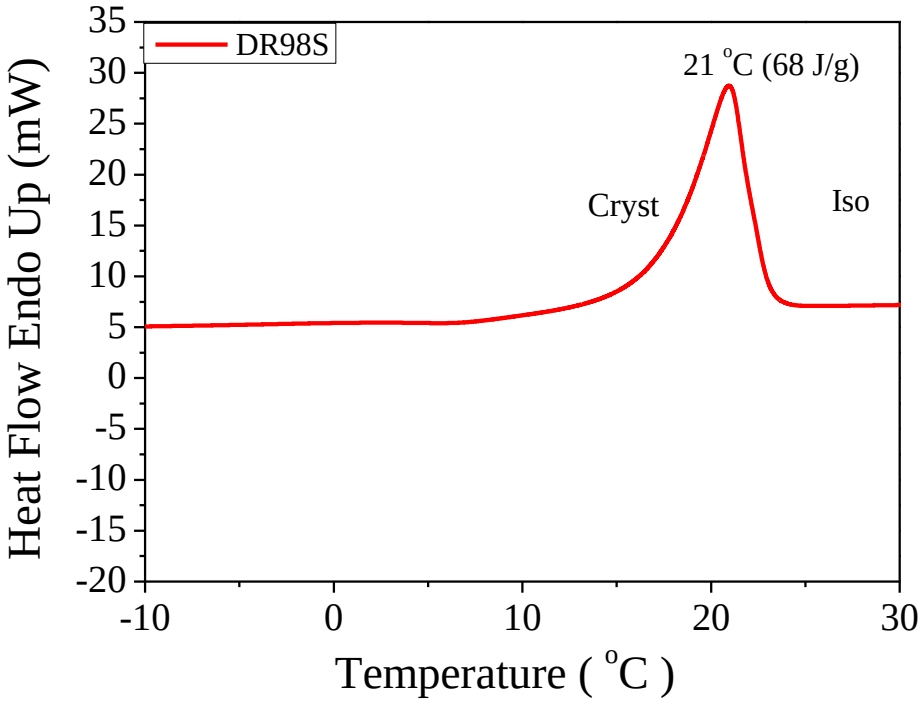

Figure 3.3 DSC thermogram of the chiral dopant DR98S at a scan rate of 10 °C/min with peak temperature and enthalpy of transition is shown in bracket.

3.3 Layer thickness measurements

3.3.1 X-ray diffraction studies

On the basis of the hard-rod approximation model of calamitic LC molecules, the layer thickness d_C in SmC phase with a tilt angle θ is related to the layer thickness in the SmA phase d_A as:

$$d_C = d_A \cos\theta \tag{3.1}$$

In conventional smectics d_A can be approximately equal to the molecular length '*l'*. However in de Vries type LCs this may not hold true, since the molecules are already tilted in the SmA phase, $d_A < l$.

By knowing the layer thickness at SmA-SmC phase transition temperature 'd_{AC}' and the lowest value of the layer thickness in SmC phase, one can estimate the maximum layer shrinkage in % for a given smectic LC. As discussed earlier the conventional LC would have layer shrinkage, as high as ~13% while de Vries type LCs should have layer shrinkages as low as ~1%. Therefore estimating the layer shrinkage is an important de Vries characteristic.

In 1999, Radcliffe *et. al.* [64] gave an empirical method to characterising the de Vries type of liquid crystals based on the layer thickness data and induced optical tilt angle data. The ratio known as the reduction factor can be defined as,

$$R \equiv \frac{\delta(T)}{\theta_{indsat}(T)} \equiv \frac{\cos^{-1}[d_C(T)/d_{AC}]}{\theta_{indsat}(T)} \tag{3.2}$$

where $\delta(T)$ is the maximum molecular tilt angle at the given temperature T, $d_C(T)$, the layer thickness at temperature T in SmC phase, with respect to the layer thickness

(d_{AC}) at SmA-SmC phase transition and θ_{indsat} is the saturated optical tilt angle in SmC at the given temperature induced by the application of electric field. The reduction factor can be considered as a figure of merit for the LC for its performance in the SSFLC (surface stabilised ferroelectric liquid crystal). The ideal de Vries LC with zero layer shrinkage should have R=0.

The temperature dependent layer thickness for pure achiral C4 and C9 was first measured by Roberts *et. al.* [37] and is shown in the Figure 3.4.

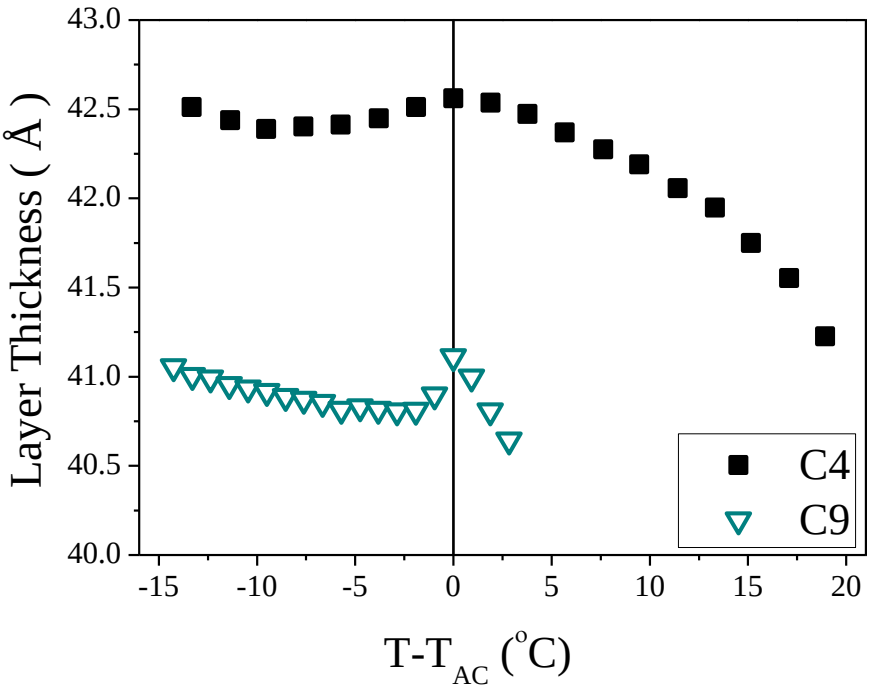

Figure 3.4 Smectic layer thicknesses of achiral C4 and C9 as a function of reduced temperature. (T_{AC} is SmA-SmC phase transition temperature)

We added chiral dopant DR98S up to 15% w/w to the two pure compounds. The temperature dependent layer thickness measured using X-ray diffraction for the mixtures are shown in Figure 3.5. For comparison, the data are plotted along with the layer thickness data of the pure achiral LC's.

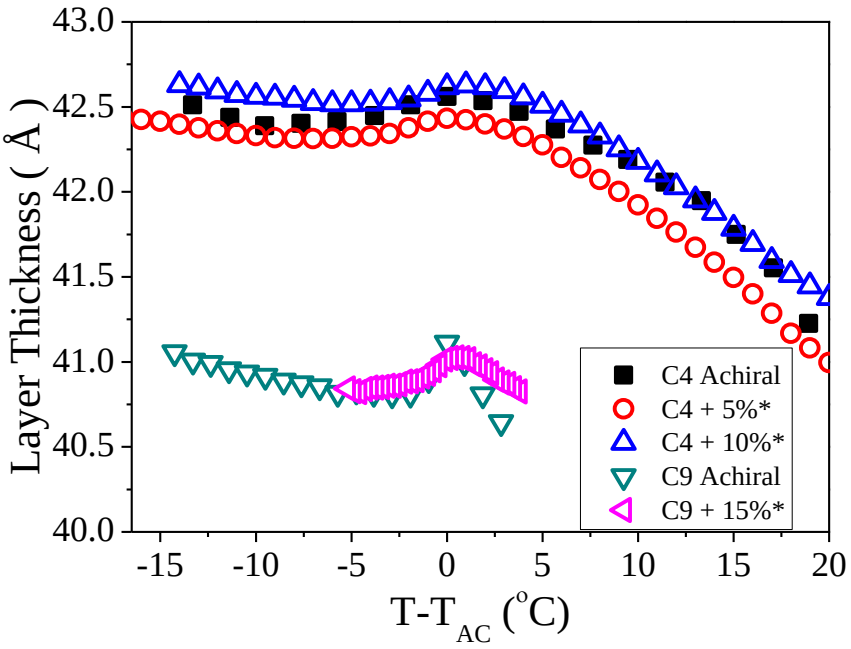

Figure 3.5 X-ray layer thickness of different chiral mixtures plotted along with the achiral layer thickness data as a function of the reduced temperature. (Here C4 + 5%* denotes 95% of achiral C4 is added with 5% of DR98S chiral dopant and the same for other mixtures)

3.3.2 Free-standing Film studies

The FSF thickness measurement is a complementary method to XRD, developed in the laboratory to obtain high resolution temperature dependent bulk film thickness using the FSF technique.

The FSF optical thickness for pure achiral and chiral mixtures of C4 and C9 as a function of the reduced temperature is shown in Figure 3.6. All the FSF optical thickness data have been normalised at the SmA-SmC phase transition point to draw a better comparison.

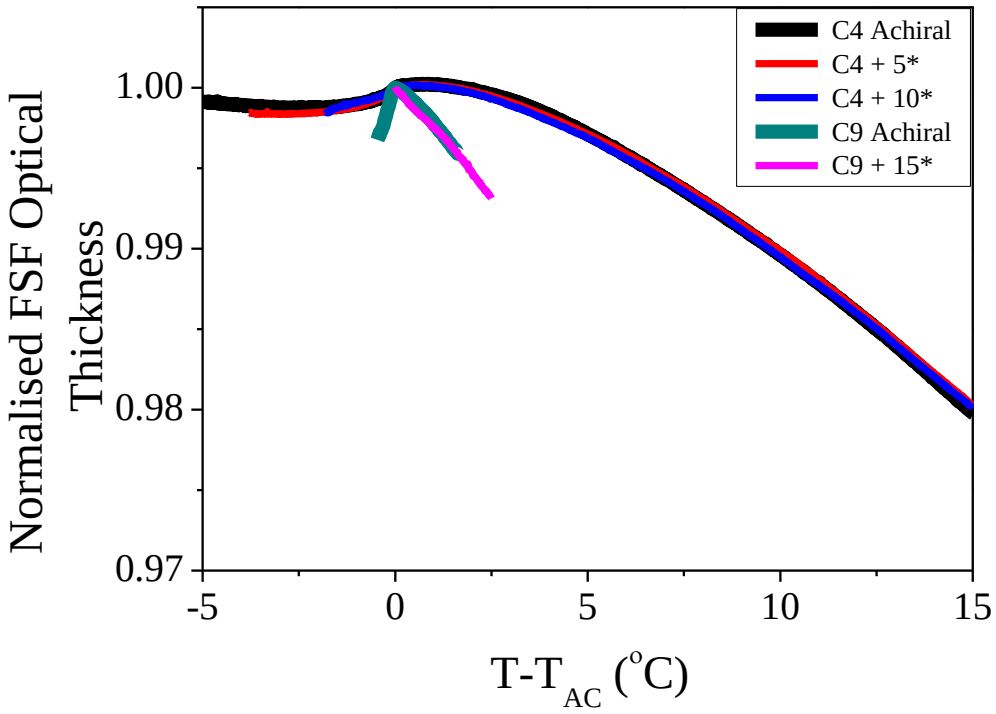

Figure 3.6 Normalised optical thickness of FSF's of achiral and chiral mixtures of C4 and C9.

In order to compare the thickness data obtained from two different techniques, the FSF optical thickness data are normalised with the X-ray layer thickness at SmA-SmC phase transition point for C4 mixtures shown in Figure 3.7. This shows that in SmA phase both FSF and X-ray thickness data follow the same trend (change is within the experimental error). However, in SmC there is a large deviation in FSF thickness data compared to the X-ray layer thickness [65]. This is due to the change in the effective refractive index caused by the appearance of the tilt angle in SmC phase. In SmA, this difference is negligibly small due to the uniaxial nature of SmA (in Homeotropic alignment).

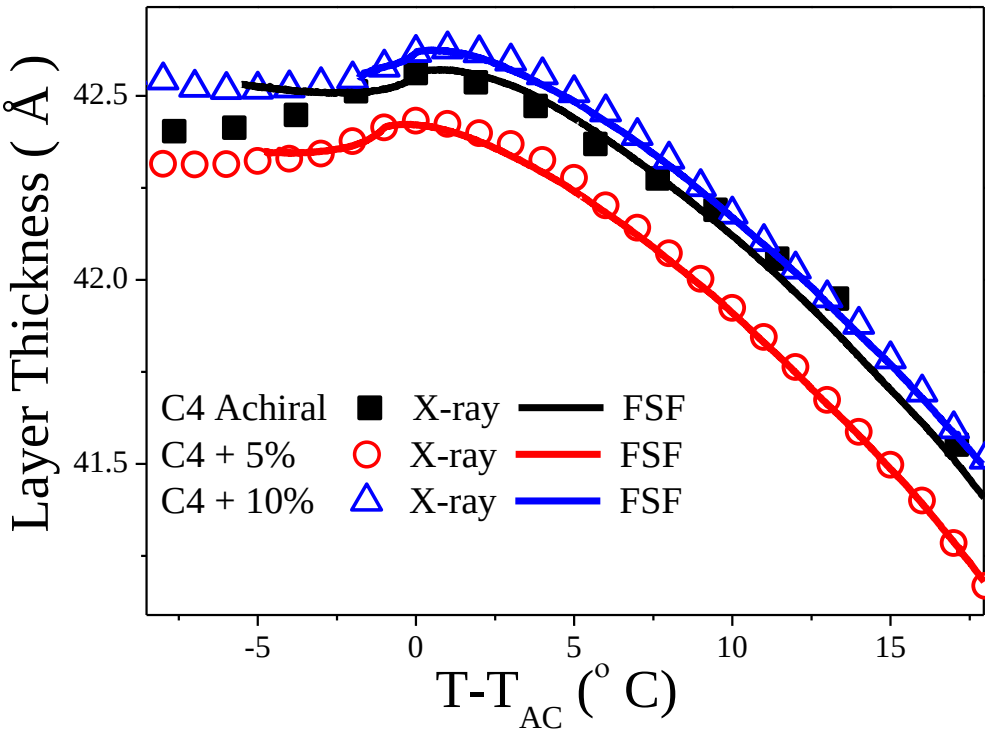

Figure 3.7 Normalised FSF optical thicknesses with the X-ray layer thicknesses for C4 pure and chiral mixtures, respectively.

All the estimated layer shrinkages and reduction factors from X-rays layer thickness data for the pure and chiral mixtures are given in Table 3.2. The layer shrinkage is estimated from the layer thickness at SmA-SmC phase transition and minimum value of the layer thickness obtained in the SmC phase, respectively. The θ_{indsat} is the measured saturated optical tilt angle in SmC phase at the given temperature with an electric field of 5 V/μm applied across a 9 μm planar-aligned cell. θ_{indsat} is measured at a temperature corresponding to the minimum value of d_C. These values suggest that these mixtures are one of the best known de Vries LCs in terms of the low values of layer shrinkage [37].

From the above smectic layer thickness studies we would like to emphasize that introducing a chiral additive or chiral dopant does not alter the characteristic low layer shrinkage of the achiral smectic LC hosts up to 15%.

Table 3.2 Layer shrinkage and reduction factors for achiral and chiral mixtures of C4 and C9.

Material	T_{AC} (°C)	d_{AC} (Å)	d_C (Å) at T- T_{AC}	Layer Shrinkage	θ_{indsat} (degrees)	R
C4 pure	57	42.5	42.3 at -9 °C	~0.5%	24	0.23
C4 + 5%	50	42.4	42.3 at -7 °C	~0.2 %	20	0.20
C4 + 10%	39	42.6	42.5 at -6 °C	~0.2 %	24	0.16
C9 pure	73	41.1	40.8 at -5 °C	~0.7%	40	0.14
C9 + 15%	56	41	40.8 at -4 °C	~0.5 %	25	0.22

3.4 Critical behaviour of the SmA-SmC phase transition

Over the last few decades there has been a considerable effort made to understand the physics of liquid crystal's phase transitions [2]. From an application point of view, it is important to predict the behaviour of temperature dependent macroscopic parameters such as the order parameters, pitch, tilt angle, elastic coefficients etc. Since these parameters show drastic changes in the vicinity of the phase transition [66].

De Gennes showed that the SmA-SmC transition is analogous to the behaviour of a superfluid helium. Based on that analogy he introduced an onset of an order with two physical parameters. These two parameters can be described by a complex number as given below:

$$\psi = \omega e^{i\phi} \tag{3.3}$$

Here ω is the magnitude of the tilt angle and ϕ is the azimuthal tilt. This would lead to following expectations; that SmA-SmC transitions is discontinuous (first order) phase transition. Also below T_{AC}, the tilt angle should vary according to the power law given below:

$$\omega = C|t|^{\beta} \tag{3.4}$$

where $t = (T - T_{AC})$ is the reduced temperature, C is a constant and $\beta \simeq 0.35$ known as order parameter critical exponent. While above $T_{AC,}$ the electric field induced tilt angle should vary exponentially as given by:

$$\omega = \frac{C}{t^{\gamma}} \tag{3.5}$$

here C is a constant and $\gamma \simeq 1.32$ is the susceptibility critical exponent. Note ω and θ_{ind} are the same [2].

De Gennes also explained the critical behaviour of the correlated volume near the phase transitions. The correlation length can be defined as the length over which the molecular dynamics are correlated. This range in volume specifies a 'correlated domain'. Correlation length is denoted by ξ. The variation of the correlation length near the phase transition is defined using the exponent υ ,

$$\xi_X \simeq \xi_0 t^{-\upsilon} \tag{3.6}$$

here, ξ_0 is a constant for a material and the exponent is supposed to be $\upsilon \simeq 0.66$ for X specifying an axis in the given frame of reference. De Gennes derived a relation between the critical exponents, as $\gamma \simeq 2\upsilon = 2(0.66) = 1.32$ for a two dimensional correlated systems. This has been verified using different experimental techniques for conventional smectic LCs [67].

On the other hand, de Vries type LCs show correlation in all the three dimensions. For ideal de Vries type LC the exponent should be $\gamma \simeq 3\upsilon = 2$, the correlated volume is given by $\xi_V = \xi_X . \xi_Y . \xi_Z$ [68]. However, de Vries type LC does not show long range correlation along the third dimensions (across the smectic layers) as seen within the layer itself, hence the value of γ would lie in between $2 \geq \gamma > 1.32$. This has been consistently reported in different experiments carried out to estimate γ [69,70]. Note: For the first order phase transition the T_{AC} will not a have

fixed value, therefore it is necessary to release the T_{AC} as a fitting parameter while estimating the critical exponent, this is indicated with a * symbol (T_{AC}*).

3.5 EO Measurements

In order to estimate critical exponent of the susceptibility in SmA phase of the chiral mixtures, we measured θ_{ind} as a function of temperature as explained below:

As discussed in 2.4.2 the rubbing direction of a planar-aligned cell is set at an angle (α in Equation 2.18) of 22.5^{o} to the polarizer in order to obtain the maximum change in intensity as per Equation 2.19. Measurements are carried out by applying a sinusoidal signal of amplitude 0.1 $V_{0\text{-}Pk}$/μm, frequency 22 Hz, to a planar-aligned cell of thickness 4 μm with a cooling rate of 0.1 °C/min. The θ_{ind} values as a function of the reduced temperature for chiral mixtures of C4 and C9 are shown in Figure 3.8. These are fitted to Equation 3.5 to estimate γ

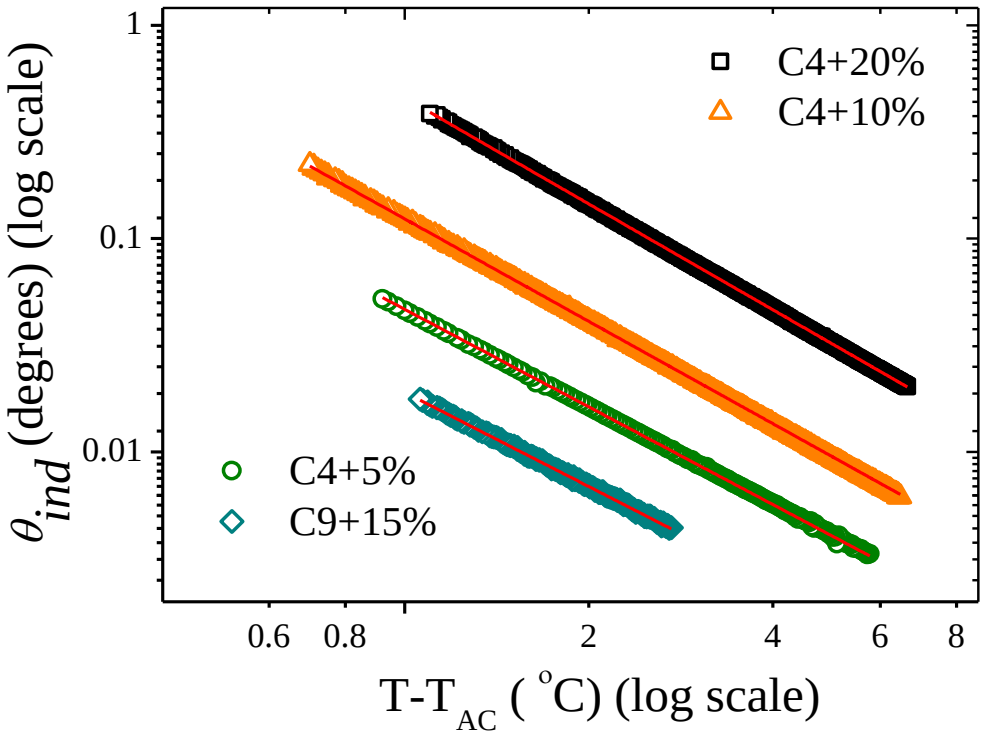

Figure 3.8 Log-Log plot of θ_{ind} as a function of reduced temperature for chiral mixtures of C4 and C9. Symbols – Experimental data. Solid line – Power law fit.

For the small amplitude of applied electric field we can expect a linear relationship between the applied fields and induced optical axis tilt θ_{ind} in SmA phase, known as the electro-clinic effect [71]. This can be expressed as,

$$\theta_{ind} = e_c E \tag{3.7}$$

where e_c is the electroclinic co-efficient and E is the applied electric field in V/µm. SmA phase of de Vries type LC liquid crystals is known to exhibit a large EC coefficient [31,41,70,72]. γ and e_c are estimated for all the mixtures and are tabulated in Table 3.2. Also e_c is plotted against the doping concentration, and is shown in Figure 3.9.

Table 3.3 SmA-SmC transition temperature (T_{AC}) and the estimated γ and e_c.

Mixture	T_{AC}* (^oC)	γ	e_c (mdeg μm V^{-1}) at ($T-T_{AC}=1.1^oC$)
C4 + 5%	49.23	1.52	0.39
C4 + 10%	39.54	1.59	1.06
C4 + 20%	36.36	1.64	3.85
C9 + 15%	56.94	1.46	0.16

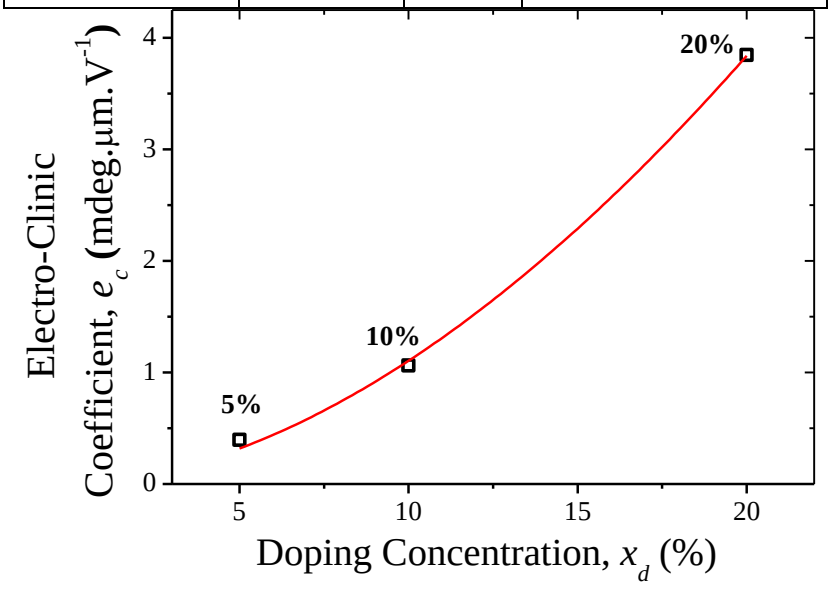

Figure 3.9 Electroclinic co-efficient e_c as a function of doping concentration x_d at temperature T= (T_{AC}+1.1) °C for chiral mixtures of C4. Square symbols – Estimated values. Solid line – data fit to the Equation 3.8.

Behaviour of e_c surprisingly follows a power function rather than a linear function of the increase with respect to the doping concentration. The relationship between e_c and the doping concentration x_d can be given by,

$$e_c = ax_d + c(x_d)^{\rho} \tag{3.8}$$

Data in Figure 3.9 are fitted to above Equation 3.8 We obtain ρ = 1.94, a = 0.002 and c = 0.001 *mdeg μm* V^{-1}. The first term represents the linear relationship between e_c and x_d for low doping concentration and the second term represents non-linear dependence. This relationship can be useful for chirality sensing applications [28].

3.6 The Spontaneous polarisation measurements

Measurements of spontaneous polarisation $\boldsymbol{P_S}$ are made using 4μm planar-aligned cell of area 25 mm^2. A square wave of 1 $V_{0\text{-}Pk}$/μm with a frequency 102 Hz is applied across the cell, current through the cell is integrated by a capacitor of capacitance 0.047μF. $\boldsymbol{P_S}$ can be estimated by recording voltage as a function of time using oscilloscope as explained in the experimental section.

Figure 3.10 shows the temperature dependence of the spontaneous polarisation $\boldsymbol{P_S}$ for different chiral mixtures of C4. On cooling *Ps* starts growing after SmA – SmC* phase transition and reaches saturation on further cooling in SmC* phase. The overall magnitude of $\boldsymbol{P_S}$ increases with increase in chiral doping concentration. This is a clear evidence of the induced ferroelectricity in achiral de Vries type LC.

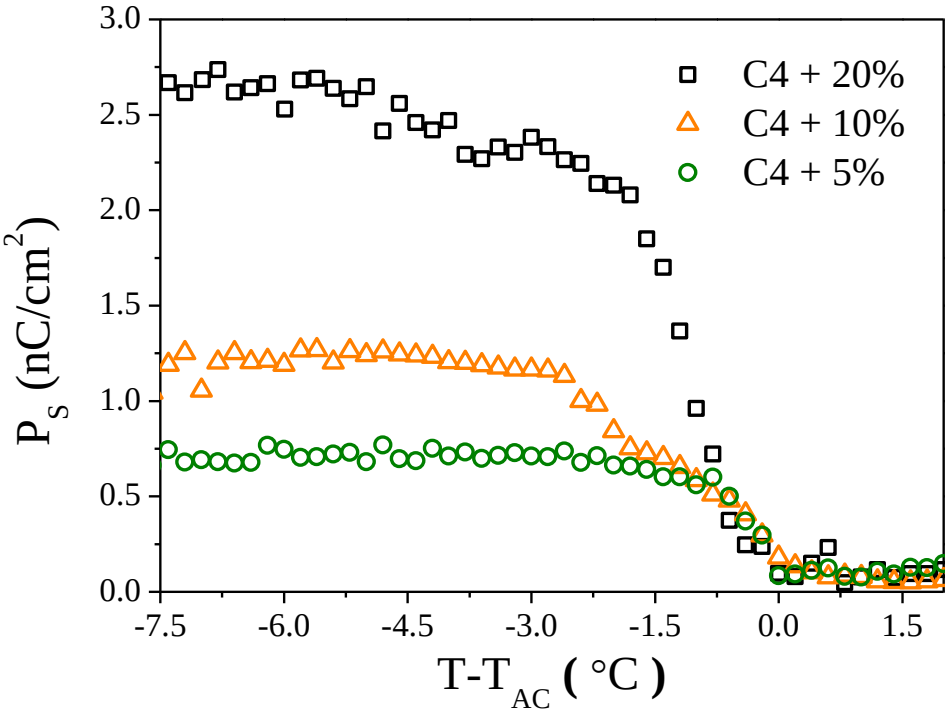

Figure 3.10 A plot representing Spontaneous polarisation P_s as function of the reduced temperature for C4 chiral mixtures.

Earlier we found that a change in layer thickness, if any, is independent of the dopant concentration. Figure 3.9 shows that we can alter the polarisation with doping concentration; this implies that we can tailor make $\boldsymbol{P_S}$ of the system while maintaining advantages of the low layer shrinkage.

3.7 Birefringence measurements

We focus our studies of a single mixture to carry out further detailed de Vries characterizations. The following experimental results are carried out using C4+10% chiral mixture.

De Vries type LC shows characteristic temperature dependent birefringence trend. The temperature dependent birefringence measurements are carried out using planar-aligned cell of thickness 9 µm using ATP technique as described in the

experimental section. Figure 3.11 shows the temperature dependent birefringence (Δn) in the absence of external electric field.

From Figure 3.11, we can infer that on cooling from the Iso to SmA, Δn increases with a reduction in temperature. This usual phenomenon is due to an increase in the order parameter (thermally induced molecular fluctuation decreases on cooling, as a result the order parameter increases). But within the SmA phase itself, birefringence shows a reversal of this trend. On further cooling the birefringence decreases instead of increasing. Nevertheless, this indicates the appearance of molecular tilt with degenerate distribution in the azimuthal angle ϕ. Since the distribution is spatially averaged in the optical experiments, the effective value of the birefringence is decreased. This phenomenon is typical of the de Vries smectics and explained in [34]. A similar non-monotonic trend is observed in the layer thickness for C4+10% (Figure 3.7). The non-monotonicity in the birefringence and the layer thickness is due to the emergence of the molecular tilt with respect to the layer normal.

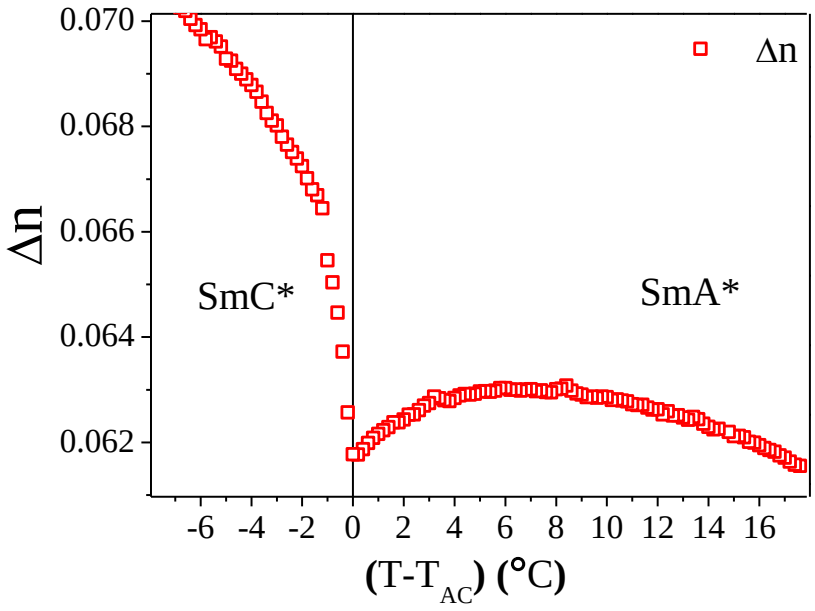

Figure 3.11 Measured birefringence in the absence of electric field as a function of reduced temperature for C4+10% chiral mixture.

3.7.1 Electric field dependence of Δn and θ_{ind}

It is known that, in chiral de Vries SmA* phase, the applied electric field can lift degeneracy in the azimuthal angle which is responsible for ~ 15% increase in the birefringence near the SmA-SmC phase transition temperature [34].

Similar results are observed in the present work with achiral + chiral mixtures. For C4 + 10% chiral mixture, field of 14 V/μm applied brings about ~ 6% increase in the birefringence with respect to the zero field birefringence value (Figure 3.13 (a)). This is also evident in the observed interference colours in a 9 μm planar-aligned cell textures under POM (Figure 3.12).

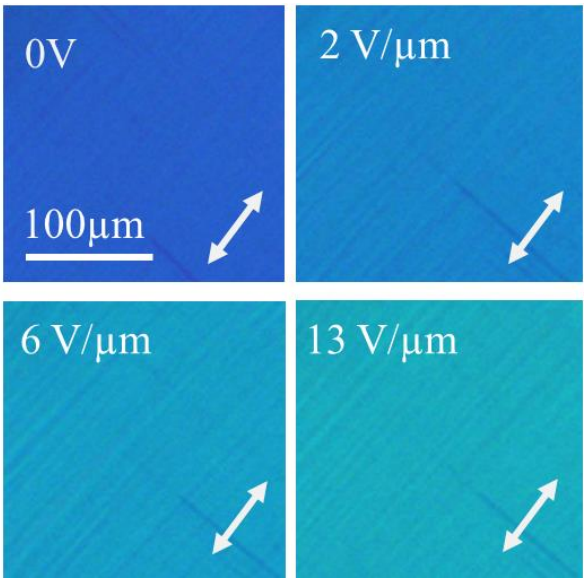

Figure 3.12 Textures captured using POM under crossed polarisers state for C4+10% mixture at T_{AC} + 1 °C (SmA) using a 9-µm planarly aligned cell for different applied electric fields. The double-headed arrows represent the rubbing direction. Scale bar: 100µm.

Figures 3.13 (a) and (b) show plots of electric field dependent birefringence (Δn) and optical axis (θ_{ind}), for selected temperatures in the SmA phase for C4+10%.

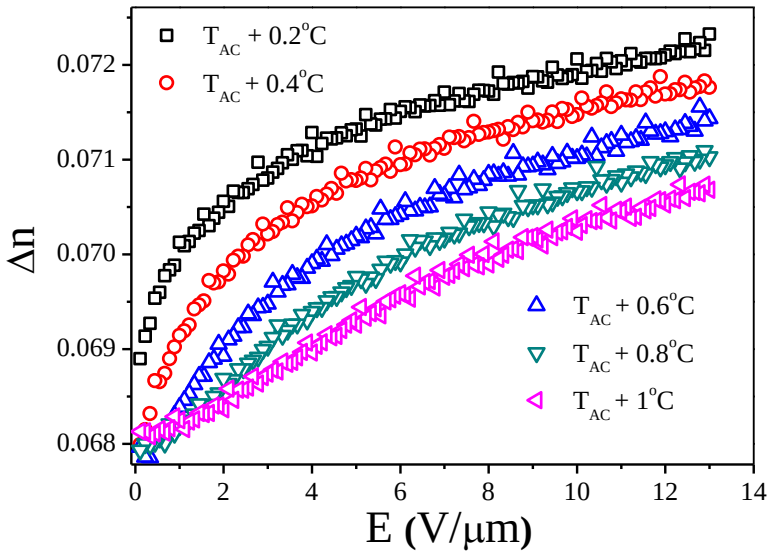

(a)

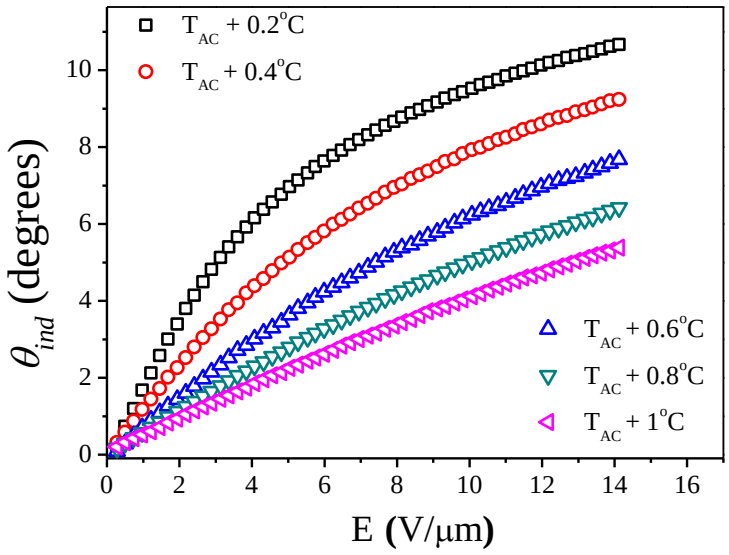

(b)

Figure 3.13 a) Electric field dependence of birefringence, Δn b) Electric field dependence of optical axis tilt, θ_{ind} , for C4+10% chiral mixture. Both shown for selected temperatures in SmA* phase up to a field of 14 V/μm.

Both Figure 3.13 (a) and (b) show that for temperatures close to Iso-SmA transition in the SmA range, we observe a linear increase in the apparent tilt angle (θ_{ind}) and the birefringence (Δn) with an increase in the applied electric field [73,74]. On approaching the SmA* - SmC* transition both parameters follow a Langevin-type increase. On further cooling, for temperatures close to the SmA*-SmC* transition, increases in both θ_{ind} and Δn are rapid and the saturation occurs for higher fields. Such electric field dependent behaviour is typical of de Vries type smectic phase. These results are rather similar to those of chiral de Vries type smectics [42].

3.8 Conclusions

To summarise, we give a number of experimental results for chiral mixtures of C4 and C9 formed from achiral homologous series. Measurements of the smectic layer thickness using two different techniques, X-rays and FSF for pure achiral and their mixtures with a chiral additive DR98S show that, adding a dopant up to 15%

w/w does not change the smectic layer thickness of the host. Any change observed is within the experimental error. However, the electro-optics and spontaneous polarisation studies for the mixtures show an increase in the magnitude with an increase in the concentration of the chiral dopant, respectively. These indicate that we can induce and alter the polar nature of the mixture while preserving its characteristic low layer shrinkage with this particular dopant. In this particular work, this could be due to the chemical structural similarity between host and dopant. Adding chiral additive also provides freedom to control the phase transition temperatures. By increasing the chiral dopant concentration we could achieve a maximum of 20 °C decrease in the SmA-SmC phase transition temperature. Further characterisations like field dependent birefringence and the optical tilt angle shows that these mixtures exhibit the characteristics of chiral de Vries type smectic LCs. This satisfies the major motivation of the work, where the material properties can be tuned to the requirements. Here results are promising for the design of low cost FLC mixtures which can be used in electro-optic device applications. It may be remarked here that $\boldsymbol{P_S}$ is low enough and consequently we need to design and use better chiral dopants.

Chapter 4

4. Chiral De Vries Smectics

4.1 Introduction

The following chapters will mainly focus on to the chiral de Vries type smectic LCs. The study of FLCs steadily increased from 1980s. This is mainly due to the fact that FLCs possess many desirable features over nematics, One of the main advantages of FLCs enables these to switch faster (sub microsecond) than nematics (milli second) [75]. However, many researchers have observed defects in FLC based devices. Therefore, detailed investigations of chiral de Vries smectics have become a necessity not only from the application point of view but it is vital to understand the anomalous nature of the temperature and field dependence of the apparent tilt angle and the birefringence.

Early studies of the low layer shrinkage were all made in achiral LCs [20]. From 1980's [29] the study of chiral de Vries smectics began to appear.

Continued research in chiral de Vries smectics [30,76-79] revealed further characteristic differences compared to the conventional smectics. One of the most important characteristics of chiral de Vries smectics is the substantial increase in the field induced birefringence and the apparent angle tilt. In this thesis, the term Electro-Optic response generally refers to a plot of birefringence or the apparent tilt angle versus applied electric field. Bahr and Hepkke [38] were the first to model such a response using a simple Landau free energy function for a chiral ferroelectric LC showing the first order phase transition. However, they did not consider the diffuse cone or de Vries behaviour in SmA* phase. Later in 1999, Panarin *et. al.* observed a large field induced apparent tilt angle in SmA* phase, They described it in terms of a new phase, named as $SmC_{R,}$ where R stands for the random distribution of azimuthal angle but the molecular tilt angle is fixed at a particular temperature.

As discussed earlier in the introduction, several models appeared in order to describe the large EO response of de Vries type smectics. In this chapter we concentrate on the most recent model given by Shen *et.al.* [42]. We employ this model to two of the best known chiral de Vries smectics. We discuss the shortcomings of the model and point out the scope for improving the EO modelling.

This chapter can be divided in to two sections: in Section 1 we discuss all the characterisation results of a chiral de Vries LC and the EO models. Section 2 deals with an investigation based on the Infrared studies of two known chiral de Vries smectics.

Section 1

4.2 Materials under investigation

In this section, the experimental results obtained for MSi_3MR11 are given. The molecular structure and the phase transition of MSi_3MR11 temperature is shown in Figure 4.1. This material was first synthesised by Galli *et. al.* in 2005 [80]. It has been resynthesized by Queen University, Belfast group for this work. The NMR data of the newly synthesised sample shows that it is purer than the previously synthesised sample by Galli *et. al.*[80].

The mesogenic core of MR11 consists of biphenyl 2-chloro-3-methylpentanoate unit. Here 'M (mono-substituted)' stands for the number of siloxane end groups attached to the mesogen MR11.

The optimized geometry of MSi_3MR11 is shown in Figure 4.2. This is obtained by the density functional theory (DFT) using B3LYP method with a 6-31G

(*d,p*) level basis set. The optimization was carried out using GAUSSIAN 09 software package [81].

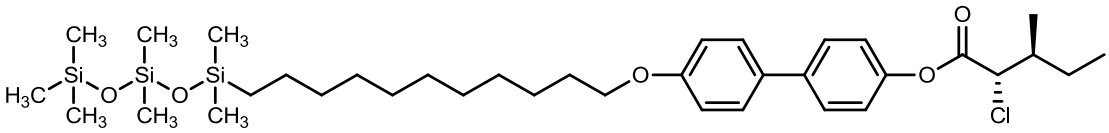

Cr **16ºC** SmC* **47ºC** SmA* **59ºC** Iso

Figure 4.1 Molecular structure and the transition temperatures in °C.

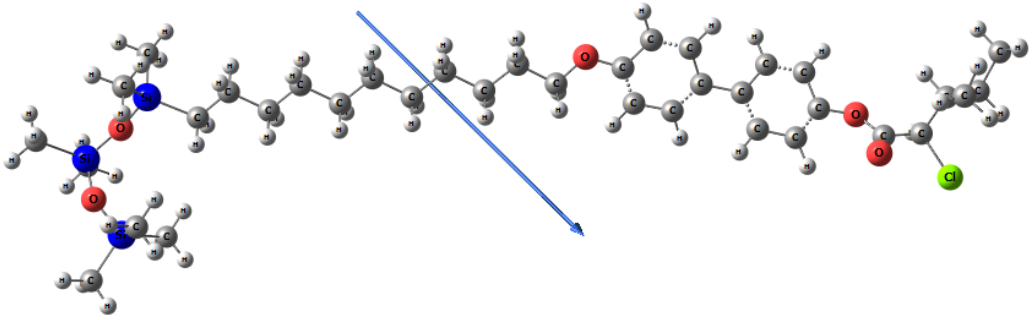

Figure 4.2 Optimized molecular geometry of MSi_3MR11. The arrow represents the direction of the molecular dipole moment (3.5 Debye).

The DSC thermogram obtained for MSi_3MR11 is shown in Figure 4.3. In both heating and cooling cycles, MSi_3MR11 exhibits three transition peaks. During the cooling cycle, enthalpy of the phase transition Iso-SmA* is -5.56 J/g, whereas that of SmA*-SmC* is -1.06 J/g. The minus sign signifies that energy is released during the phase transition on cooling. The enthalpies associated with the transition temperatures (first cooling and second heating rates of 10 ºC min^{-1}) show that the SmA*-SmC* phase transition is of weakly of the first order [82].

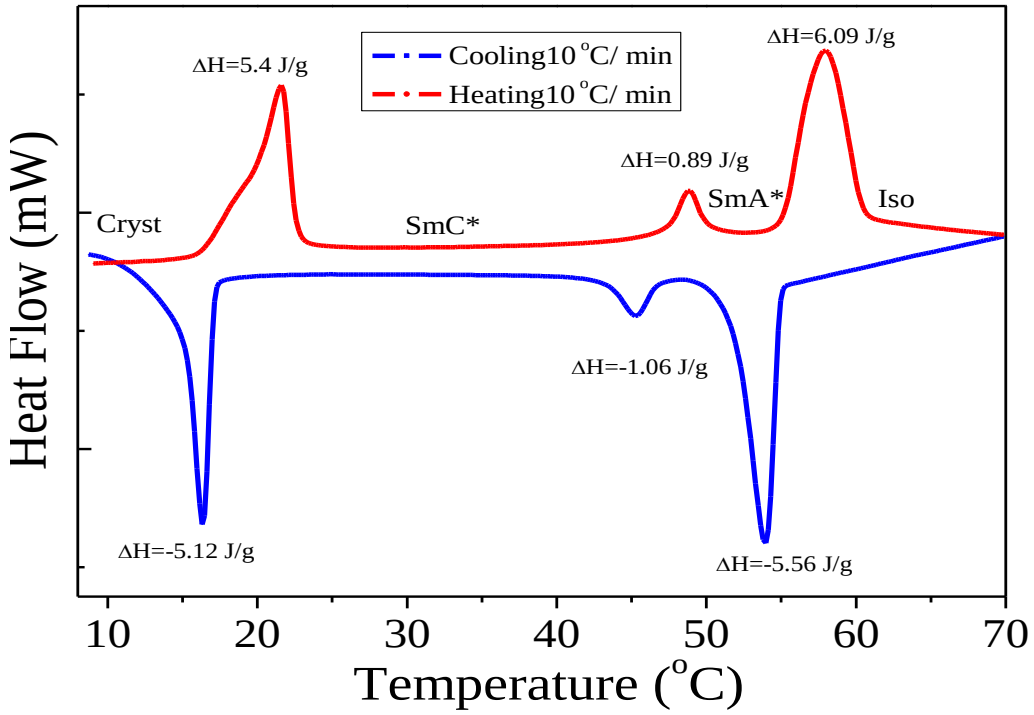

Figure 4.3 DSC thermogram of MSi_3MR11 obtained from cooling and heating with a rate of 10 °C/min.

4.3 Layer thickness measurements

4.3.1 X-ray diffraction and FSF studies

The X-ray diffraction study was performed using a 1.0-mm quartz capillary tube filled with MSi_3MR11 by Kooijman [62]. The tube was placed inside a Linkam hot stage (HFSX350-CAP) controlled with a resolution of 0.05 ºC using temperature controller (T95-HS) for temperature dependence studies of the layer thickness. The measurements were performed using a microfocus Rigaku Screen Machine (copper anode with a wavelength of 1.542 Å) and the diffraction patterns were recorded by a Mercury 3 CCD detector of resolution 1024×1024 pixels (size: 73.2×73.2 μm^2) placed approximately 73 mm away from the sample. The data were calibrated against silver behenate standards traceable to the National Institute of Standard and

Technology. Data were analysed using FIT2D software [83] and the background data (i.e., scattering from an empty capillary) was subtracted from the measured scattering data using *Mathematica* software.

The X-ray diffraction studies of SmA* phase of MSi_3MR11 shows a sharp Bragg layer reflection peaks in the small-angle region centred at ~39.6 Å and the second order reflection is centred at ~19.8 Å as show in in Figure 4.4. The orthogonal nature of the SmA* phase is confirmed by a pair of diffuse crescents in the wide angle-region located at ~4.6 Å perpendicular to the layer peak. Higher order peak appears in the SmC* phase at ~13.4 Å and there is no change in the position of the diffuse crescents, seemingly indistinguishable from the SmA* phase.

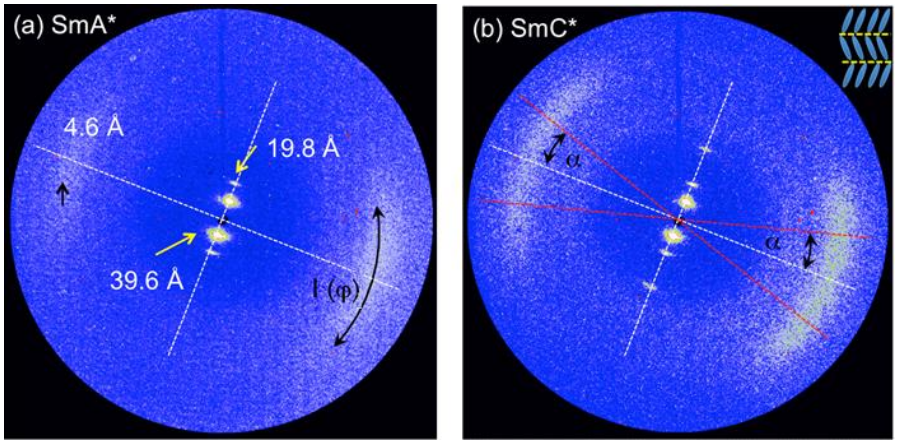

Figure 4.4 X-ray diffractions patterns of MSi_3MR11 in (a) SmA* phase (1.2 °C above the T_{AC}) and (b) SmC* phase (17.5 °C below the T_{AC}).

The layer thickness of MSi_3MR11 as a function of the reduced temperature is shown in Figure 4.5. The layer thickness was determined from the Lorentzian fits to the first small-angle peak. The maximum layer shrinkage (LS) is calculated to be 1.7% and the corresponding reduction factor is found as ~0.4, estimated 20 °C below T_{AC}. The measured θ_{indsat} is 26.7° for a field of 10 V/μm. These values suggest that MSi_3MR11 can be considered as a good de Vries smectic.

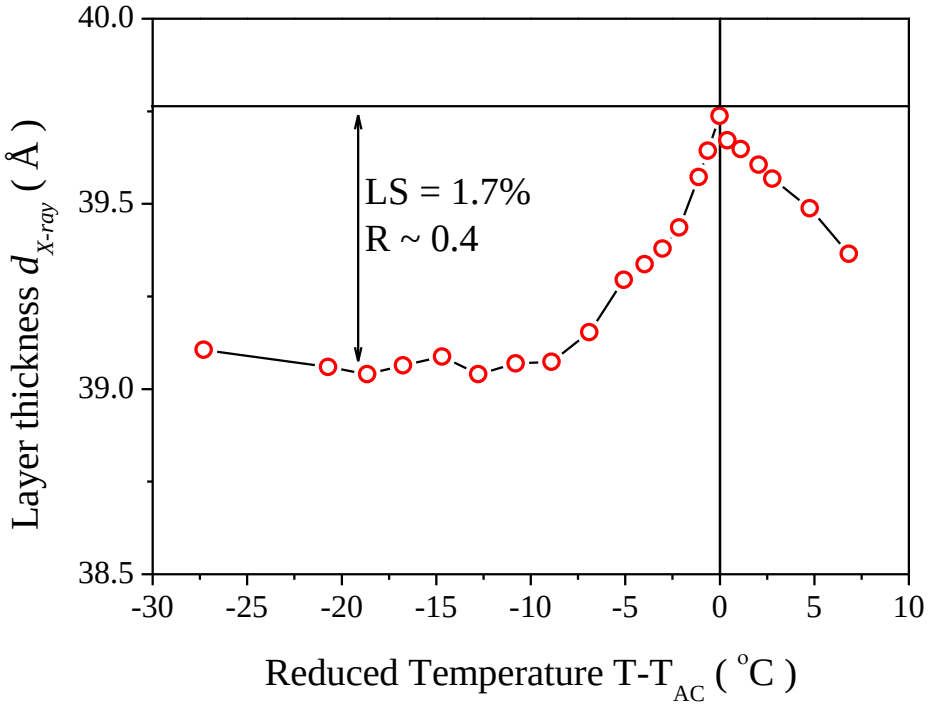

Figure 4.5 Layer thickness as a function of the reduced temperature for MSi_3MR11. LS: Layer shrinkage. R: Reduction factor.

In order to investigate the layer thicknesses change over a narrow range of temperature; we performed high resolution FSF optical thickness measurement. The FSF optical thickness is normalized at the SmA*-SmC* phase transition point and plotted as function of the reduced temperature as shown in Figure 4.6. The plot shows that, on cooling from the isotropic temperature, the thickness increases steadily, as also seen in the X-ray layer thickness data. However, ~2 °C above the T_{AC} the trend reverses and shows a "bump" shaped curve. This implies that the emergence of tilt angle with respect to the layer normal, before the sample reaches SmC* phase. Also the shape of the curve, suggests that the appearance of the tilt angle varies as the temperature gets closer to the phase transition temperature. Such a peculiar trend in FSF optical thickness was previously reported for a series of de Vries type LCs exhibiting antiferroelectric phase in the phase sequence [69].

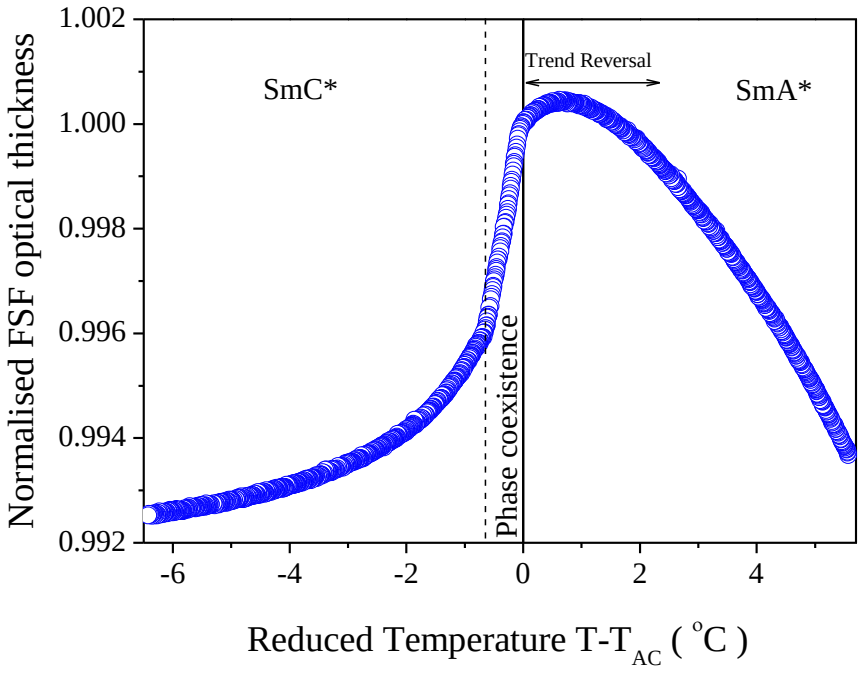

Figure 4.6 Normalized FSF optical thickness data as function of reduced temperature for MSi_3MR11.

The bump shaped thickness trend in the curve of normalised thickness is not clearly seen in the X-ray layer thickness data (Figure 4.5), due to a lower resolution of the experiment. The discontinuity observed in FSF optical thickness is due to phase coexistence region which is denoted by the dotted line in Figure 4.6. The phase coexistence can be observed in FSF under POM, such an image for a de Vries LC is shown in 6th chapter.

4.4 Electro-Optical investigations

The EO measurements were carried out using a 3-μm planar-aligned cell, a triangular wave form electric field with 15 V/μm of frequency 46 Hz was applied. This frequency is chosen to avoid ionic conductivity while providing a sufficient time for a complete switching to occur. Amplitude of the applied field should be large enough to saturate the response but at the same it should be much lower to

avoid the dielectric break down. The EO experiments were performed as explained in the ATP section on experimental methods.

Figure 4.7 shows the measured temperature dependent birefringence for zero electric field. As discussed in the previous chapter, the birefringence decreases instead of increasing on cooling [84]. This shows that MSi_3MR11 is a typical de Vries type LC.

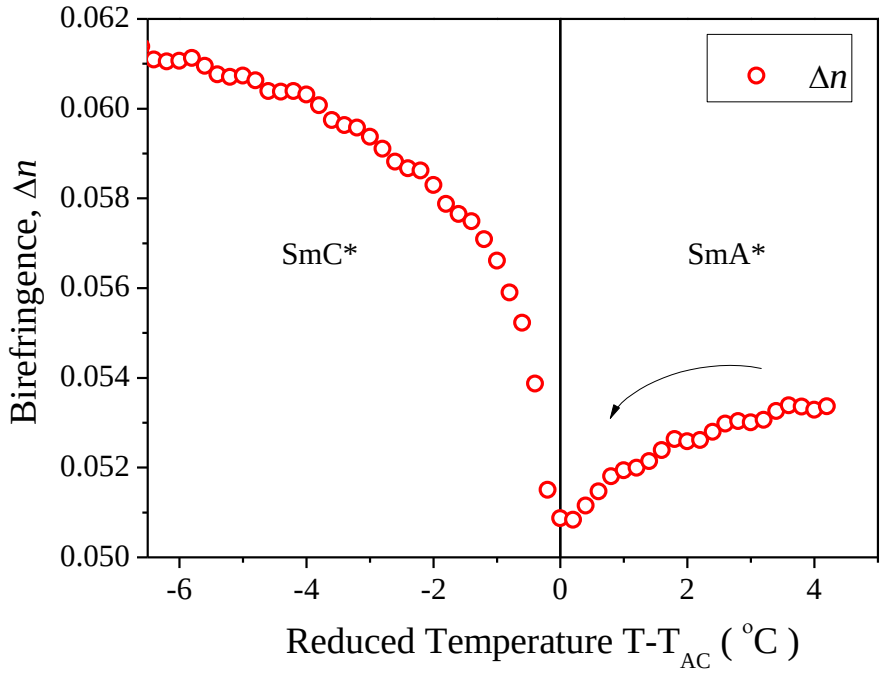

Figure 4.7 Measured birefringence as a function of the reduced temperature with zero electric field using a 3-µm planar-aligned cell. The arrow represents the decreasing tendency of birefringence in SmA* phase.

Figure 4.8 (a) and (b) show the electric field dependence of birefringence (Δn) and optical axis tilt (θ_{ind}) for selected temperatures within SmA* phase.

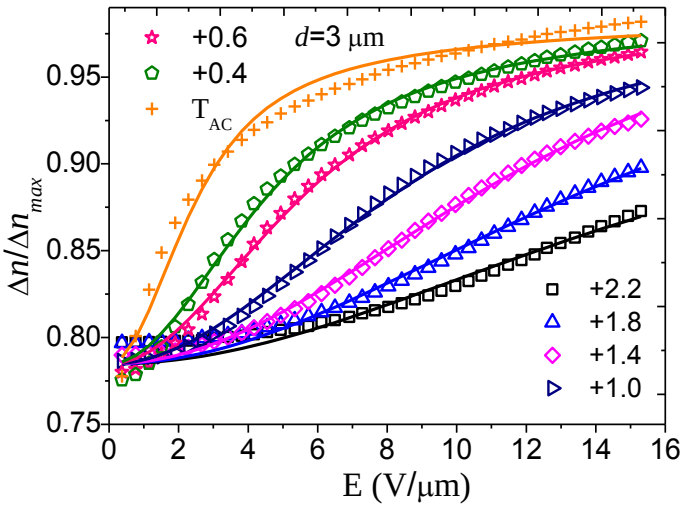

(a)

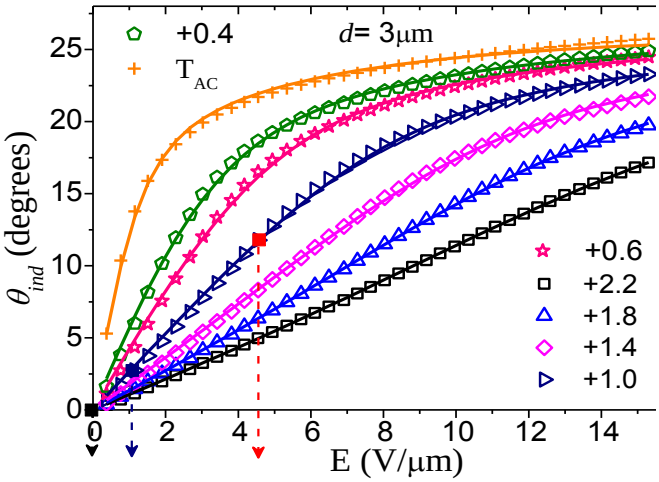

ODF shown in Figure 4.9

(b)

Figure 4.8 (a) The measured birefringence as a function of the applied electric field. (b) Measured apparent tilt angle as a function of applied electric field.Both (a) and (b) shown for selected temperatures in SmA* phase. In Figure 4.7 (b), a few data points are highlighted to represent that a molecular orientational distribution is shown corresponding to these data points in Figure 4.9. Symbols: Experimental data points. Solid line: Theoretical fit by Generalised Langevin-Debye (GLD) model.

A large field induced increase in birefringence is characteristic of de Vries smectic LC (Figure 4.8 (a)) in SmA* phase. In Figures 4.8 (a) and (b), both

birefringence and the apparent tilt angle, show an almost linear increase with field for higher temperatures in the selected range of temperatures (Close to Iso-SmA*). This could be explained by a conventional electro-clinic effect observed in SmA* phase of a FLC [74]. However, on cooling around ~1.5 °C above the T_{AC}, the field dependent response attains a supralinear growth as a function of electric field. Such a curve represents a sigmoidal function. This is yet another observation found in de Vries type smectic LCs. On further cooling, in the vicinity of SmA*-SmC* phase transition the response attains rapid saturation even for low values of electric field. As discussed in Chapter 1 and the introduction, the EO optic response has been modelled by several groups, in order to understand the microscopic origins of the huge electro-clinic effect in SmA* phase of de Vries smectics and to explain the molecular orientational distribution. In this chapter, we employ the most recent model proposed by Shen *et. al.* [42] in 2013. A detailed explanation of the model is given below.

4.4.1 Generalised Langevin-Debye model

The theoretical approach of modelling the EO of de Vries smectics originates from the Langevin-Debye model proposed by Fukuda [41,70,85]. This was originally developed to explain the "thersoldless antiferroelectricity" observed in some chiral tilted SmC* phase [86]. Later in 2002, Clark *et. al.* [87] showed that the Langevin-Debye approach can be successfully employed to describe some key features of the EO response of the de Vries type smectic LCs. This model assumes that the molecules in de Vries SmA* phase are randomly distributed in their azimuthal angle on a cone with a fixed tilt angle (θ_A) with respect to the layer normal. This is considered to as natural molecular distribution where there is no external force

involved (i.e. zero applied electric field). However on applying electric field **E**, the Mean-Field potential of the system varies as:

$$U_p = -pE\cos\phi \tag{4.1}$$

here the local dipole moment **p** couples with the azimuthal angle ϕ. With this description of the Langevin-Debye model Mean-Field potential, Clark *et. al.* qualitatively reproduced the EO response, but could not fit the characteristic sigmoidal shaped EO response as seen in the experimental data. Therefore, in 2013 Shen et. al. [42] modified the original Langevin-Debye model. In his, Generalised Langevin-Debye (GLD) model, in addition to the azimuthal degree of freedom, the molecules are also allowed to vary in tilt angle over a defined range. This dramatically improved the quality of the fit between the theory and experiment. The Mean-Field potential defined in GLD model is expressed as,

$$U = -p_0 E\sin\theta\cos\phi(1+\alpha E\cos\phi) \tag{4.2}$$

where $p_0\sin\theta$ gives the magnitude of the dipole moment of the tilt correlated domain. The first order $\boldsymbol{E}$ term describes the usual energy associated with the dipole interaction. While the second order $\boldsymbol{E^2}$ term with the scaling parameter α provides the tilt susceptibility leading to sigmoidal response as a function of $\boldsymbol{E}$. The mean field molecular orientational distribution function (ODF) is defined as,

$$f(\theta,\phi) = \exp[-U/k_BT]/\int_{\theta_{\min}}^{\theta_{\max}}\int_0^{2\pi}\exp[-U/k_BT]\sin\theta d\theta d\phi \tag{4.3}$$

The average of a physical parameter <*x*> in the GLD model is evaluated as given below,

$$< x >= \int_{\theta_{\min}}^{\theta_{\max}} \int_{0}^{2\pi} x(\theta,\phi) f(\theta,\phi) \sin\theta d\theta d\phi \qquad (4.4)$$

In the GLD model the molecules are allowed to vary in tilt θ over a limited range and this range is estimated from the experiment. Here $\theta_{\max}$ corresponds to the experimentally observed maximum apparent tilt angle with a large applied electric field, sufficient enough to saturate the response in SmA* phase. $\theta_{\min}$ is estimated from the measured zero field birefringence, i.e. the zero field molecular distribution over a cone with an angle of $\theta_{\min}$.

On neglecting the molecular biaxiality and by averaging the dielectric tensor over the ODF Shen *et. al.*[42] derived the expression for the field dependent apparent tilt $\theta_{ind}(E)$ and Δn (E) as,

$$\frac{\Delta n}{\Delta n_{\max}} = \frac{< \cos^2\theta - \sin^2\theta \cos^2\phi >}{\cos 2\theta_{ind}} \qquad (4.5)$$

$$\tan 2\theta_{ind} = \frac{< \sin 2\theta \cos\phi >}{< \cos^2\theta - \sin^2\theta \cos^2\phi >} \qquad (4.6)$$

here Δn_{max} is the saturated maximum value of birefringence for a large applied electric field.

Equations (4.5) and (4.6) are used to fit the experimental data given in Figure 4.8 (a) and (b) respectively. For MSi_3MR11 we have found that θ_{min} = 16.9° and θ_{max} = 26.6°. The molecular tilt is allowed vary within the above given limits and two other fitting parameters (p_0 and α) are used to obtain the fit. Values of θ_{min} and θ_{max} are kept fixed for different temperatures, however the other parameters strongly depends on temperature. In this work, in contrast to the procedure followed by Shen *et. al.* , [42] the fitting was carried out separately for both $\theta_{ind}(E)$ and Δn (E), in order

to improve the quality of the fit. This change in procedure produced higher quality fit, but the obtained temperature dependent fitting parameter follow different trends for temperatures close to $T_{AC.}$ This is evident from Figure 4.9. The local dipole moment p_0 varies like a power law function and diverges at T_{AC}. The power law exponents obtained for the two curves are different and this is one of the shortcomings of the GLD model. Nevertheless both the estimated exponents (γ=1.80 for the apparent tilt angle and γ=1.67 for birefringence) fall in the expected range as discussed in the previous chapter.

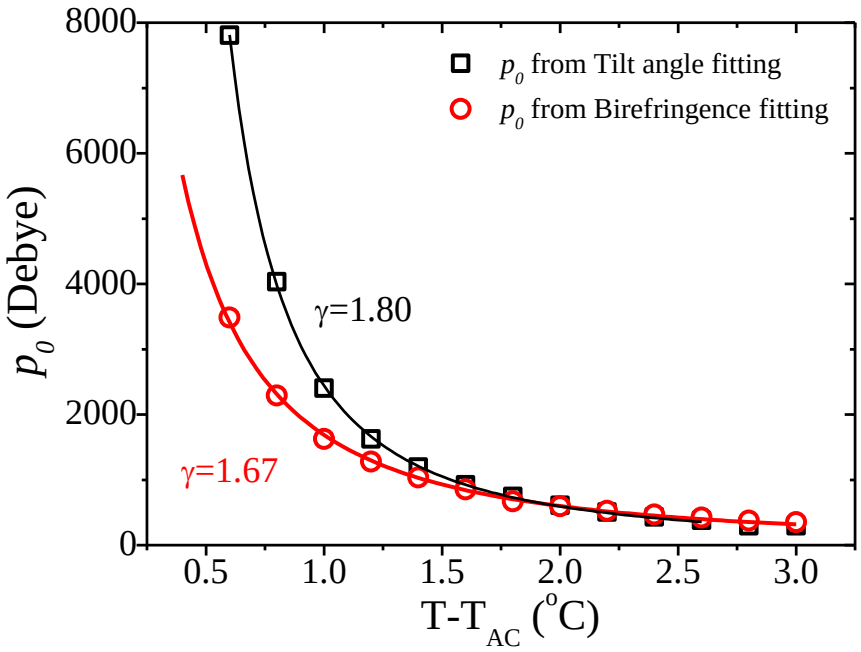

Figure 4.9 Temperature dependence of the fitting parameters p_0. Symbols: Estimated fitting parameter Line: Power law fit.

As shown in Figure 4.9, on cooling the local dipole moment p_0 gradually increases, this is due to the increase in size of the tilt correlated domain. The scaling parameter α varies from ~0.017 to 0.023 μm/V for birefringence and ~0.024 to 0.11 for the apparent tilt angle. Nevertheless, this clearly indicates the system under consideration is much more complex than the model with simple assumptions despite

the quality of the fit obtained. One of the reasons for the observed shortcomings of the GLD model could be that, the model works with fixed values of θ_{min} and θ_{max} (i.e. independent of temperature). However the thickness measurements and the zero field temperature dependent birefringence experimental data strongly suggest that, the diffuse cone (θ_{min}) angle should be a function of temperature. This limitation is addressed in the following chapters.

Figure 4.10 shows the molecular orientational distribution function (ODF) for a single temperature T= (T_{AC} + 0.8 °C) and for different applied electric field. For zero applied electric field the model assumes that, the molecules are distributed uniformly over a cone formed between θ_{min} and θ_{max}, shown by black coloured lines in Figure 4.10 (a). An electric field is applied along the layer plane (along Y-axis in the Figure 4.10). For low values of applied electric fields the molecules are tilted to one side depending on the sign of the applied field, this is shown by blue coloured line Figure 4.10 (b). However, for high values of the applied electric field, almost all molecules crowd over a narrow range of azimuthal angles shown by red coloured lines in Figure 4.10 (c). The apparent tilt angle is an average of the tilted molecules as shown in Figure 4.10.

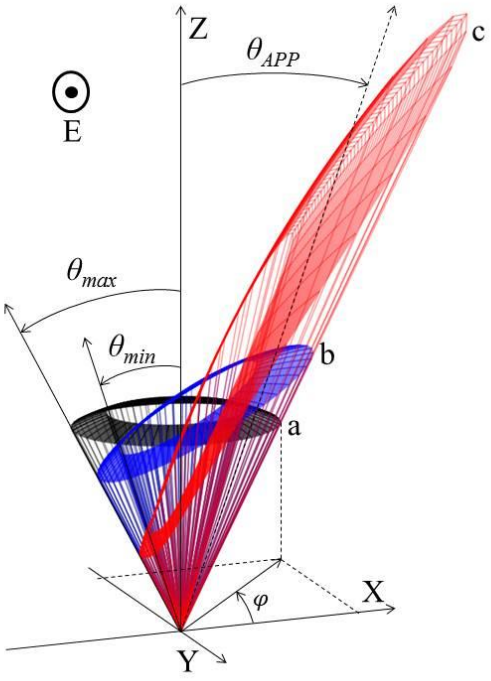

Figure 4.10 The ODF of MSi_3MR11 at a temperature of $T = T_{AC} + 0.8^oC$ for selected values of applied electric field – (a) 0 V/µm (black); (b) 1 V/µm (blue); and (c) 4 V/µm (red). *X*-*Y* is the smectic layer plane and *Z* axis is along the layer normal. The field is applied along *Y*-direction (along smectic layer plane).

4.5 Spontaneous polarisation measurement

Figure 4.11 shows a plot of the spontaneous polarisation measured as function of the reduced temperature. Measurements were carried out using a 4 µm planarly aligned cell with an ITO area of 20 mm^2. A trigular wave AC electric field of 12.5 V/µm is applied across the cell with at a frequency of 152 Hz. The $\boldsymbol{P_s}$ is measured as explained in the experimental section. A large electric field is applied to ensure the saturation of the induced polarisation in SmC* phase. MSi_3MR11 exhibits a maximum value of Ps~124 nC/cm^2 at 13.5 °C below T_{AC}.

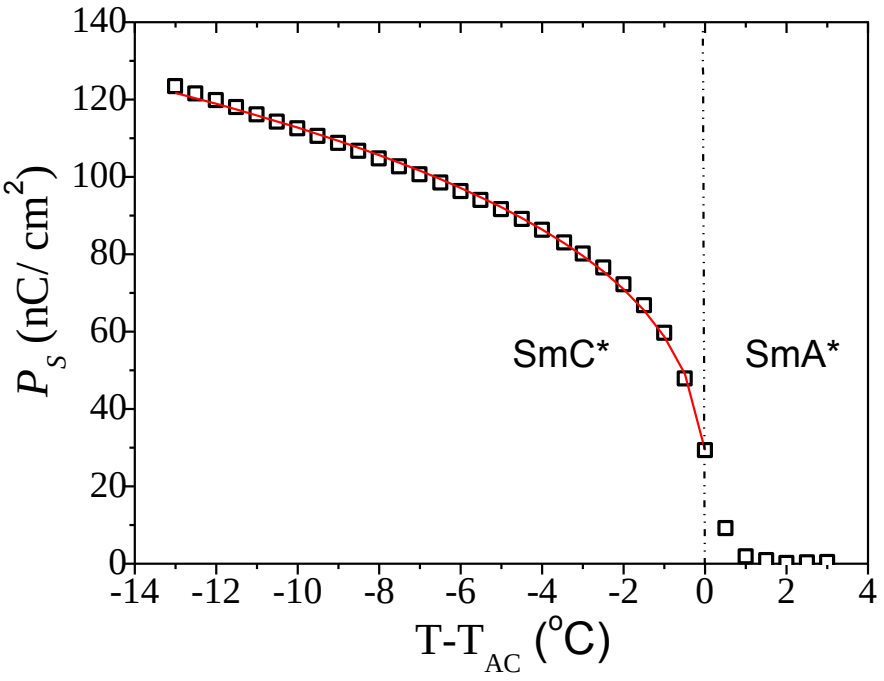

Figure 4.11 Spontaneous polarization P_s *vs* (T-T$_{AC}$) measured using a 4 µm planar cell under cooling from the isotropic state. Triangular-waveform voltage of 50 V$_{pk\ to\ pk}$ at a frequency of 152 Hz is used in the experiment.

Temperature dependent experimental values of P_s shows power law dependence in SmC* phase, similar to the order parameter critical exponent as discussed in the previous chapter. Therefore below the T$_{AC}$, P_s can be expressed as,

$$P_S = P_0(T_{AC}^{\ *} - T)^{\beta} \qquad (4.7)$$

here β is the critical exponent. The estimated exponent for the best fit is found to be β=0.29. As expected this value is lower than the exponent for the conventional smectics β=0.35. This suggests that the MSi$_3$MR11 belong to de Vries type LC and it exhibits a 'weakly first order phase transition' [63].

Section 2

4.6 Infrared measurements on de Vries smectics

In this section we have used polarised Infrared (IR) spectroscopy to investigate two de Vries materials: MSi_3MR11 and W599 [88].

The polarized IR technique offers a direct measurement of the dichoric ratio and the orientational order parameter of the LC system based on the intensity of molecular vibrations when exposed to IR radiations [89]. The measurements can be obtained as a function of temperature, electric field or both [90]. The experimental method involved in this investigation is described below.

The polarized IR measurements were performed using Bio-Rad FTS-6000 spectrometer with spectral range of 450 to 4000 cm^{-1} in wave number. The spectrometer is equipped with a liquid nitrogen cooled mercury cadmium telluride (MCT) detector. The wire grid rotation polarizer is controlled by a computer. The sample is mounted on to a hot stage with a temperature stability of ±0.1 °C. Zinc selenide (ZnSe) plates are used for the LC sample cell instead of the usual glass plates, since ZnSe is transparent over the IR region. The ZnSe windows are coated with a thin layer of ITO. The windows are also coated with a polymer solution (RN1175) and kept in an oven at 250 °C, in order to obtain a homogenous planar alignment. These windows are then sandwiched with a 5 μm Mylar spacer to provide the necessary gap.

The IR spectra are recorded for selected temperatures in SmA* and SmC*, while more data points are obtained in SmA* phase which is our current interest. DC biases of both positive and negative voltages are applied across the cell. The polarizer is rotated from 0° to 180° with 10° steps for each applied voltages and the IR spectra is recorded for every positions. The intensity and the width of the each

measured spectral lines are obtained using Perkin-Elmer GRAMS Research (PEGR) program. Origin 7.5 software is used to fit each absorbance profile.

In this section we have investigated one of the materials that were studied by the Shen et. al. known as W599. It was again resynthesized by Queen Unversity, Belfast group for this work. The molecular structure and the phase transitions of W599 are shown in Figure 4.12.

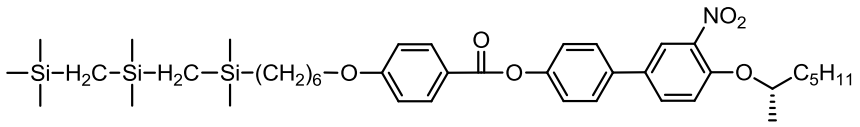

SmC* 29 °C SmA*43 °C Iso

Figure 4.12 Molecular structure and phase sequence of W599.

The W599 molecular structure is a tricarbosilane end tail analogue of the well-known de Vries type smectic material TSiKN65 [31] which is of organosiloxane end chian. The compound with a carbosilane end tail is found to be more stable than the organosiloxane end tail one. Results from Shen *et. al.* [42] work shows that W599 is also a very good candidate for de Vries type smectic LC.

The experimental spectra of MSi_3MR11 and W599 show multiple absorption bands corresponding to the vibrations of several molecular groups of the constituent molecule, respectively. From these spectra, the C-C phenyl ring stretching vibration is chosen, since it is the most prominent peak and easily separable from the other peaks. It is positioned at 1608 cm^{-1} for MSi_3MR11 and 1605 cm^{-1} for W599. Moreover, the dipole moment of these vibrations is parallel to the long axis of the molecule in each of these compounds. The absorbance profile *A* as a function of the

molecular tilt θ for this C-C band varies with polariser rotation and also by the applied electric field. A unique absorbance profile is constructed for each applied voltage and is fitted to the given equation [91,92]:

$$A(\theta_P) = -\log_{10}[10^{-A_{\parallel}} + (10^{-A_{\perp}} - 10^{-A_{\parallel}})\sin^2(\theta_P - \theta_{indIR})] \qquad (4.8)$$

where θ_P is the polariser angle, minimum and maximum values of the absorbance at different polariser angles are given by $A_{\perp}$ and $A_{\parallel}$ and the θ_{indIR} is represented as the induced apparent tilt angle by the applied field, for which the absorbance of the phenyl stretching is maximum for the given polariser angle.

The estimated θ_{indIR} values of MSi_3MR11 and W599 as a function of the applied voltage acrosse the cell for selected temperatures in SmA* phase is shown in Figure 4.13 (a) and (b) respectively.

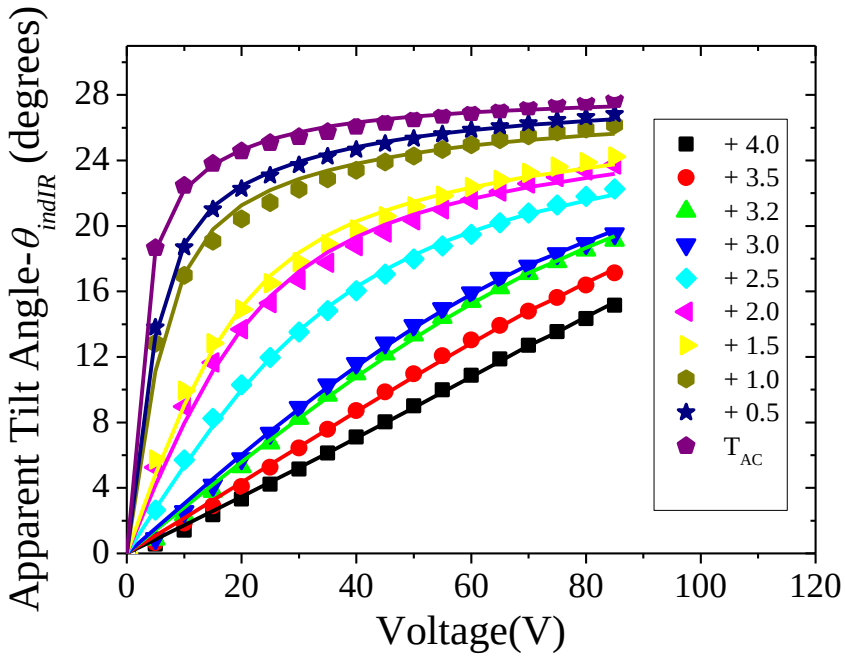

(a)

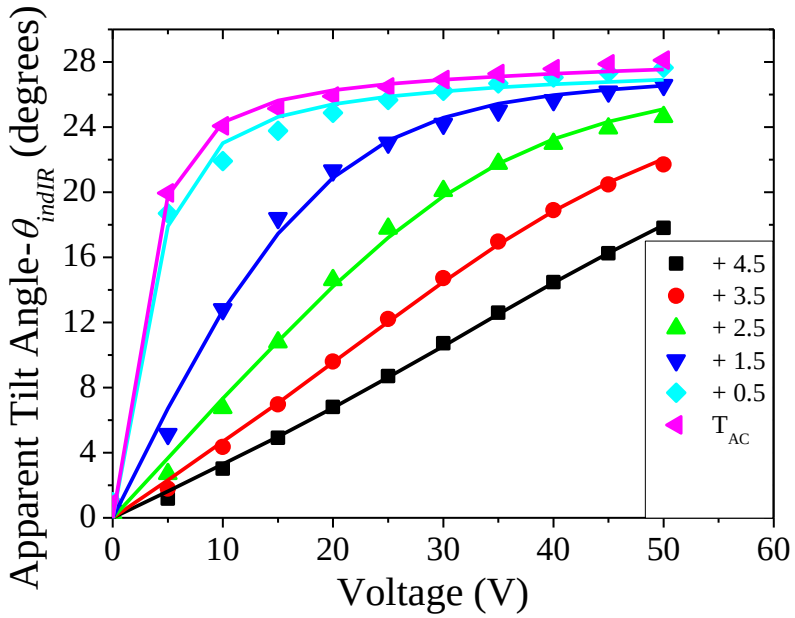

(b)

Figure 4.13 Field dependent apparent tilt angle θ_{indIR} determined from the absorbance profiles of the C-C phenyl ring stretching vibration at various temperatures in SmA* for (a) MSi_3MR11 at 1608 $cm^{-1}$and (b) W599 at 1605 cm^{-1}. Symbols: Experimental values. Solid line: Fit to Equation 4.6 the GLD model.

The apparent tilt angle θ_{indIR} estimated from the IR measurements is analogous to the optical axis tilt in the EO measurements. Therefore we employed the GLD model to fit the θ_{indIR} as a function of applied electric field using Equation 4.6. The initial parameter for the fit, i.e θ_{min} is obtained from the zero field birefringence value, θ_{min} = 16.9° for MSi_3MR11 and θ_{min} = 25.6° from Ref [42] for W599. However, θ_{max} is estimated from the above given experimental values θ_{max} = 28.4° for MSi_3MR11 and θ_{max} = 28.6° for W599. The model yields a good fit for the apparent tilt angle θ_{indIR} estimated from the IR measurements.

The fitting parameter p_0 diverges as SmA*-SmC* phase transition is approached shown in Figure 4.9 for MSi_3MR11 and Figure 4 (d) in [42]. The magnitude of p_0 given in the Ref [42] and here matches for high temperatures, but

attains the values of the order 10^3 for temperatures close to T_{AC} for W599. The temperature dependence of the fitting parameter p_0 is shown in Figures 4.14 (a) and (b) for MSi_3MR11 and W599.

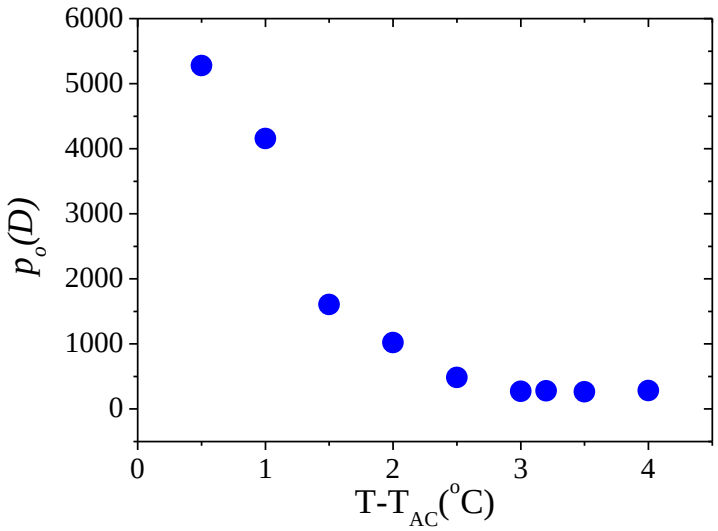

(a)

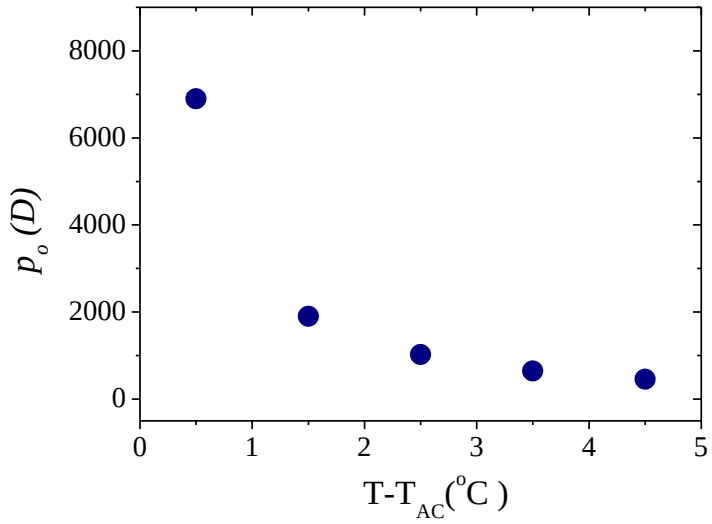

(b)

Figure 4.14 The local dipole moment p_0 as function of the reduced temperature from GLD model for (a) MSi_3MR11 and (b) W599

4.7 Conclusions

The heptamethyltrisiloxane based LC - MSi3MR11 is known to be a good de Vries smectic LC. This material was studied using a number of techniques such as, DSC, POM, X-rays, EO and Spontaneous Polarisation. From DSC and POM studies we show that the material shows direct transition to SmA* phase from Isotropic phase. The low value of the enthalpy suggests that the material exhibits weakly first order SmA*-SmC* phase transition. From X-ray layer thickness measurements we show that the MSi3MR11 exhibits a maximum layer shrinkage of 1.7% and a corresponding reduction factor is 0.4. MSi_3MR11 exhibits a maximum value of $\boldsymbol{P_s}$ ~124 nC/cm^2 at 13.5 °C below T_{AC}. The high resolution FSF optical thickness measurement shows a characteristic trend reversal within the SmA* phase. Moreover, an anomalous observed decrease in the measured birefringence is seen in the temperature dependent birefringence data. We show that the field dependent EO for MSi3MR11 shows a characteristic sigmoidal shaped response near T_{AC}. We employed the GLD model proposed by Shen *et. al.* to fit the field dependent birefringence and the apparent tilt angle. From fitting we show that the tilt correlated domain grows in size and follows a power law function with temperature with a critical exponent much greater than for the conventional smectics. We show that the GLD model produces a good fit to the observed experimental data. However, we have highlighted a few shortcomings and given an account of the limitations in the GLD model. These will be addressed in the following chapters. Later on we performed a detailed IR spectroscopy studies for MSi3MR11 and W599. W599 is yet another well-known de Vries smectic material, which is a carbosilane analogue of the well studied TSiKN65. The obtained field dependent apparent tilt angle from the IR measurements is also modelled with the GLD model. The model surprisingly works

quite well for the IR apparent tilt angle vs temperature and produces a similar result as we get from the EO measurements. Overall the two well-known de Vries smectic materials are extensively studied using a number of experimental techniques and also the field dependent EO is modelled to understand the role of the diffuse cone model in explaining the nature of the de Vries smectics.

‘

Chapter 5

5. Novel Chiral de Vries Smectics

5.1 Introduction

In the previous chapters the high resolution birefringence and the thickness measurements showed trend reversal prior to the SmA*-SmC* phase transition. These results can be interpreted in terms of the two outcomes, (i) The molecules are tilted in SmA* phase as de Vries predicted, (ii) the molecular tilt angle with respect to the layer normal varies as a function of temperature in SmA* phase.

In this chapter we mainly focus on to obtaining further evidence on the above discussed scenario. We investigate novel chemical compounds for a better understanding of the molecular structure of de Vries smectic LCs.

This chapter is divided into two sections; in the first section we modify the GLD model by introducing a new fitting parameter. The experimental results in the first section are from a new carbosilane end tail de Vries smectic LC.

In the second section of this chapter, we study a new low layer shrinkage material, with epoxyhexoxy backbone. We also propose a new theoretical model for the EO response. We also compare the results obtained from the fitting of the experimental results from the EO experiment to different models.

Section 1

5.2 Material under investigation

The molecular structure and the phase transition temperatures for DR276 are given in Figure 5.1. DR276 is based on 5-phenyl-pyrimidine benzoate core terminated with a tri-carbosilane group on one side and chiral 2-octanol on the opposite side.

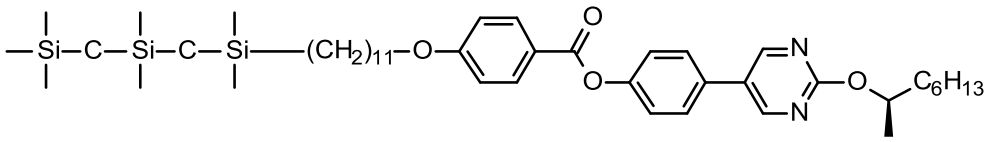

Cryst 14°C SmC* 78.5°C SmA* 87°C Iso

Figure 5.1 Molecular structure and the phase transition temperatures of DR276.

Sreenilayam *et. al.* recently reported the synthetic procedure of DR276, X-ray layer thickness and EO experimental results [93]. DR276 shows maximum layer shrinkage of ~1.9% at 10 °C below T_{AC} and the reduction factor **R** of DR276 is ~0.3. These results suggest that DR276 is a good candidate for de Vries type smectics.

5.3 Electro-Optic Measurements

The EO measurements are carried out using a planar-aligned cell of thickness 2.6 μm filled with DR276. A triangular wave electric field of magnitude 14 $V_{0\text{-}pk}/\mu m$ is applied across the cell. The birefringence and the apparent tilt angle values were obtained as explained in the ATP section, in Chapter 2.

Figure 5.2 shows the temperature dependent birefringence for zero and maximum applied electric field. DR276 also shows a characteristic decrease of the birefringence in SmA* phase as discussed in the previous chapters with a reduction in temperature. *Δn* for maximum applied field is plotted along with the zero field *Δn*. For high temperatures in SmA* phase (close to Iso) the applied field increases *Δn* slightly. However on cooling we can see a significant difference between the zero field Δn and the maximum field Δn. This is again a typical characteristic of the de Vries SmA* phase. The applied electric field (14 V/μm) increases the birefringence by 32% at the phase transition temperature T_{AC}. This behaviour strongly implies that the molecular tilt emerges within the temperature range of SmA* slowly and then increases rapidly on approaching the SmA*-SmC* phase transition.

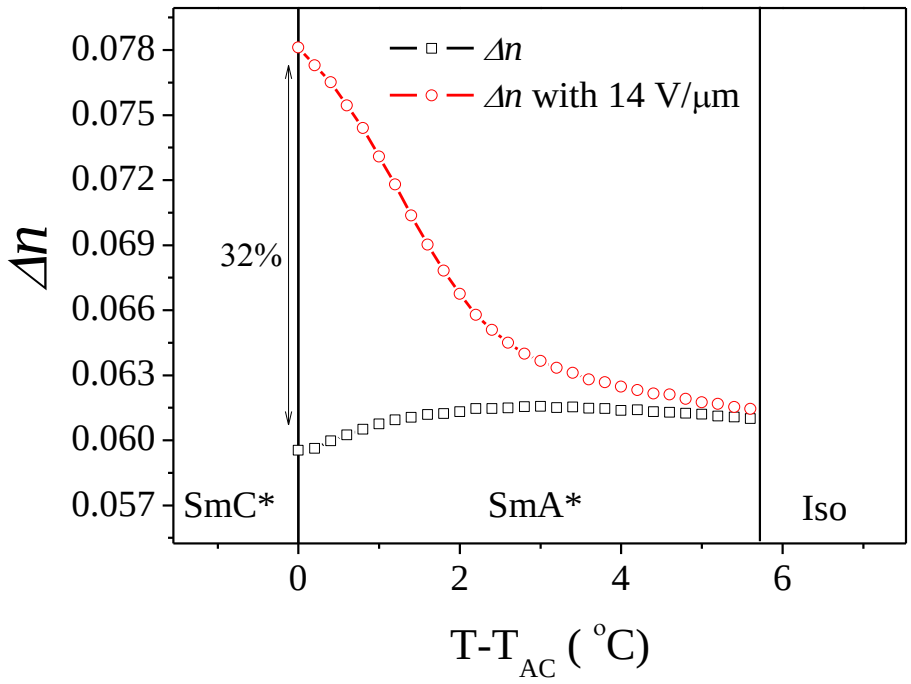

Figure 5.2 Plot of the temperature dependent birefringence Δn with (14 V/μm) and without applied electric field in SmA* phase of DR276.

5.4 Modified-GLD model

In the original model (GLD) the molecular tilt with respect to the layer normal is assumed to vary over prescribed limits from θ_{min} to θ_{max}. θ_{min} is estimated from the zero-field birefringence value and θ_{max} refers to the saturated value of the measured apparent tilt angle for the maximum applied electric field under the assumption that the birefringence with this field is saturated. For DR276 we found that the saturated apparent tilt angle is 31^o, *i.e.* $\theta_{max} = 31^o$.

However, based on the investigations of the temperature dependent layer thickness and birefringence, we strongly anticipate that θ should also be a function of temperature. Therefore we modify the GLD model by releasing the lower integration limit θ_{min} (in Equations 4.3 and 4.4). The θ_{min} is replaced by θ_T which will now be a new fitting parameter, along with p_0 and α remaining as the other two fitting parameters associated with the Mean-Field potential. The new ODF is shown below,

$$f(\theta,\phi) = \exp[-U/k_BT] / \int_{\theta_T}^{\theta_{\max}} \int_0^{2\pi} \exp[-U/k_BT] \sin\theta d\theta d\phi \quad (5.1)$$

The average of a physical parameter 'x' in modified GLD model is evaluated as given below,

$$< x >= \int_{\theta_T}^{\theta_{\max}} \int_0^{2\pi} x(\theta,\phi) f(\theta,\phi) \sin\theta d\theta d\phi \quad (5.2)$$

Figure 5.3 (a) and (b) show the electric field dependent Δn and θ_{ind} respectively, for several temperatures in SmA* phase. The data (symbols) are fitted to the model (solid lines) using Equations (4.5) and (4.6), respectively. We see that both Δn and θ_{ind} vary linearly with E for a temperature range close to Iso-SmA* transition in Sm*A** phase. While, on cooling the response tends to saturate and also

exhibit a sigmoidal-shaped curves; clearly visible for $T-T_{AC} \leq 2°C$. The modified GLD model reproduces the characteristic electro-optic response quite well which is evident from the quality of the fit.

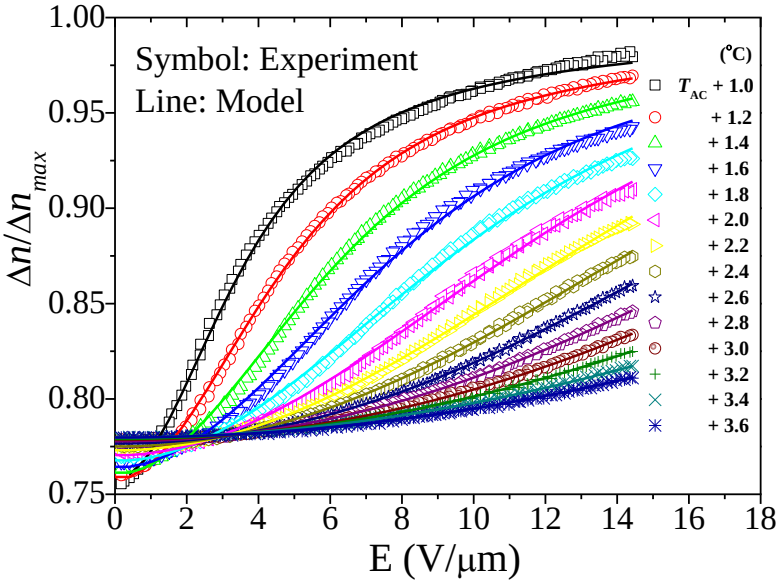

(a)

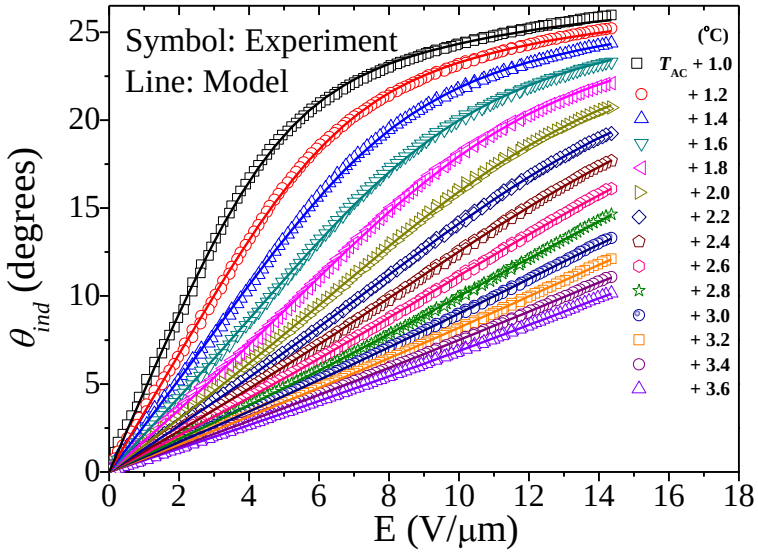

(b)

Figure 5.3 (a) Birefringence Δn and (b) the apparent tilt angle θ_{ind} as a function of applied electric field for a range of temperatures in SmA* phase. Symbols – experimental data, Solid line – Modified GLD model fit.

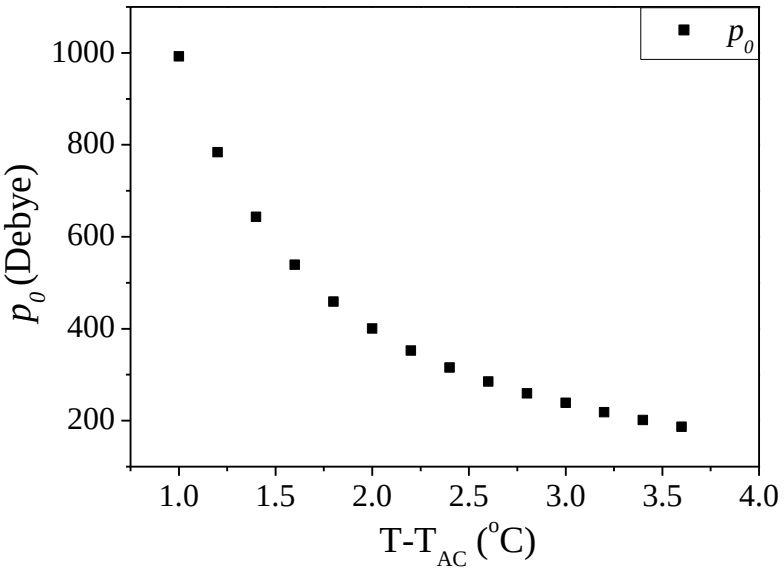
p_0
1000
800
600
400
200
p_0 (Debye)
1.0
1.5
2.0
2.5
3.0
3.5
4.0
T-T$_{AC}$ (^{o}C)

(a)

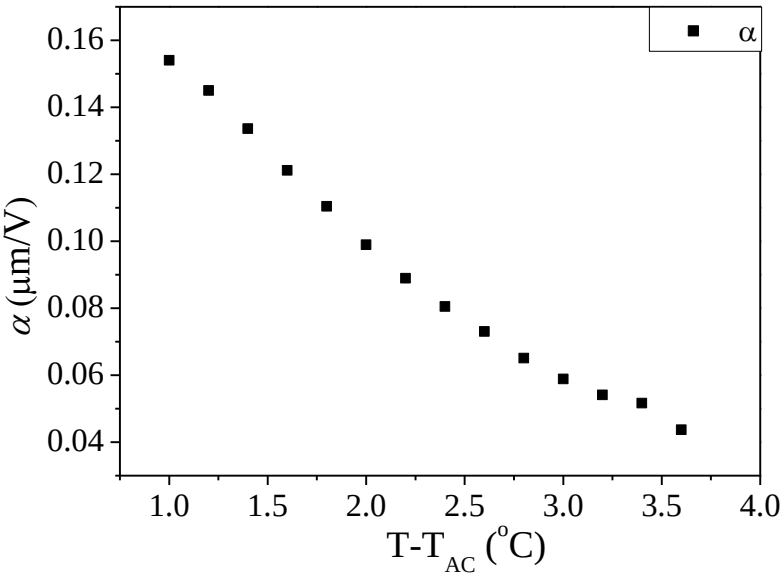
α
0.16
0.14
0.12
0.10
0.08
0.06
0.04
α (μm/V)
1.0
1.5
2.0
2.5
3.0
3.5
4.0
T-T$_{AC}$ (^{o}C)

(b)

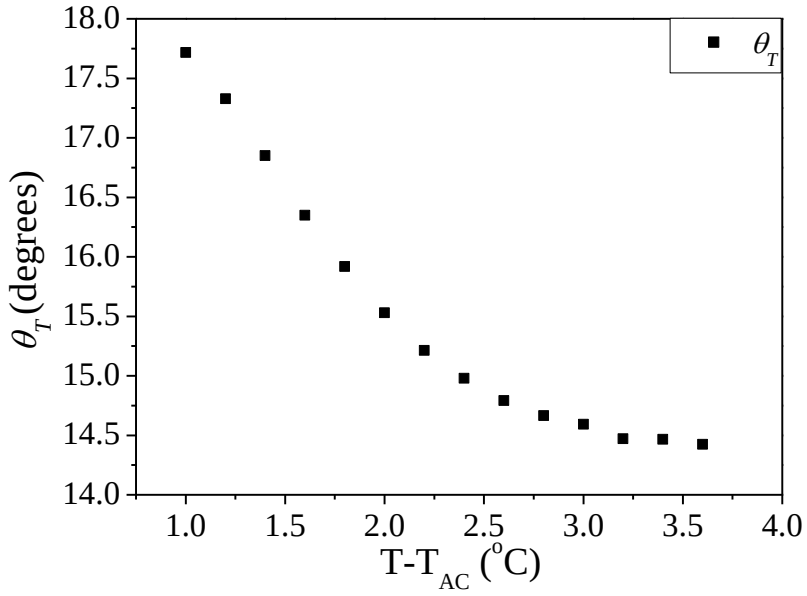

(c)

Figure 5.4 The temperature dependence of fitting parameters a) local dipole moment p_0 b) phenomenological parameter α and c) diffuse cone tilt angle θ_T of modified GLD model.

The temperature dependent variation of the fitting parameters $p_{0,}$ α and θ_T are shown in Figure 5.4. The magnitude of p_0 diverges on approaching Sm*A**-Sm*C** phase transition which corresponds to the growth in the size of the tilt-correlated domains. The phenomenological parameter α increases almost linearly on cooling towards Sm*A**-Sm*C** phase transition. For the given range of temperatures in SmA* phase θ_T varies from 14° to 18° and it clearly increases on cooling as expected from our earlier discussions.

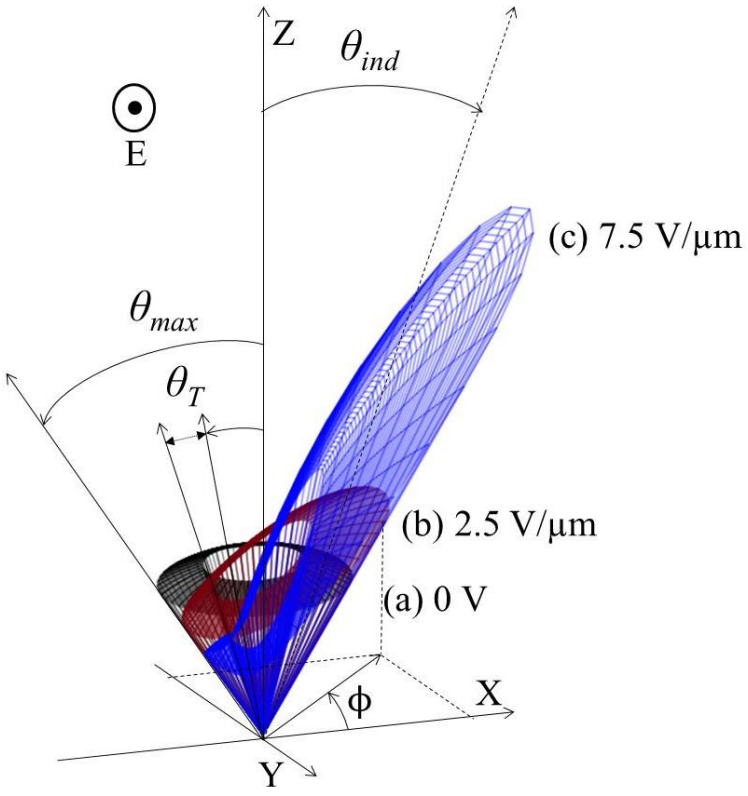

Figure 5.5 Orientatinal distribution function *f (θ,ϕ)* from the modified GLD model for DR276 at (T_{AC} + 1.6) °C for selected applied voltages (a) 0 V/µm, (b) 2.5 V/µm and (c) 7.5 V/µm. (shown in polar co-ordinates)

Figure 5.5 shows the ODF *f (θ,ϕ)* obtained using the modified GLD model at (T_{AC} + 1.6) °C for different applied fields. For zero electric field, the ODF shows that molecules are distributed uniformly over a diffuse cone with θ varying from θ_T to θ_{max}. On applying the electric field, the cone gets distorted as a result of the molecules crowding towards one side of the cone. For higher electric fields the distribution gets condensed, confining the molecules over a narrow range of azimuthal angles. This is also evident from the saturation of θ_{ind} observed in the experiment. The temperature dependent variation of θ_T is represented by the double headed arrow in Figure 5.5.

Section 2

5.5 Material under investigation

The molecular structure and the phase transition temperatures for adpc042 are given in Figure 5.6. The adpc042 LC is based on 5-phenyl-pyrimidine core functionalized with a tri-siloxane group on one side and (*R, R*)-2,3-epoxyhexoxy chain on the opposite side [94].

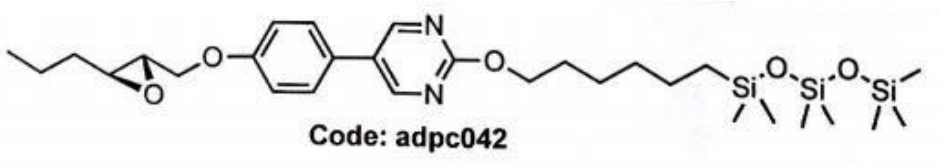

Cr -5 ^{o}C Sm*C** 58 ^{o}C Sm*A** 82 ^{o}C Iso

Figure 5.6 Molecular structure and the phase sequence of adpc042 LC.

The DSC thermogram of adpc042 is shown in Figure 5.7. The DSC data are obtained on cooling at a rate of 10 °C/min. The DSC thermogram shows a huge peak at ~82 °C with an enthalpy Δ*H* of ~11.71 Jg^{-1} corresponding to the Iso-SmA* phase transition. The SmA* phase is also confirmed by the POM image captured using a 9-μm planar-aligned cell and a focal conic texture observed in SmA* temperature range. On cooling the sample, the second peak appears at ~58 °C with Δ*H* of ~0.49 Jg^{-1} suggesting that a weakly first order SmA*-SmC* phase transition occurs. The POM image captured in SmC* phase shows a broken fan shaped texture, typical for a tilted phase of calamatic LC molecules. The POM textures are shown in the inset of Figure 5.6.

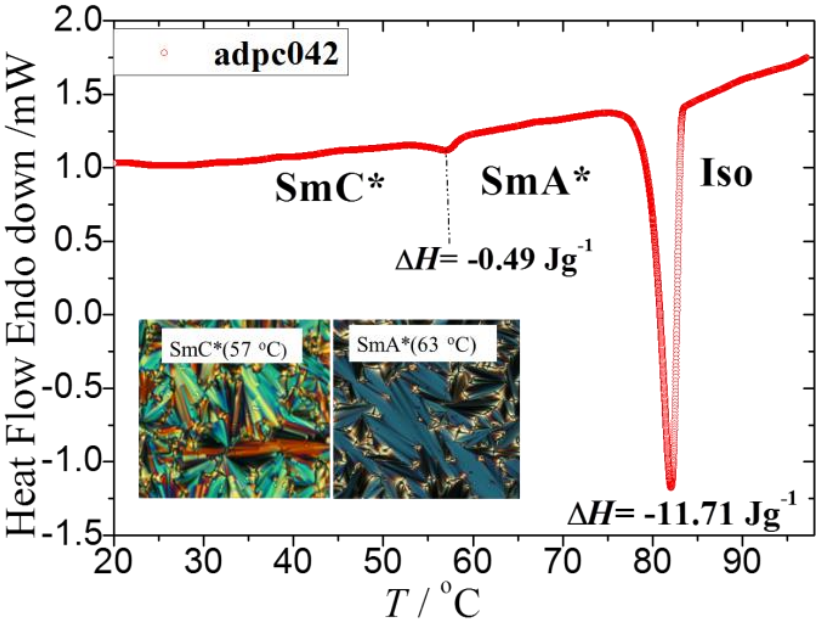

Figure 5.7 DSC thermogram of adpc042 recorded on cooling at a rate of 10 °C/min. Insets are images captured from POM under crossed polarisers using a 9-µm planar-aligned cell.

5.6 Layer thickness measurements

The temperature dependent layer thickness is obtained by X-ray diffraction method. Measurements were carried out using Bruker D8 diffractometer using Cu-K_α source at a wavelength of 0.154 nm. The layer thicknesses were obtained as described in the experimental section. X-rays measurements were carried out under cooling with a ramp rate of 0.1 °C, shown in Figure 5.8. We have also conducted FSF optical thickness measurements for adpc042 using high resolution method as described in the experimental section [95]. The FSF measurement was carried out on cooling with a ramp rate of 0.02 °C. Figure 5.7 shows the temperature dependent layer thickness and the optical thickness of adpc042. The FSF optical thickness is normalised by the layer thickness at T_{AC}. The X-rays layer thickness shown below is obtained in a much higher resolution compared to the previous data discussed in earlier chapters. As a result, the characteristic trend reversal of the thickness in SmA* phase is being observed.

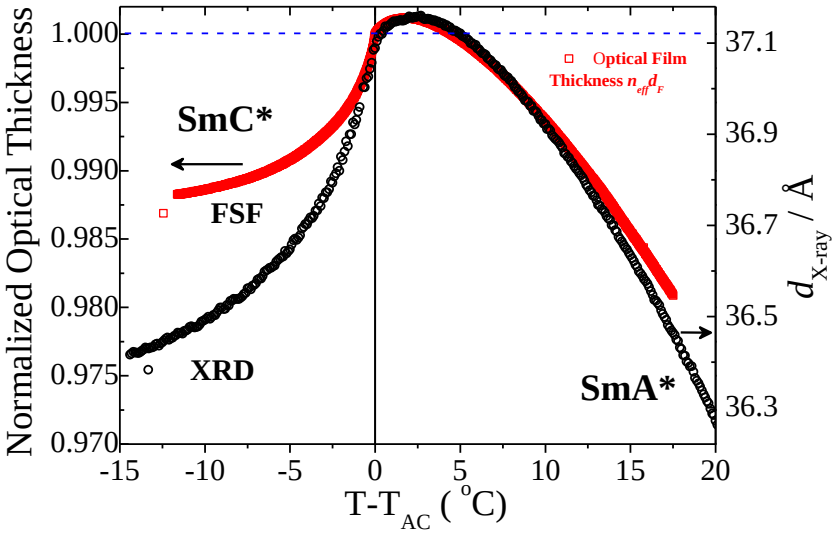

Figure 5.8 A comparison of the smectic layer thickness from X-ray and normalised FSF optical thickness as a function of the reduced temperature.

Figure 5.9 shows simulated molecular structure in its extended form. The simulation was performed using Hyperchem Program. The molecular length *l* is estimated from simulation as ~31 Å, lower than the layer thickness obtained from X-ray diffraction. A possible pseudo bilayer structure is shown in Figure 5.8 such that the total length of the pair of molecules matches the obtained layer thickness.

The layer shrinkage of adpc042 is estimated as ~1.7% for 13 °C below T_{AC} and the corresponding reduction factor **R** is 0.4 for an apparent tilt angle of 28° for the given temperature. These values suggest that adpc042 is a reasonable candidate for de Vries smectic.

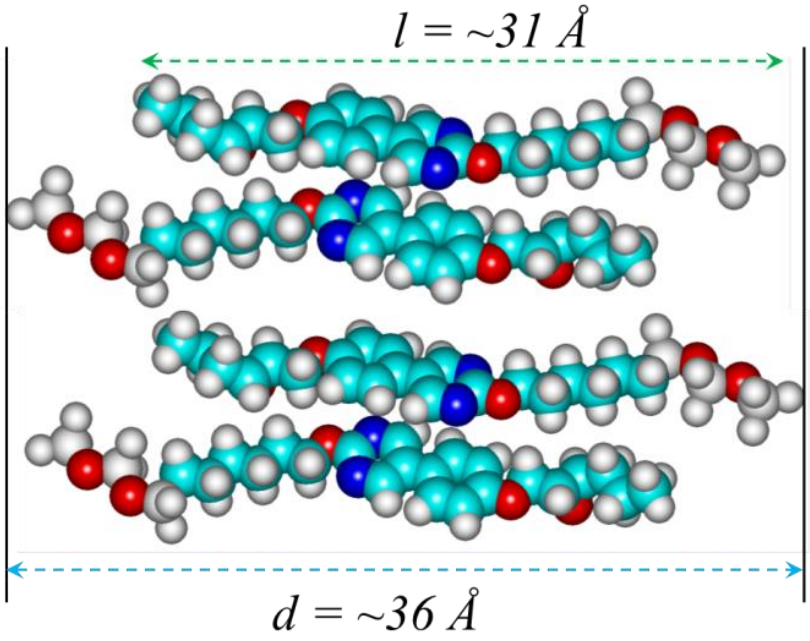

Figure 5.9 Simulated molecular structure using Hyperchem Program and a presentation of the proposed pseudo bilayer structure.

5.7 Spontaneous polarisation measurement

The measured values of spontaneous polarization $\boldsymbol{P_S}$ as a function of the reduced temperature are shown in Figure 5.10. Measurements were carried out using a 5-µm planar-aligned cell under the application of a square wave AC voltage of frequency 110 Hz with an amplitude of 12 V/µm. The square wave method of obtaining $\boldsymbol{P_S}$ is explained in Chapter 2. The applied electric field is large enough to unwind the helical structure in SmC* phase to obtain the saturated $\boldsymbol{P_S}$. $\boldsymbol{P_S}$ increases with a decrease in temperature below the SmC*-SmA* transition temperature. The adpc042 LC yields a maximum of $\boldsymbol{P_S} \sim 82.5$ nC cm^{-2} for $T = (T_{AC} - 30)$ ^{o}C.

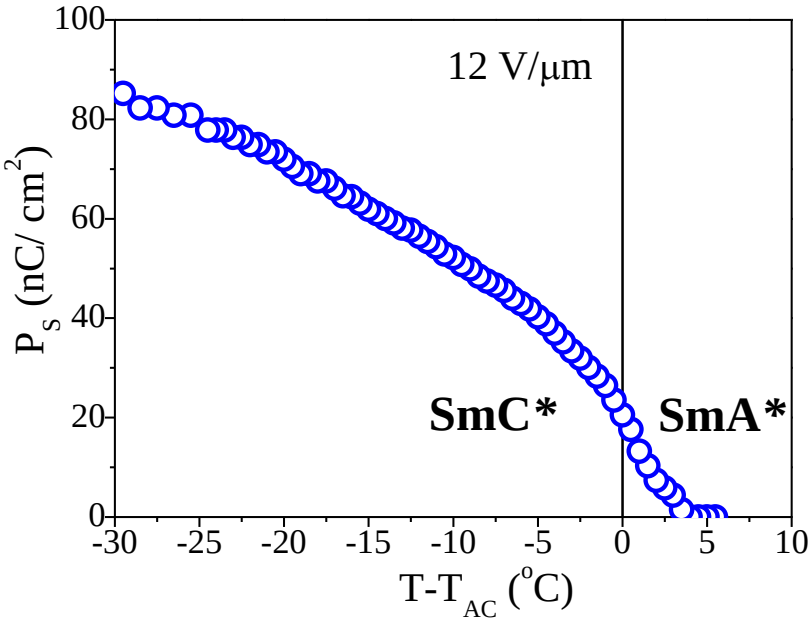

Figure 5.10 Spontaneous polarisation P_S as a function of the reduced temperature for adpc042.

5.8 Electro-Optic measurements

The POM images of a planar-aligned textures of SmA* phase are shown in Figure 5.11 in order to represent the field induced increase in birefringence. The applied electric field changes the observed interference colours; a characteristic of de Vries smectic LC.

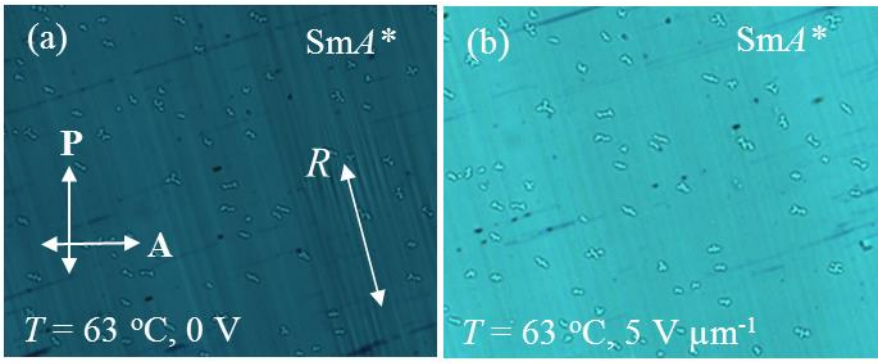

Figure 5.11 POM images of a planar aligned SmA* phase texture obtained at 63 °C in 9-μm planar-aligned cell filled with adpc042. (a) without electric field (b) with a field of 5 V/μm. The crossed polariser state is represented by P-polariser and A-analyser oriented at right angles to each other. The double headed arrow represents the rubbing direction.

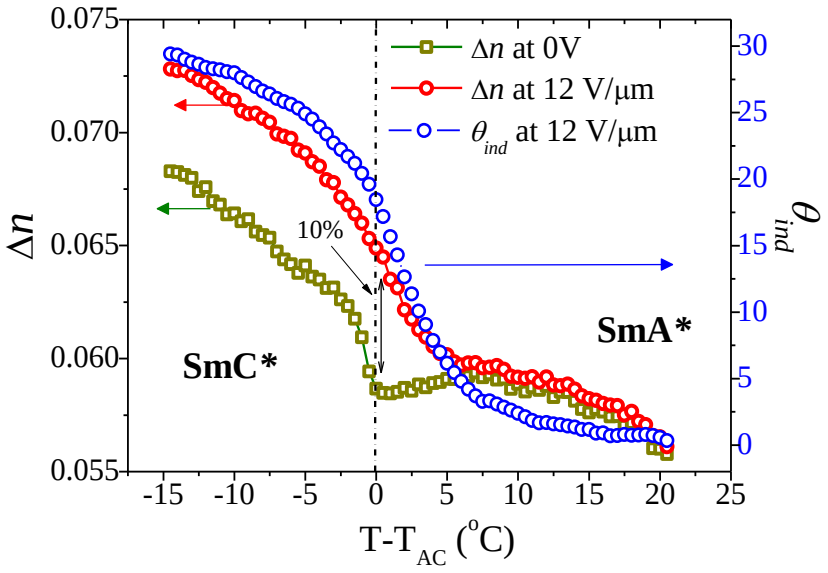

Figure 5.12 Temperature dependence of the birefringence with and without electric field.Also temperature dependence of the apparent tilt angle for a maximum applied field of 12 V/μm.

The birefringence and the apparent tilt angles are measured using ATP technique as described in the experimental section. A 3-μm thick planar-aligned cell is filled with adpc042 LC and triangular wave of amplitude of 12 V/μm electric field is applied across the cell at a frequency of 46 Hz.

Figure 5.12 shows the temperature dependence of birefringence and the apparent tilt angle. As seen earlier for other de Vries type LCs the birefringence for zero applied electric field, increases slightly at higher temperatures close to the Iso indicating decreasing tendency of thermal fluctuations. However on cooling, the birefringence decreases reaching minimum at T_{AC}. This is explained by the emergence of molecular tilt angle and its increasing tendency with the reduction in temperature in the previous section. adpc042 shows a 10% increase in the birefringence at T_{AC} with 12 V/μm field applied across it. The field induced birefringence increase is not as high as seen before in the other chiral de Vries smectics but is much higher than for conventional smectics. The apparent tilt angle shows a maximum of 20° at $T = T_{AC}$ with a field of 12 V/μm.

5.9 Mean-Field Langevin-Debye model

The modified GLD model produces a good quality fit with the observed experimental data. However, the obtained ODF shows that the model works only if the θ is restricted over a range of values. In spite of the quality of the fit, this generalisation of limiting the tilt angle to vary over a range of values is less physical. Therefore here we propose a new model for the apparent tilt angle as a function of applied electric field. In this new model the molecular tilt angle is allowed to vary from 0 to 90°. The Mean-Field Langevin-Debye (MFLD) model involves three fitting parameters for reproducing the experimentally observed EO response.

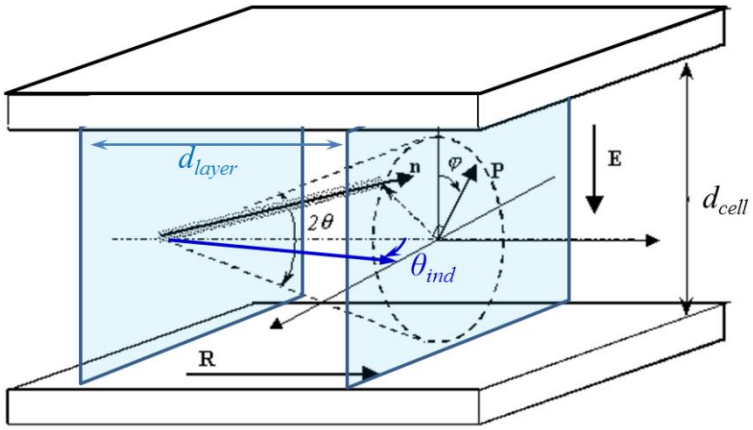

Figure 5.13 The laboratory co-ordinate system used in the MFLD model.

The Mean-Field potential of the MFLD model can be expressed as:

$$U = -p_0 E \sin\theta\cos\phi + A^2 \sin^2(\theta - \theta_0) \qquad (5.3)$$

Here the first term is the same as used in the GLD model, responsible for the usual dipole interaction energy with the applied electric field with p_0 is the local dipole moment of a tilt correlated domain. The second term in the above Equation (5.3) defines a mean-field cone distribution with an aperture angle of the cone as $2\theta_0$. The ODF width increases with increase in $\sqrt{k_B T}/A$. Here k_B is the Boltzmann constant, T

is the absolute temperature and A is the phenomenological co-efficient for zero field distribution. The second term in Equation 5.3 implicitly depends on the applied electric field. As discussed in the introduction two different types of ODF are used to describe the de Vries nature in literature. i) Sugar-loaf shaped ODF, is unimodal Gaussian type distribution, the maximum appears at θ=0°. ii) Volcano or diffuse cone shaped ODF, where the maximum occurs at a finite non-zero value of θ. Note that the MFLD model will produce "Sugar-loaf" like ODF for $\theta_0 < \sqrt{k_B T}/A$ and will produce "diffuse cone" like ODF for $\theta_0 > \sqrt{k_B T}/A$ as shown in Figure 5.13. The ODF of MFLD model is expressed as,

$$f(\theta,\phi) = \exp[-U/k_B T] / \int_0^{\pi/2}\int_0^{2\pi} \exp[-U/k_B T]\sin\theta d\theta d\phi \qquad (5.4)$$

The average of a physical parameter 'x' in modified GLD model is evaluated as given below,

$$< x >= \int_0^{\pi/2}\int_0^{2\pi} x(\theta,\phi) f(\theta,\phi)\sin\theta d\theta d\phi \qquad (5.5)$$

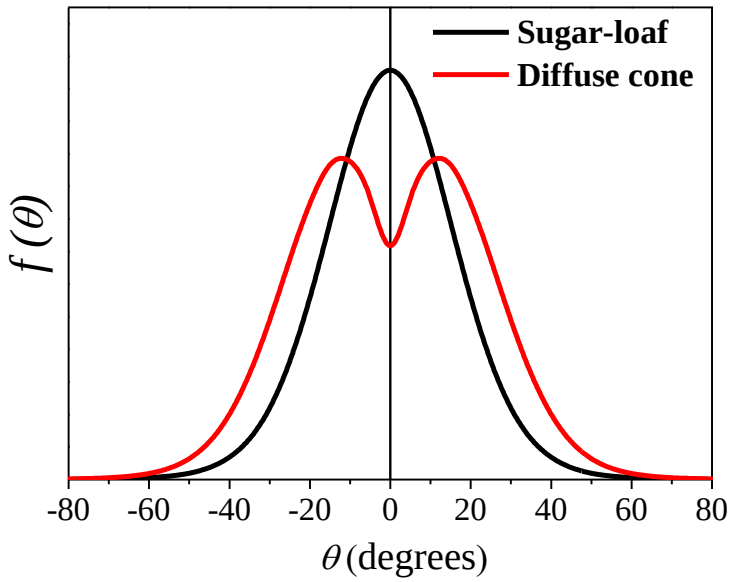

Figure 5.14 2D representation of Sugar-loaf and Diffuse cone molecular ODFs.

Figure 5.15 shows electric field dependent apparent tilt angle fitted with the MFLD model for a range of temperatures in SmA*. The EO response is linear for temperatures close to the Isotropic phase. On cooling the sample, the response attains a Langevin-like function. Surprisingly adpc042 does not exhibit the characteristic sigmoidal EO response. Hence we can neglect the higher order (E^2) electric field dependent term in the Mean-Field potential. The MFLD model produces an excellent fit to the experimentally observed EO response. However, the MFLD model can work only for the field dependent apparent tilt angle.

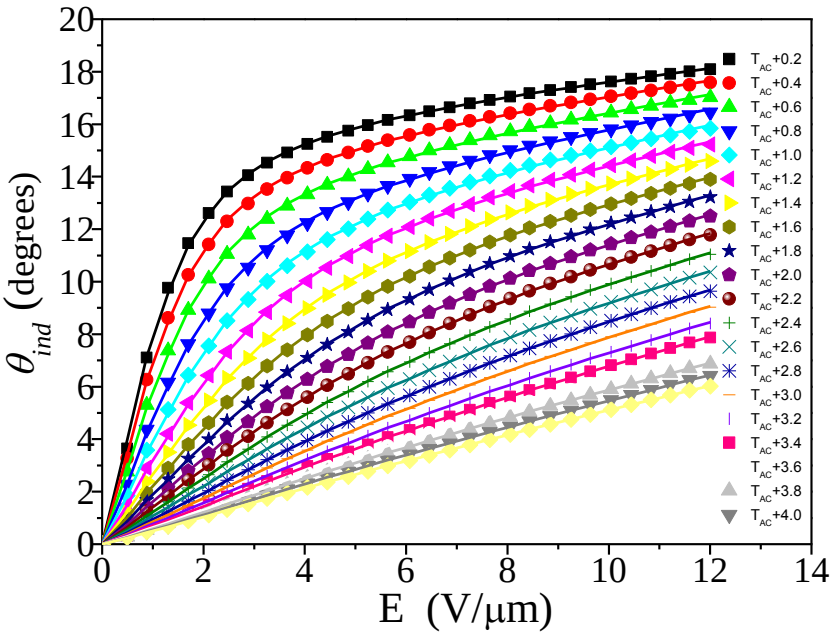

Figure 5.15 Apparent tilt angle as a fuction of the applied eletric field across a cell. Symbols: Experimental values. Solid line: MFLD model fit.

Both fitting parameters p_0 and A increase smoothly and diverges close to T_{AC} due to a growth in the size of the tilt correlated domain (Figure 5.16).

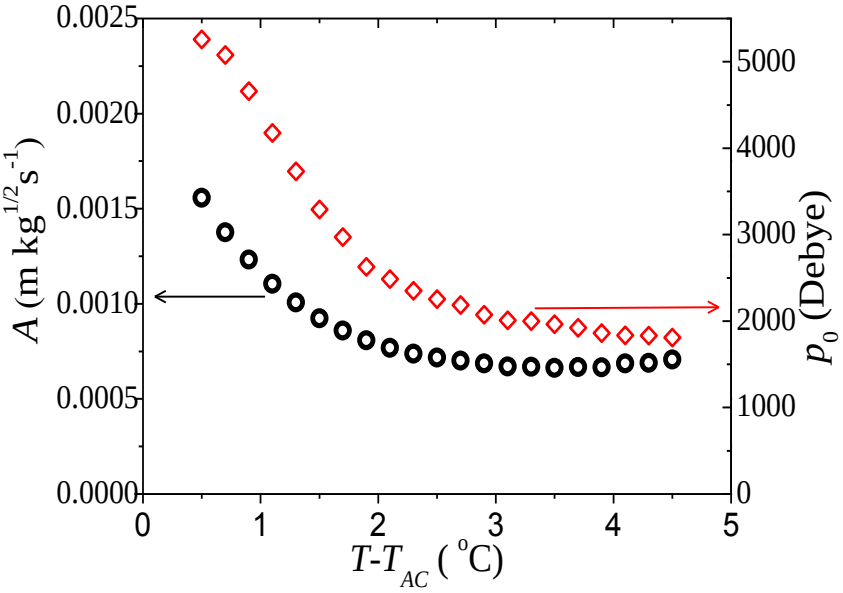

Figure 5.16 The temperature dependence of MFLD model fitting parameters p_0 and *A*.

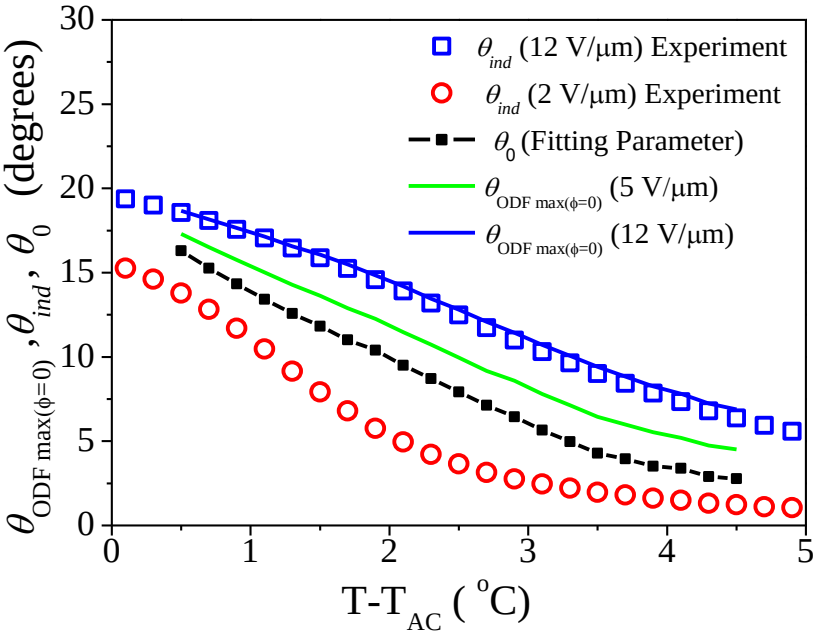

Figure 5.17 Comparison of the various different tilt angles as a function of temperature: θ_0 – fitting parameter, θ_{ind} – apparent tilt angle and $\theta_{ODFmax\ (\phi=0)}$ – position of the ODF maxima.

Figure 5.17 shows that on cooling the cell, the fitting parameter θ_0 increases almost linearly from ~2° to 16.5°. This clearly indicates the variation of the diffuse cone angle with temperature. The maximum field induced apparent tilt angle (Blue squares in Figure 5.17) is much higher than the diffuse cone angle, showing that the

de Vries smectic materials exhibit huge electro-clinic effect. On applying the electric field, the diffuse cone distribution is distorted; this is clearly evident from the simulated θ_{ODFmax} values corresponding to a maximum of the ODF with applied electric field (Solid lines in Figure 5.17). The experimental values of θ_{ind} for 12 $V\mu m^{-1}$ are slightly lower than θ_{ODFmax} for the same applied electric field. This is expected from a highly distorted diffuse-cone ODF due to the large applied electric field. The ODF of adpc042 at T_{AC}+1 °C is shown in Figure 5.17.

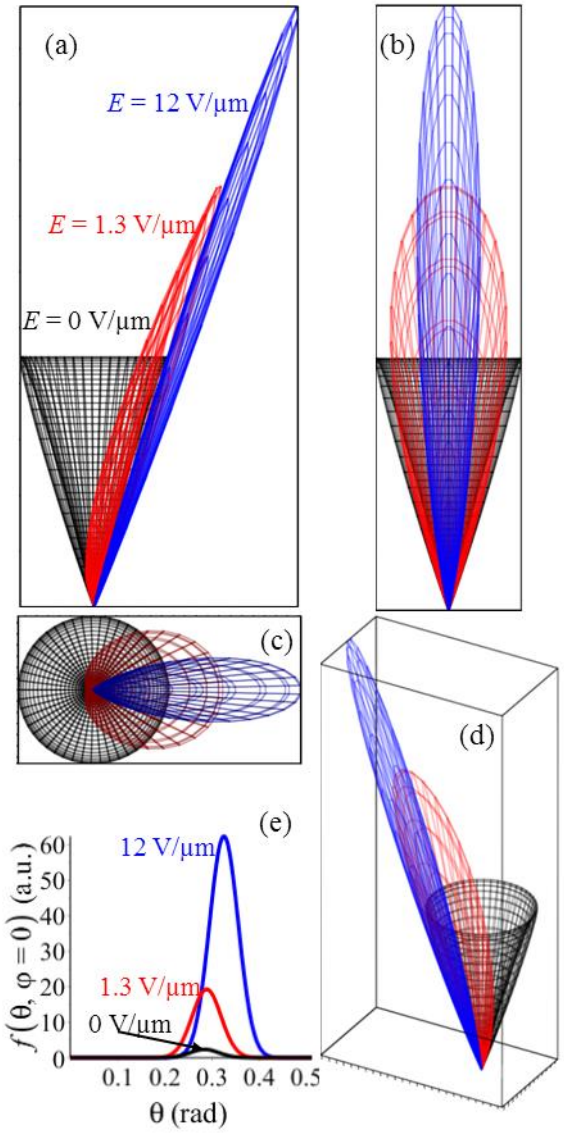

Figure 5.18 ODF for adpc042 obtained from MFLD model for a particular temperature (T = T_{AC} +1 °C) and for different applied electric fields. (a-d) - 3D ODF is shown in different axonometric projections. e) 2D representation of the same ODF.

The ODF is normalised as shown below such that the volume of ODF remains constant for different applied electric fields.

$$Normalised\ ODF = \frac{f(\theta,\phi)}{\sqrt[3]{\int_0^{2\pi}\int_0^{\pi/2} f(\theta,\phi)^3 \sin\theta d\theta d\phi}} \tag{5.6}$$

Moreover, by using the local dipole moment value obtained from the fit, we can estimate the effective size of a single tilt correlated domain; using the procedure similar to the one described in [42]. Here we use p_0 ~5000 Debye at 0.5 °C above T_{AC}. The effective single molecular dipole moment can be estimated with the relation given below:

$$\mu_{eff} = \frac{P_{S-\max} M}{\rho N_A \sin\theta_{indsat}} \tag{5.7}$$

Here $P_{S-\max}$ is the measured saturated value of the spontaneous polarisation which is 69 nC/cm^2 from Figure 5.10, M = 590.3 g/mol - molar mass, ρ = 1.2 g/cm^3 - density, N_A is the Avogadro number and θ_{indsat} = 30° is the saturated apparent tilt angle with the maximum applied electric field. With the data given above the effective molecular dipole moment is estimated to be μ_{eff} ~ 0.34 Debye. Therefore from the local dipole moment value obtained from the fit for adpc042, the tilt-correlated domain consists of approximately 6000 molecules near the Iso-SmA* phase transition and grows to ~15000 molecules near $T_{AC.}$ The effective length of the tilt-correlated domain can be estimated from:

$$\text{Correlation length - } \xi = \sqrt[3]{\frac{p_0 \sin\theta_{indsat}}{P_{S-\max}}} \qquad (5.8)$$

For adpc042 the tilt-correlated domain length is calculated to be of the order ~**30nm** for temperatures close to SmA*-SmC* phase transition.

Figure 5.19 illustrates the difference between the $\sqrt{k_B T}/A$ and θ_0 as a function of temperature in SmA* phase. We can clearly see that the crossover between Sugar-loaf and Diffuse cone happens approximately around 2-3 °C above T_{AC}.

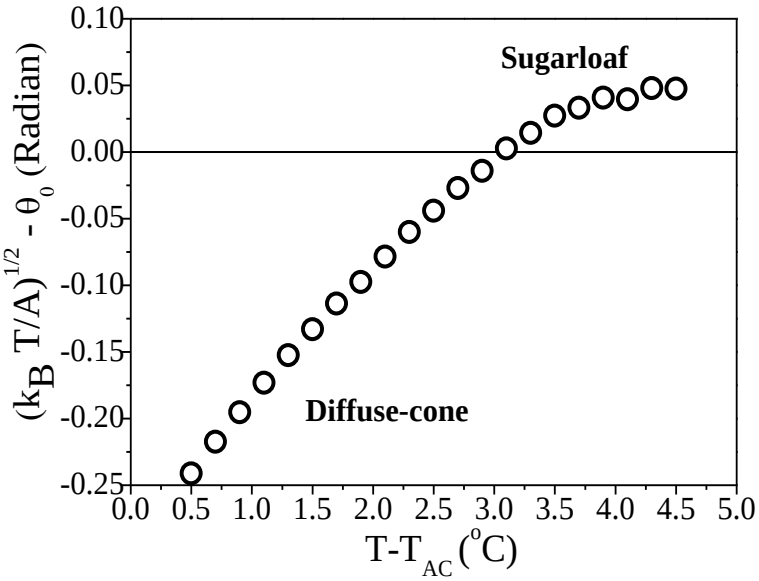

Figure 5.19 The difference between $\sqrt{k_B T}/A$ and θ_0 is plotted as a function of temperature.

In order to investigate the differences between the various EO models, we fit experimentally obtained θ_{ind} as a function of applied electric field using different models. We used the following three different models:

1. Hollow cone model [41]
2. GLD model [42]

3. MFLD model [94]

The models given above produced a reasonably good fit to the apparent tilt angle for low values of applied electric field. However, in Figure 5.20 we can clearly see that MFLD model produces a better fit for the entire range of the applied electric fields. The comparison is quantified by the sum of squares of the residuals (χ^2) for the different models, shown in Figure 5.21. Furthermore, the continuous smooth molecular distribution obtained from MFLD model for SmA* phase seems to be more physically meaningful (Figure 5.21).

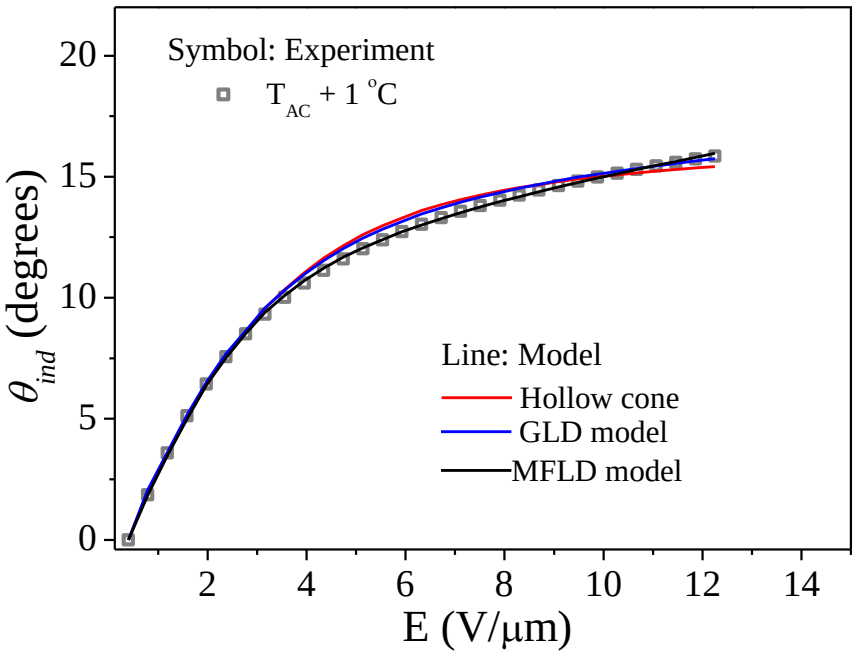

Figure 5.20 The apparent tilt angle as a function of the applied electric field fitted with different models. Symbols: Experiment. Solid lines: Different models.

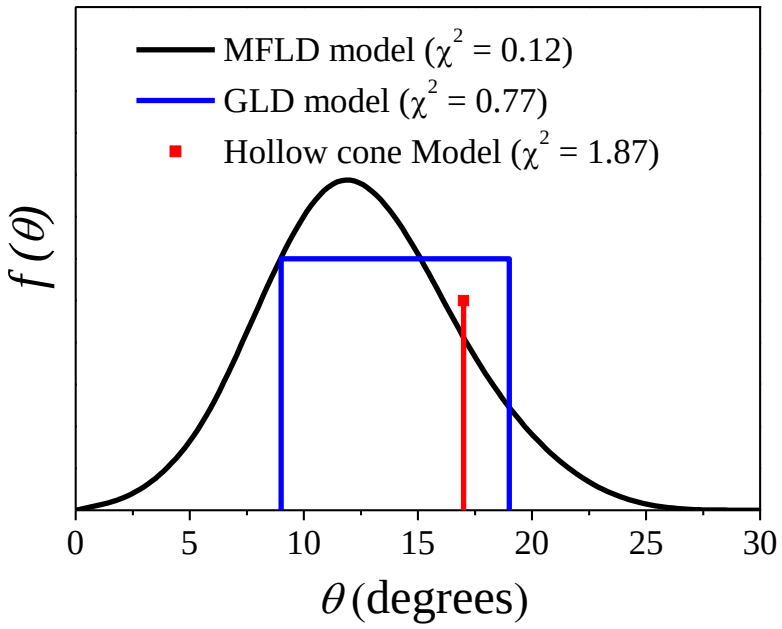

Figure 5.21 2D representation of ODF obtained from the fit using different models.

5.10 Conclusions

In this chapter we focused on addressing the limitations of the GLD model. In the first section, we investigate the results of a chiral LC DR276, based on carbosilane end tail with 5-phenyl-pyrimidine benzoate core. DR276 shows a maximum layer shrinkage of ~1.9% at 10 °C below T_{AC} and reduction factor **R** of DR276 is ~0.3. Based on the experimental results, DR276 is considered to be a good de Vries smectic material. DR276 also shows the characteristic trend reversal in the temperature dependent layer thickness and birefringence data as a function of the temperature. We modify the GLD model based on the speculations from the temperature dependent birefringence experiment. The lower integration limit θ_{min} of the ODF is replaced with θ_T, it depends on temperature and it is released to act as a new fitting parameter in the model. This modification brings a good quality fit with the measured field dependent EO response. From the fitting results we show that all the fitting parameter increases on cooling and follow a power law function. This

leads to a conclusion that the new fitting parameter varies with temperature as expected and the diffuse cone angle shows an increases approaching T_{AC}. For DR276 θ_T varies from 14º to 18º for a given range of temperatures in SmA* phase. In the second section of this chapter, we study another new de Vries type LC based on epoxyhexoxy backbone with 5-phenyl-pyrimidine core terminated with a tri-siloxane group named as adpc042. In order to continue the improvisation of EO modelling, we propose a new model, where the tilt is allowed to vary from 0 to 90° expecting a continuous ODF. MFLD model involves a Mean-Field potential which comprises a field independent mean-field cone distribution and the first order field dependent local dipole moment term from the GLD model. This model contains three fitting parameters and these produce an excellent fit to the EO of adpc042. The fitting parameters diverge on approaching T_{AC} as expected. From the obtained local dipole moment and polarization density of adpc042, tilt-correlated domain length is estimated to be of the order **~30nm** for temperatures close to SmA*-SmC* phase transition. At this stage we compare the ODFs obtained from the different models used so far for the EO modeling and we show that MFLD model produces a continuous ODF in de Vries SmA* phase with the peak of molecular distribution coinciding with a non-zero molecular tilt, supporting the diffuse cone formalism.

Chapter 6

6. Comparative Study of Two Chiral Smectics

6.1 Introduction

In this chapter we carry out studies on two analogues chiral smectic materials for de Vries characterisation.

In the previous chapter, we have seen that MFLD model produces a continuous ODF with the maximum of the probability occurring at a finite angle; supporting the diffuse cone formalism. However, from the natural distribution of molecules at zero electric field one can estimate order parameter of a LC system. The narrow ODF in SmA* phase obtained from MFLD model yields an order parameter equivalent to ~0.9. This clearly suggests that MFLD model over estimates the order of the system under study. This is considered to be one of the main drawbacks of the MFLD model. Moreover, MFLD model can work only for materials which do not exhibit the sigmoidal shaped electro-optic response .

In this chapter we address the above mentioned limitations of MFLD model. We propose a new model, based on the modified Maier-Saupe molecular distribution at zero field and Langevin-Debye type Mean-Field potential for field dependent birefringence. The Maier-Saupe Langevin-Debye (MSLD) model is used to fit the electro-optic results obtained for the two new chiral de Vries smectics. From the modelling, we obtain the temperature dependent order parameter from birefringence measurements.

In this chapter we compare the electro-optic results of conventional smectics with de Vries smectics.

6.2 Materials under investigation

Figure 6.1 shows molecular structures of DR133 and DR118. DR133 is based on 5-phenyl-pyrimidine benzoate core while DR118 is based on 5-phenyl-pyrimidine benzene core. Both DR133 and DR118 are terminated with trisiloxane end chain separated by an alkyl spacer on one side and the chiral (S) alkyl end chain on the other side. Table 6.1 shows the phase transition temperatures of DR133, DR118 and the commercial FLC mixture Felix 18/100 from Hoechst Ltd.

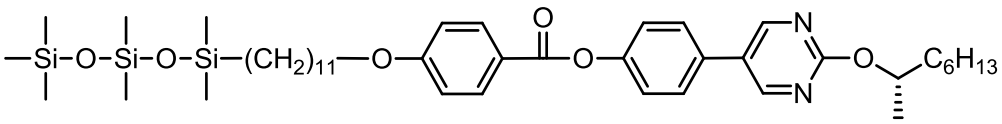

(a)

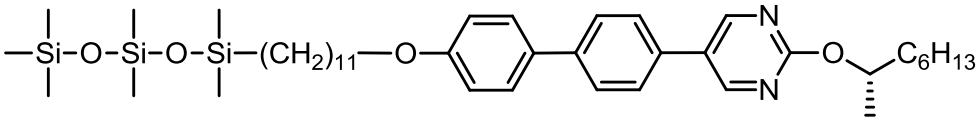

(b)

Figure 6.1 Molecular structures of (a) DR133 and (b) DR118.

Table 6.1 Phase transition temperatures of DR133 and DR118.

Materials	Phase Sequence
DR133	Cryst **11 °C** Sm*C** **94 °C** Sm*A** **102 °C** Iso
DR118	Cryst **60 °C** SmC* **95 °C** SmA **113 °C** Iso
Felix 18/100	SmC* **73.1 °C** SmA* **83.8 °C** N* **88.5 °C** Iso

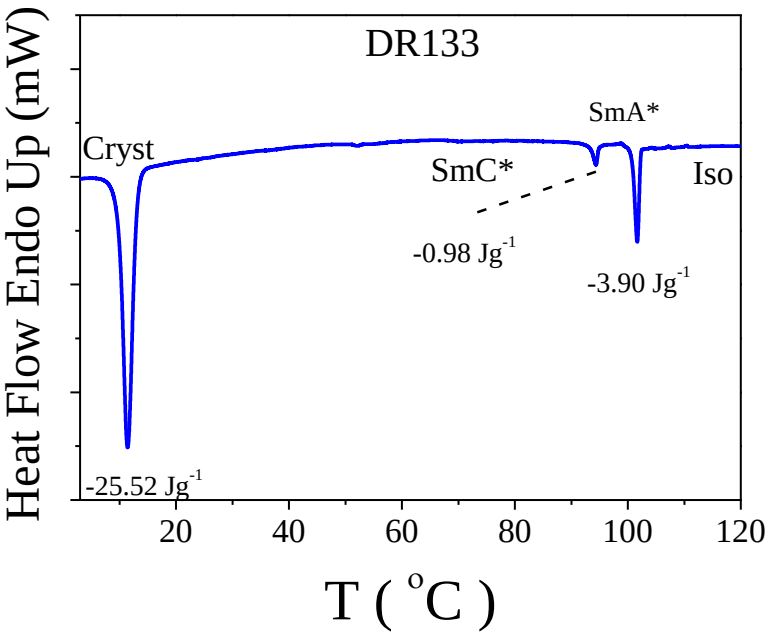

(a)

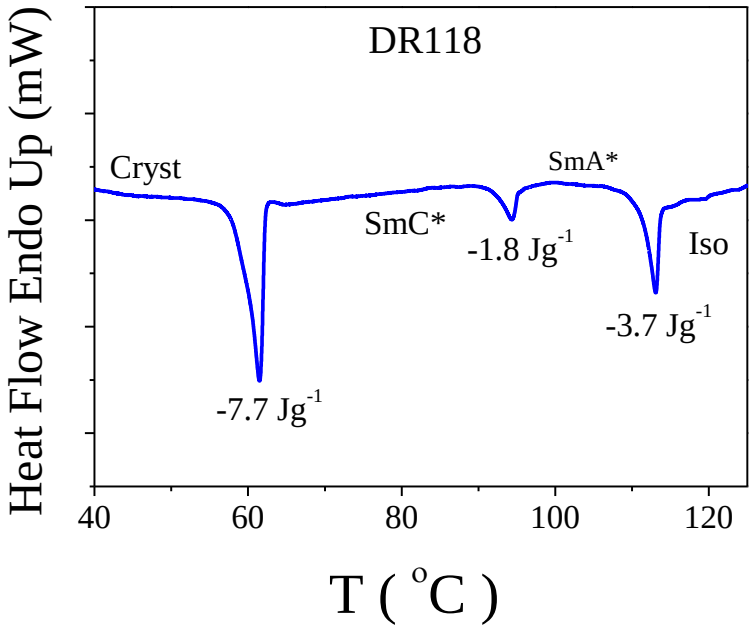

(b)

Figure 6.2 DSC thermograms of (a) DR133 and (b) DR118 under cooling at a scan rate of 10 °C/min showing different phases with transition enthalpies ΔH in Jg^{-1}.

Figure 6.2 represents the DSC thermograms of DR133 and DR118. An observed small enthalpy change at the SmA*-SmC* phase transition temperature

suggests that both materials exhibit weak first order phase transition, typical for de Vries smectic LCs.

6.3 Layer thickness measurements

The temperature dependent layer thickness is obtained using X-ray diffraction method facility at the University of Warsaw, Poland. The measurements were carried out on Bruker D8 diffractometer using Cu-K_α source at a wavelength 0.154 nm. The X-ray measurement was carried out under cooling with a ramp rate of 0.1 °C. We have also conducted FSF optical thickness measurements for DR133 and DR118 using a high resolution method as described in the experimental methods of this thesis. The temperature axis of the FSF optical thickness data is normalised at T_{AC}. As discussed in the earlier chapters the normalized FSF optical thickness deviates from the measured X-ray layer thickness in the SmC* phase due the appearance of the molecular tilt, responsible for an increase in the effective refractive index of the FSF film. Here we propose a simple method for correcting FSF optical thickness data using the birefringence X-ray layer thickness data in order to demonstrate the validity of FSF technique. This procedure allows us to estimate the number of layers in a FSF and to obtain the tilt angle responsible for the increase in the optical thickness, by using the hard rod approximation model.

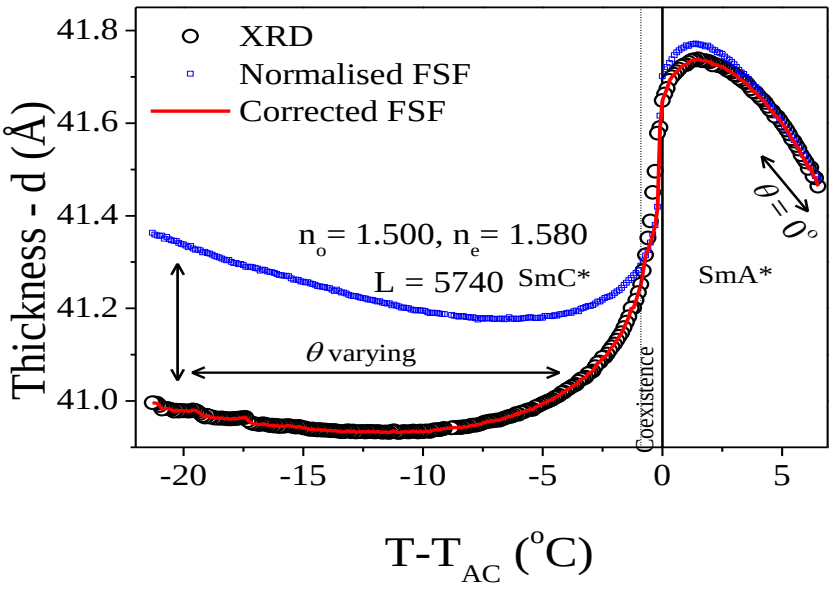

(a)

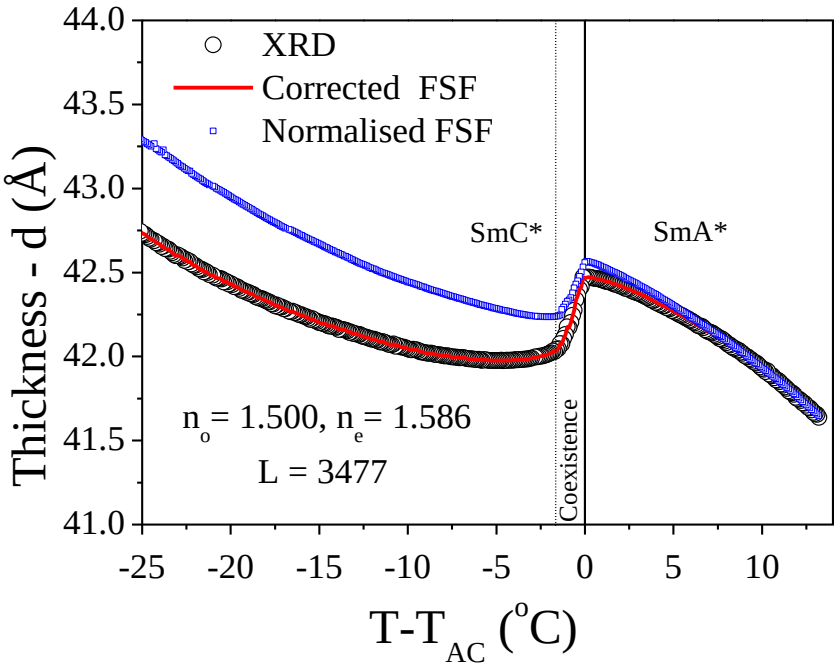

(b)

Figure 6.3 Temperature dependence of the layer thickness determined from X-rays and normalised FSF optical thickness for (a) DR133 and (b) DR118. Red line represents the corrected FSF thickness with X-rays layer thickness. Coexistence region is represented by dotted line.

6.3.1 Free-Standing film thickness correction

The optical thickness of a FSF can be expressed as,

$$Optical\,Thickness = n_{eff} Ld \tag{6.1}$$

where n_{eff} is the effective refractive index, L is the number of smectic layers in the FSF and d is the thickness of a single smectic layer.

For a non-polarised white light the effective refractive index can be approximated as,

$$n_{eff} = \frac{n_o + n(\theta)}{2} \tag{6.2}$$

Where n_o is the ordinary refractive index for the sample in homeotropic alignment $n(\theta)$ can be defined as,

$$n(\theta) = \frac{n_o n_e}{\sqrt{n_o^2 \sin^2\theta + n_e^2 \cos^2\theta}} \tag{6.3}$$

On assuming n_o = 1.5 and $\theta \sim 0°$ for temperature close to SmA*-Iso (perfect homeotropic), the effective refractive index will be $n_{eff} = n_o$. On the basis of the approximation we can find the number of layers L of the FSF which correspondingly coincides with d measured from the X-ray diffraction. The number of layers in the FSF for the particular experiment is estimated to be L = 5740 and L = 3477 for DR133 and DR118, respectively. These show good agreement with the X-ray layer thickness for the temperatures close to SmA*-Iso phase transition (Figure 6.3). On cooling, the appearance of molecular tilt θ leads to the contribution of $n(\theta)$ which results in the apparent increase of FSF thickness. This change can be observed from the deviations of normalised FSF optical thickness to the thickness measured using X-ray (Figure 6.3 (a) and (b) (Blue boxes)). Figure 6.4 (a) and (b) show the estimated

value of θ from the correction for n_e = 1.580 (DR133) and n_e = 1.594 (DR118) as a function of temperature. The values of n_o and n_e are approximated from the birefringence measurements (Figure 6.7). The corresponding thickness is shown in Figure 6.3 (a) and (b) (Red line). The variation of the tilt in SmC* clearly shows a power law dependency as function of temperature with a critical exponent β.

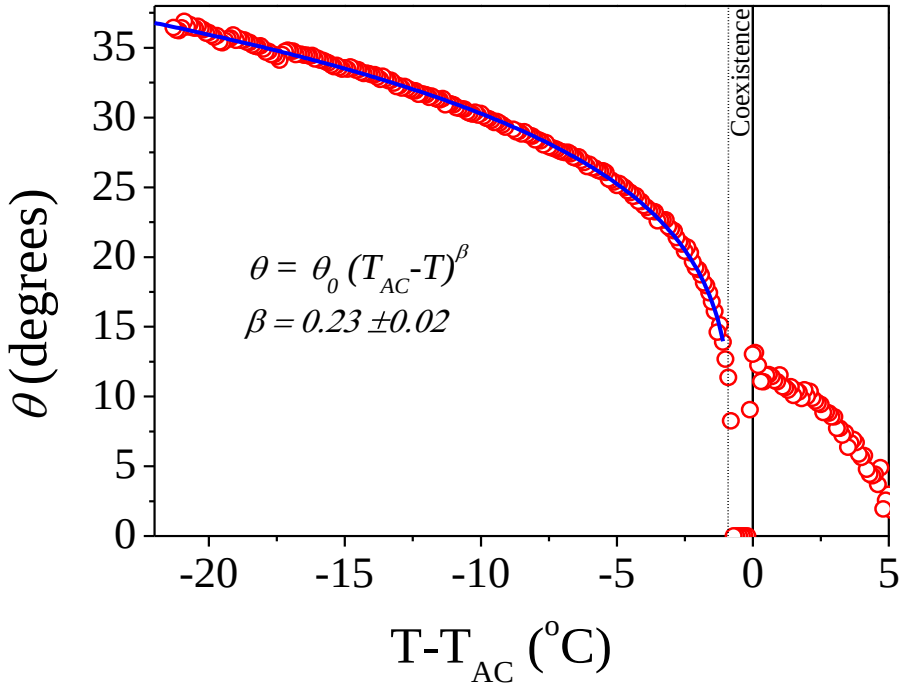

(a)

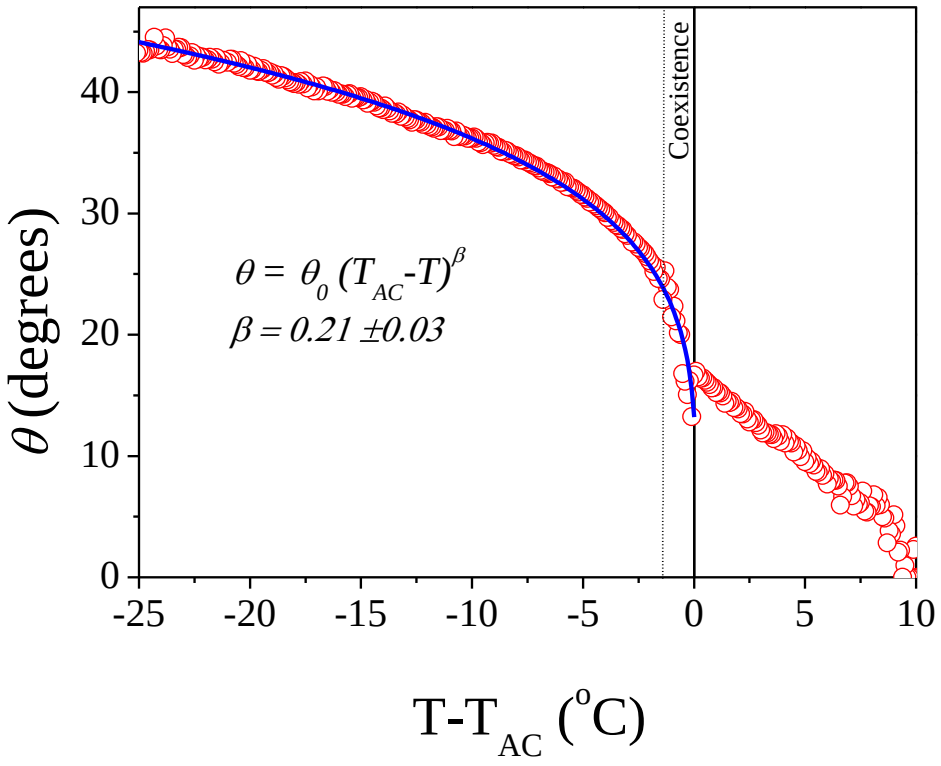

(b)

Figure 6.4 Temperature dependent θ estimated from the FSF thickness correction with layer thickness measured from X-ray method. Solid line: Power-Law fit.

Table 6.2 Layer shrinkage and reduction factors for DR133 and DR118.

Material	T_{AC} (°C)	d_{AC} (Å)	d_C (Å) at T- T_{AC} (°C)	Layer Shrinkage	θ_{indsat} (degrees)	***R***
DR133	95	41.6	40.9 at -11	1.7%	34.5	0.3
DR118	94	42.4	41.9 at -5	1.2%	35.5	0.2

The layer shrinkage and reduction factors of DR133 and DR118 are shown in Table 6.2.

6.4 Electro-optic measurements

The EO measurements of Felix 18/100 were made using a 2.4 µm planar-aligned cell using ATP technique. Figure 6.5 shows a comparison of the apparent tilt angle as a function of the reduced temperature for conventional smectics (Felix 18/100) and de Vries type smectics (DR133). The apparent tilt angle for a minimum field (0.1 V/µm) shows similar response for both Felix 18/100 and DR133. However high applied field (20 V/µm) clearly shows that de Vries smectics exhibit huge electroclinic tilt in SmA* phase whereas Felix 18/100 exhibits relatively low apparent tilt angle. The large field induced apparent tilt angle in DR133 directly results in field induced increase in the birefringence (Figure 6.7 (a)). Such a behaviour is absent in a conventional smectic, as seen in Figure 6.6 the applied electric field induces only 1.2% increase in the birefringence at $T=T_{AC}$ for Felix 18/100.

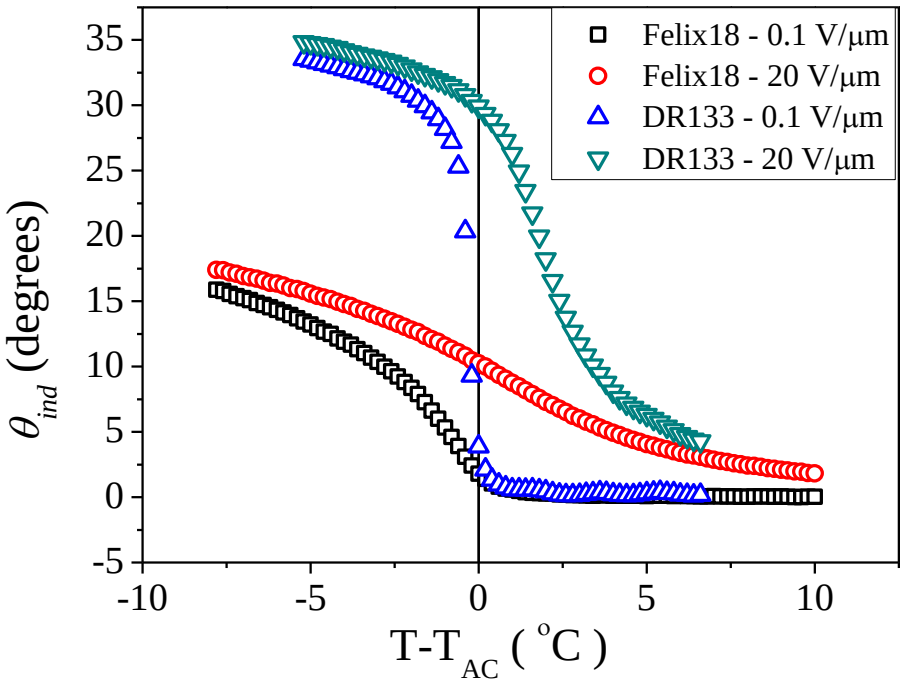

Figure 6.5 A comparison of temperature dependent apparent tilt angle from conventional and de Vries type smectic LC for minimum and maximum applied fields.

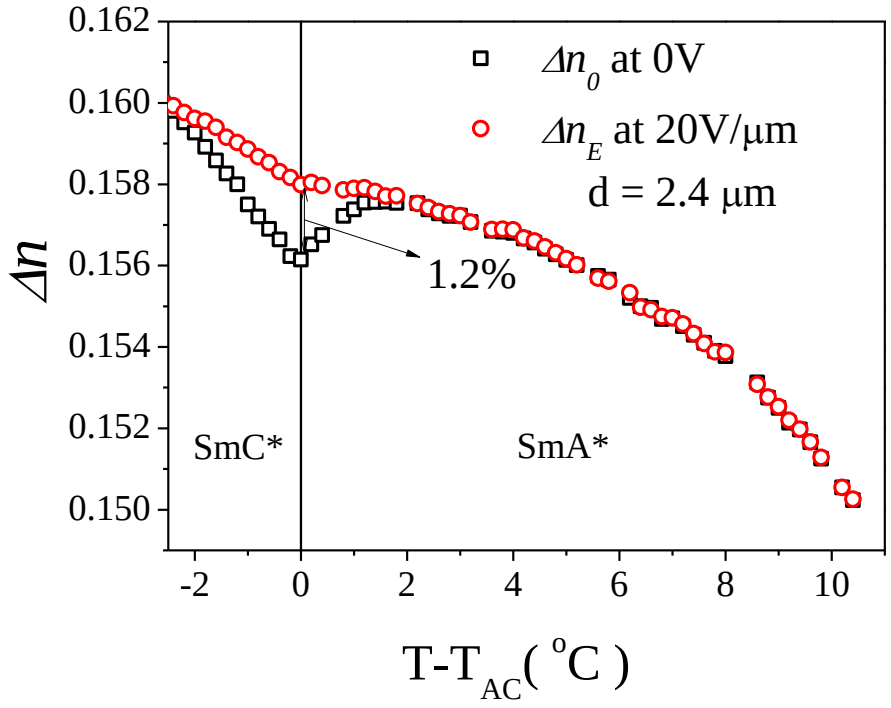

Figure 6.6 Birefringence as a function of reduced temperature for Felix 18/100 FLC mixture.

The EO measurements were made using 1.9 μm planar-aligned cell for DR133 and 1.6 μm planar-aligned cell for DR118. As seen earlier for other chiral de Vries smectic materials the zero field birefringence (Δn_o) as a function of temperature shows trend reversal for both DR133 and DR118 in Figure 6.7 (a) and (b) respectively. This anomalous decrease in Δn indicates the emergence of molecular tilt where the azimuthal angle ϕ of the molecular directors is distributed around a cone for maintaining the uniaxiality of SmA* phase. Since the molecular distribution is spatially averaged in the optical experiment, the effective value of birefringence decreases. On applying the electric field across a planar-aligned cell, birefringence Δn_E does not change with field close to the isotropic state for both DR133 and DR118. However on approaching T~ (T_{AC} + 3) °C for DR133 and T ~(T_{AC} + 5) °C for DR118, we observe a significant increase in Δn_E with the electric field of 20 V/μm. On further cooling, Δn_E diverges and is 30% higher for DR133 and

37% for DR118 than Δn at zero field at T_{AC}. This implies that in close proximity to T_{AC}, applied electric field lifts degeneracy in azimuthal angle ϕ while the molecular directors are redistributed by the field. The birefringence reaches a maximum of Δn_{max} = 0.085 for DR133 in SmC* phase at ~15 °C below the T_{AC} and Δn_{max} = 0.093 for DR118 at ~ 30 °C.

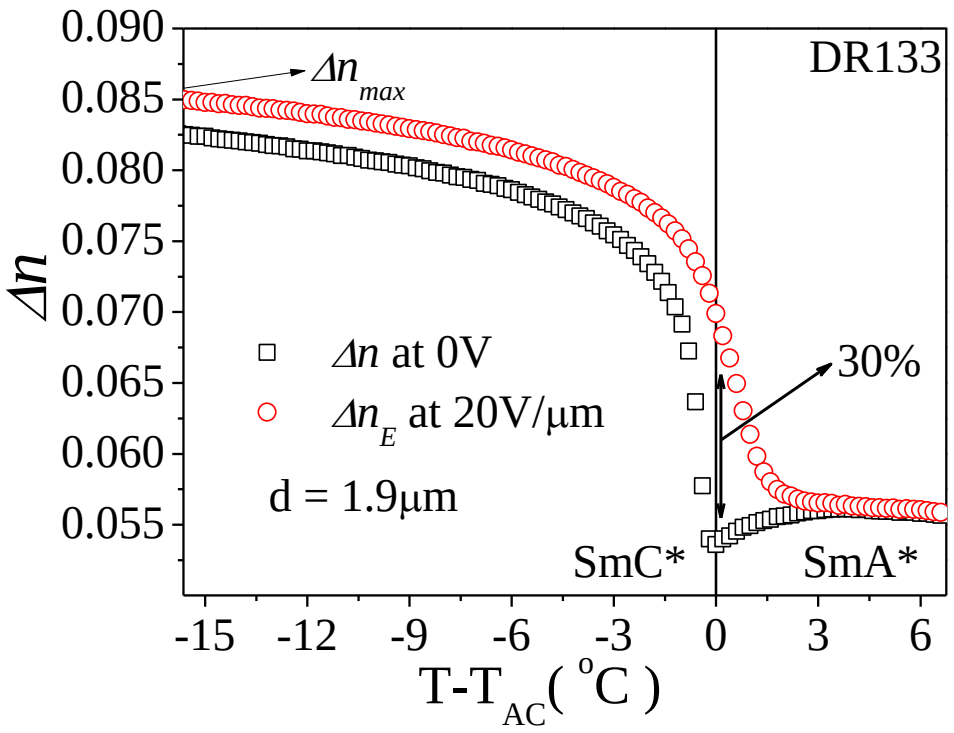

(a)

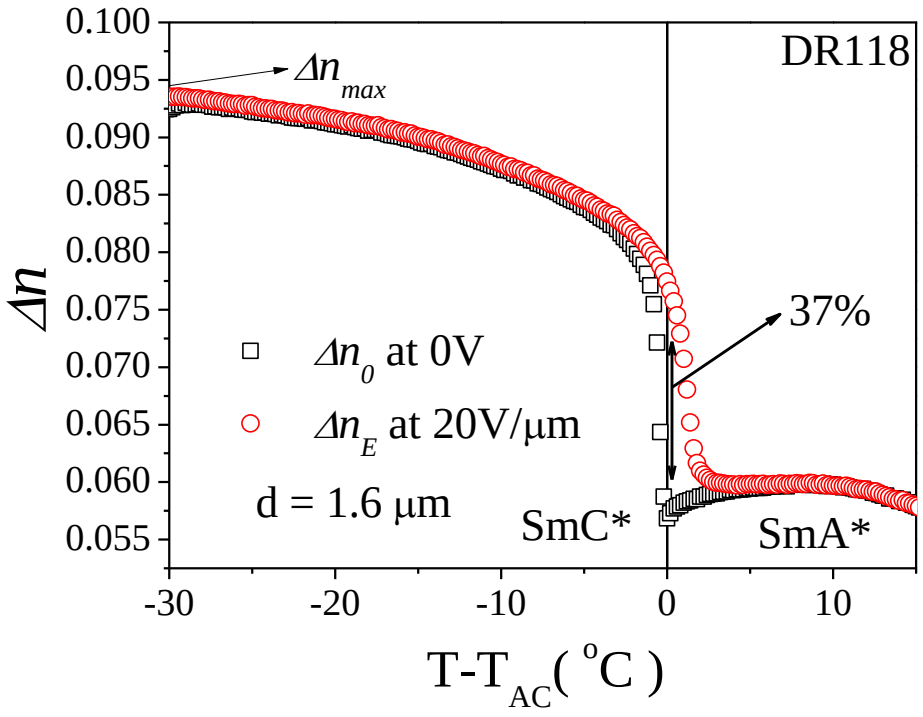

(b)

Figure 6.7 The temperature dependence of Δn for zero and 20 V/μm applied electric fields for (a) DR133 (b) DR118.

Plots of Δn normalised by its maximum value Δn_{max} are shown as a function of the electric field for different temperatures in Figure 6.9 (a) and (b) for DR133 and DR118 respectively. The experimental data (presented as symbols) are fitted to the model defined by Equation 6.8. Fits of the data to the model are shown by solid red lines. We note that $\Delta n/\Delta n_{max}$ increases linearly with the field at higher temperatures in SmA* phase *i.e.* particularly closer to the Iso. - SmA* transition temperatures. While on cooling, the electric field saturates Δn as well as leads to a sigmoidal-shaped response, seen at $T \leq (T_{AC} + 1.8)$ °C for DR133 and $T \leq (T_{AC} + 2.0)$ °C for DR118.

One of the arguments regarding the observed huge field induced birefringence and apparent tilt angle is, that the applied large field induces phase transition (to SmC* phase) near T_{AC} for de Vries type smectics. In order to address the above

argument the comparison of Δn response in SmA* phase and SmC* phase is shown in Figure 6.8.

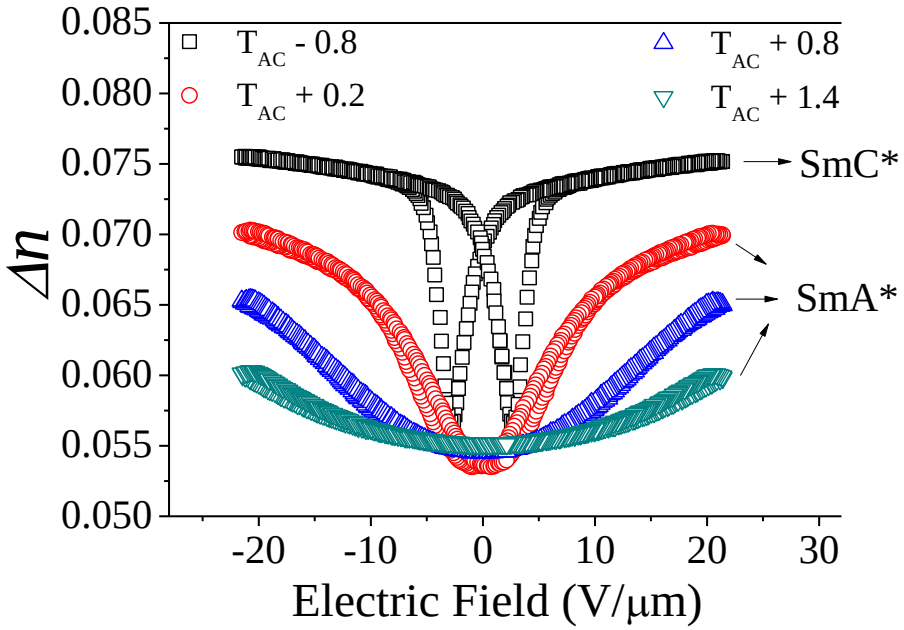

Figure 6.8 Birefringence as function of applied electric field for the entire range of positive and negative applied fields for DR133.

Some of distinct differences observed in SmA* and SmC* from Figure 6.8 are:

- In Sm*C** phase, the response saturates spontaneously for low values of the applied field, while in Sm*A** phase even for high electric fields the response does not attain a complete saturation.
- Sm*A** phase exhibits 'U' shaped switching, while SmC* phase exhibits 'V' shaped switching.
- We observe a prominent hysteresis in Sm*C** phase, which is typical for tilted phases, inferring bi-stability. Such hysteresis is absent in SmA* phase.

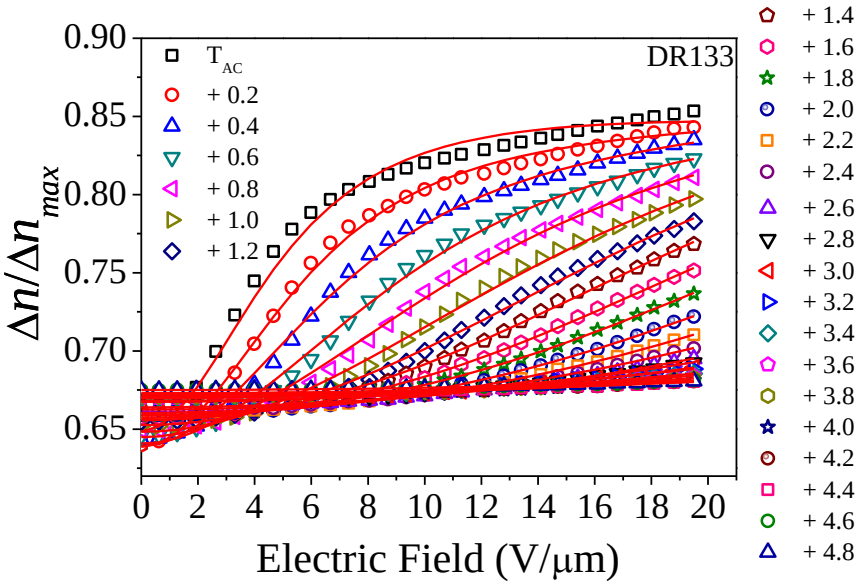

(a)

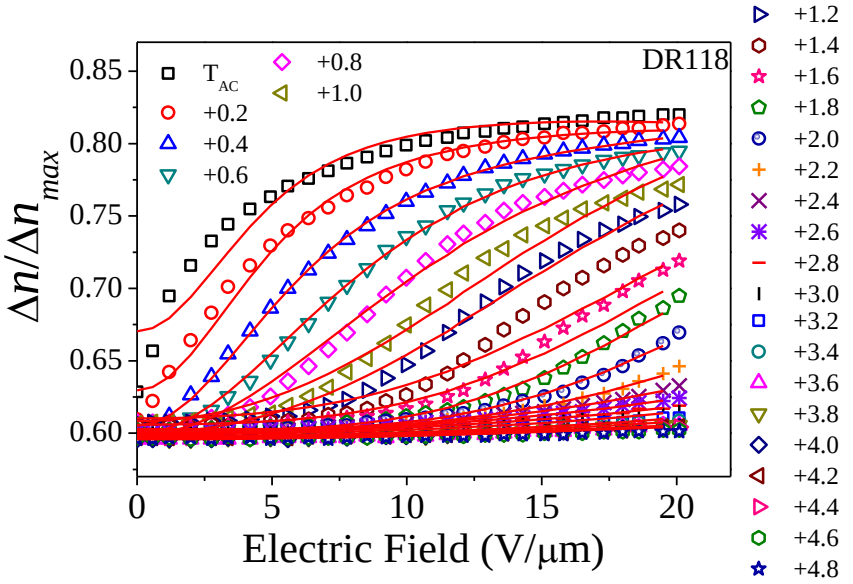

(b)

Figure 6.9 Normalized birefringence $\Delta n/\Delta n_{max}$ as a function of the applied electric field for a range of temperatures in SmA* phase for (a) DR133 and (b) DR118. Symbols: Experimental data. Solid red lines: MSLD model fit.

6.5 Maier-Saupe Langevin-Debye Model

The schematic representation of EO geometry in the laboratory frame with a representative molecule in molecular frame of reference is shown in Figure 6.10.

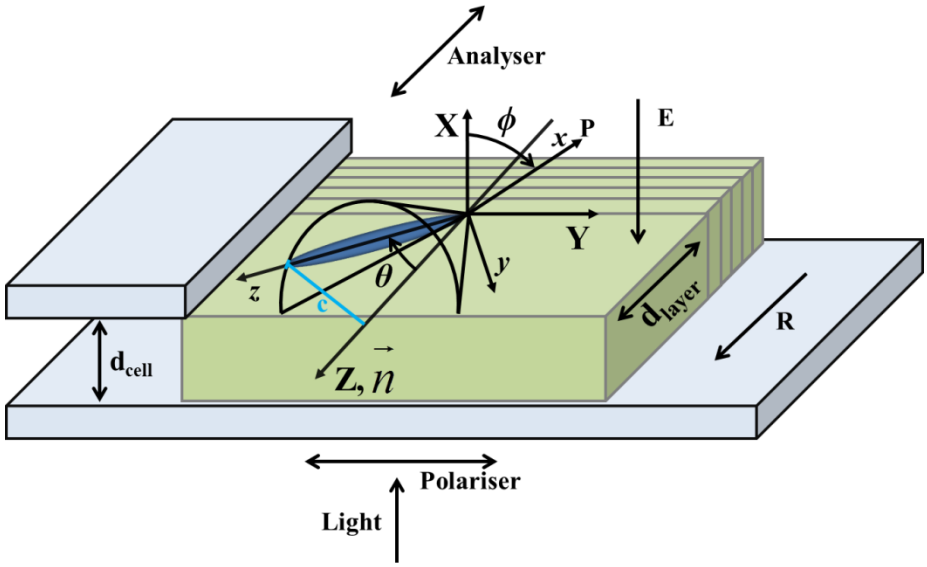

Figure 6.10 A schematic representation of the EO geometry of a planar-aligned cell. X, Y, Z and *x*, *y*, *z* are the laboratory and the molecular frames of references, respectively. The LC material is sandwiched in between the two ITO-deposited glass plates of cell thickness (d_{cell}). The molecular long axis *z* is tilted by an angle θ from the layer normal Z. The director $\vec{n}$ is parallel to the layer normal in SmA* phase for zero applied electric field. Here θ also represents the fluctuation angle around the director. The *c* director (shown as a blue line) is the projection of the molecular long axis on the smectic-layer plane where the induced polarization P, is normal to the *c* director. P makes an angle ϕ with the axis that is directed normal to the substrate, X. An electric field E is applied across the cell and is parallel to the smectic-layers. This brings about a change in the intensity of the transmitted light between the crossed polarizers by the field, with the light normally incident on the cell.

Theoretical approach to the EO modelling starts from the use of a Mean-Field potential of the generalised Langevin - Debye model [42] and by adding a modified Maier-Saupe distribution [24] energy term. Hence the Mean-Field potential *U* of the proposed model can be written as:

$$U = -A^2 \cos^2(\theta - \theta_0) - p_0 E \sin\theta \cos\phi(1 + \alpha E \cos\phi) \qquad (6.4)$$

Angles θ and ϕ are defined in terms of molecular and laboratory frames of references as shown in Figure 6.10. The electric field independent term $A^2 \cos^2(\theta - \theta_0)$ is the energy required to restore the constituent molecules to minimum packing entropy of the system. The MSLD model involves four fitting parameters to fit the experimental EO data. θ_0 is one of the model parameters which defines the maximum probable molecular long axis tilt with respect to layer normal in the absence of electric field. Here $p_0 \sin\theta$ is the magnitude of the dipole moment of a domain in which the tilt directions are correlated with each other. The linear term in $\boldsymbol{E}$ expresses the interaction of the dipole moment of this domain with the field. The quadratic term in $\boldsymbol{E}$ and its scaling factor α gives rise to tilt susceptibility for higher amplitudes of electric field. This term also leads to the sigmoidal EO response to the applied field.

Under the condition that, in SmA* phase the director is parallel to the layer normal. The order parameter of uniaxial liquid crystalline phase can be obtained from the Legendre polynomial-expansion coefficient:

$$P_2 = \frac{1}{2}(3\cos^2\theta - 1) \qquad (6.5)$$

Here θ is equivalent to the β which is usually defined as the fluctuation angle around the director.

The order parameter can be obtained by averaging the Equation 6.5 with the ODF as follows:

$$< x >= \int_0^{\frac{\pi}{2}} \int_0^{2\pi} x(\theta,\phi) f(\theta,\phi) \sin\theta d\theta d\phi \qquad (6.6)$$

$< x >$ denotes the ensemble average of 'x' ($i.e < x >=< P_2 >$). The mean-field molecular ODF $f(\theta,\phi)$ is defined as follows:

$$f(\theta,\phi) = \exp[-U / k_B T] / \int_0^{\frac{\pi}{2}} \int_0^{2\pi} \exp[-U / k_B T] \sin\theta d\theta d\phi \qquad (6.7)$$

U from Eq. (6.4) is inserted into Eq. (6.9) to obtain the ODF. The term $A^2 / k_B T$ describes the molecular tilt fluctuations and the ODF width decreases as $A^2 / k_B T$ increases, this is evident from Figure 6.11 (a), wider the ODF, lower is the order parameter and vice versa. Angle θ_0 defines the shape of the ODF (Fig. 4). For, $\theta_0 < k_B T / A^2$ we obtain a sugarloaf-like distribution (Gaussian distribution) function and for $\theta_0 > k_B T / A^2$ a volcano-shaped distribution function. Here $2\theta_0$ is defined as the 'aperture angle' of the volcano-shaped distribution function.

On neglecting the molecular biaxiality of liquid crystalline molecules and by averaging the dielectric tensor over the ODF, Shen *et al*. derived an expression for the normalized birefringence [42] as given below:

$$\frac{\Delta n}{\Delta n_{\max}} = \frac{< \cos^2\theta - \sin^2\theta \cos^2\phi >}{\cos 2\left(\frac{1}{2}\tan^{-1}\left(\frac{< \sin 2\theta \cos\phi >}{< \cos^2\theta - \sin^2\theta \cos^2\phi >}\right)\right)} \qquad (6.8)$$

Here Δn is the measured birefringence of the LC compound and $\Delta n_{\max}$ is the saturated birefringence at a temperature well within the Sm*C** phase for the maximum field applied across a planar-aligned cell. Averages in Equation (6.8) are estimated using Equation (6.6) by adopting the same procedure as given above.

The order parameter simulated using Equation (6.6) and (6.7) for zero electric field is shown in Figure 6.11 (*i.e* $E = 0$ thus $p_0 \& \alpha$ does not play any role in the calculations of the order parameter). The field-induced birefringence is obtained using Equation (6.8) as shown in Figure 6.13. The simulations are performed with the objective of determining the effect of θ_0 on values of the order parameters, ODF and the field induced birefringence.

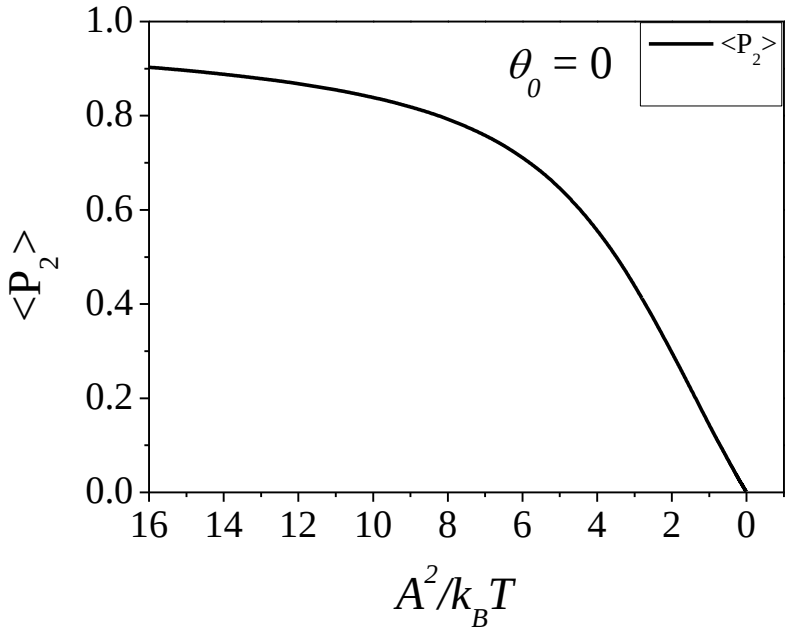

(a)

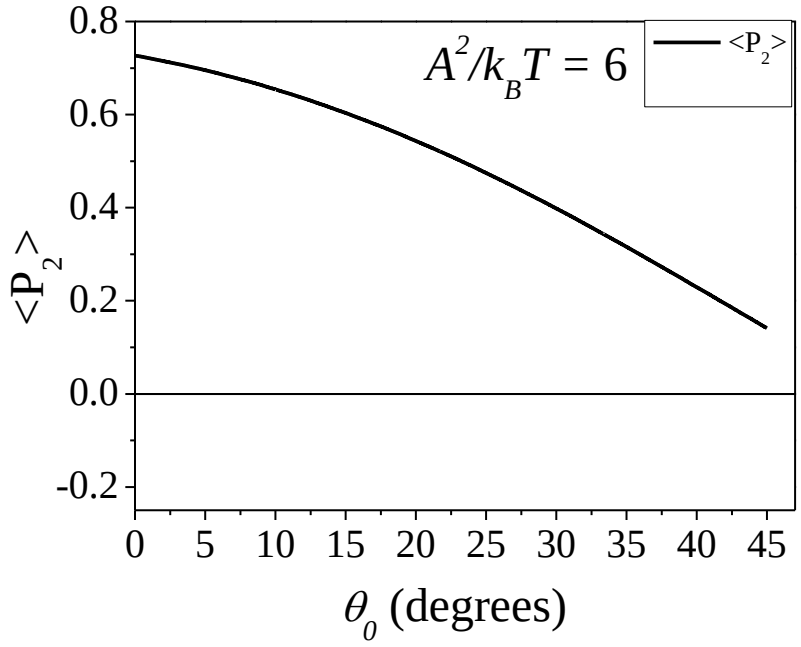

(b)

Figure 6.11 Relationship between (a) the orientational order parameter and $A^2 / k_B T$ for the sugarloaf-like molecular distribution, (b) the orientational order parameter is plotted vs. θ_0, for a fixed value of $A^2 / k_B T$. Both plots are in the absence of electric field.

The term $A^2 / k_B T$ describes the mean-field nematic interaction energy compared to the thermal energy. A higher value of $A^2 / k_B T$ implies a 'larger molecular interaction energy'. These are clearly evident from the large values of the orientational order parameter shown in Figure 6.11 (a) for large values of $A^2 / k_B T$. Figure 6.11 (b) shows a relationship between the orientational order parameter and θ_0, plotted for a fixed value of $A^2 / k_B T$. We find that for $\theta_0 = 0°$, the order parameter attains the maximum value. The simulation results do show that if $\theta_0 \neq 0°$, the order parameter is low as observed experimentally [23] for de Vries smectics.

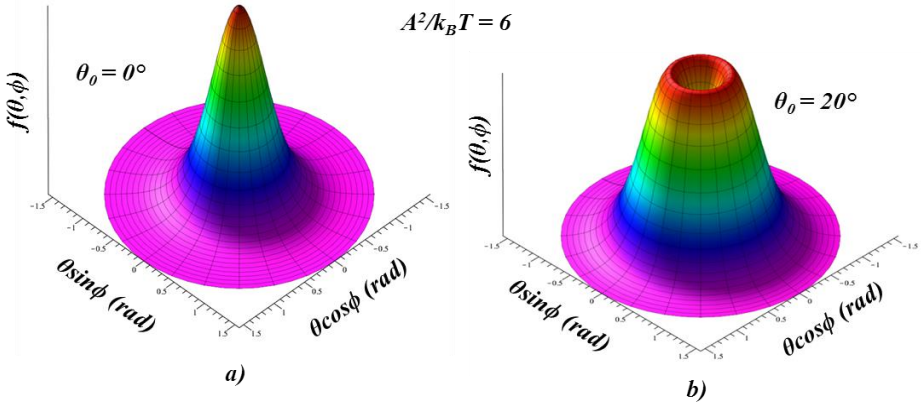

Figure 6.12 The effect of θ_0 on the shape of the distribution function, a 3-D representation of the ODF for (a) θ_0 = 0° and for (b) θ_0 = 20°, in both cases, $A^2 / k_B T$ is fixed.

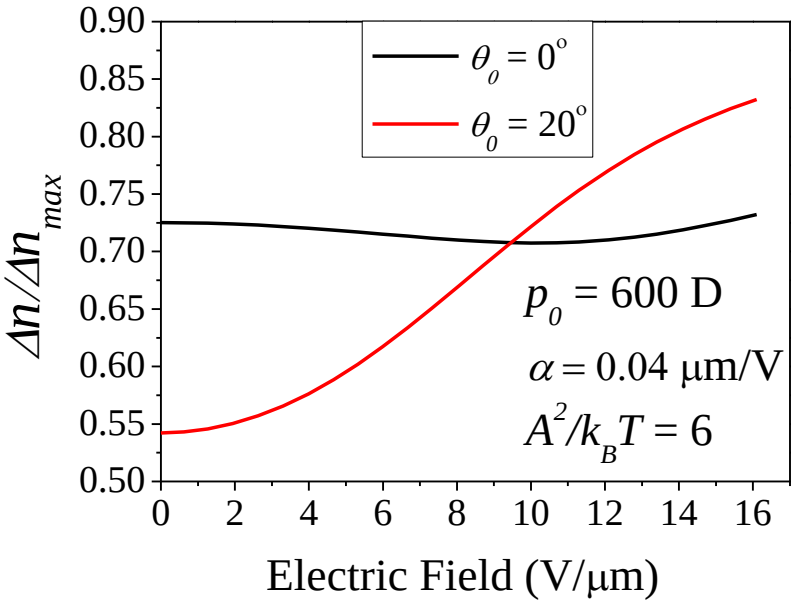

Figure 6.13 The simulated electric-field induced birefringence and the effect of θ_0 on the shape of birefringence curves, parameters p_0 , α and $A^2 / k_B T$ are fixed.

In Figure 6.13, if θ_0 = 0° then the ODF is sugarloaf-like (Figure 6.12), we surprisingly find that $\Delta n / \Delta n_{\max}$ hardly changes with ***E*** (black line). Since the experimental results [42,70,96] follow the simulated birefringence curve as shown in Figure 6.13 (red line), we can safely conclude that the volcano-like distribution is the

clear outcome from this analysis, for a set of the chosen values for $p_{0,}$ α and $A^2 / k_B T$

.

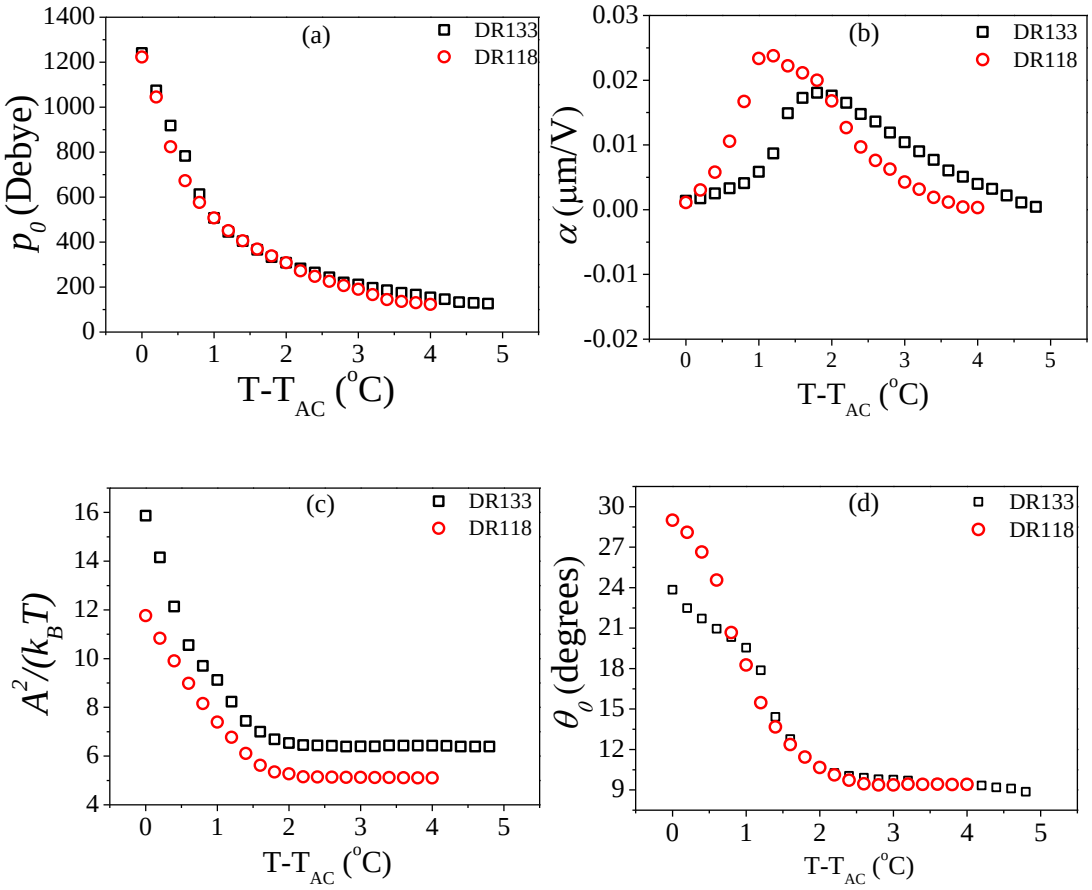

Figure 6.14 Temperature dependencies of the fitting parameters (a) the local dipole moment p_0 ; (b) the scaling factor α for the quadratic term (c) $A^2 / k_B T$ and (d) the maximum probable angle, θ_0 .

Temperature dependent variations of the fitting parameters are shown in Figure 6.14 for both DR133 (Black Squares) and DR118 (Red Circles). The local dipole moment p_0 diverges (Figure 6.14 (a)) on approaching SmA*- SmC* phase transition temperature; the divergence corresponds to an increase in the size of the tilt-correlated domain. Both $A^2 / k_B T$ (Figure 6.14 (c)) and the aperture angle $2\theta_0$ (Figure 6.14 (d)) diverge with a reduction in temperature as temperature approaches T_{AC}. From Figure 6.14 (c) we see that $A^2 / k_B T$ value is lower for DR118 compared

to DR133, the knowledge from our simulation results suggest that the molecules are tightly packed in DR118 than DR133. Also Figure 6.14 (d) shows that DR118 exhibits higher molecular tilt in the vicinity of the phase transition temperature than DR133.

De Gennes states that anisotropy of any physical quantity of a liquid crystal is an indirect measurement of its orientational order [2]. The ratio between the anisotropy in its free state (i.e. δG be the anisotropy of a physical quantity, $\delta G = G_{\parallel} - G_{\perp}$) to the anisotropy in the perfect order (ΔG) would yield us macroscopic orientational order ($S=\langle P_2 \rangle = \delta G/\Delta G$). This approach has been used for estimating S from dielectric and optical anisotropies [97,98]. A simple method to estimate the order parameter S from the birefringence measurements was given by Zywucki *et. al.* [99]. In this chapter, the principle of estimating the order parameter is similar to the above mentioned approach, Δn being the optical anisotropy and Δn_{max} being the saturated optical anisotropy. The maximum value is obtained from a temperature well within the SmC* phase with a large applied electric field, this also simplifies the need of extrapolation [100]. Then, we use the fitting parameters from the mean-field modelling namely, $A^2 / k_B T$ and θ_0 (Note: These two parameters provide the molecular long axis tilt distribution in the absence of electric field) to extract the order parameter and the plot is shown in Figure 6.15 as a function of the reduced temperature for both DR133 and DR118.

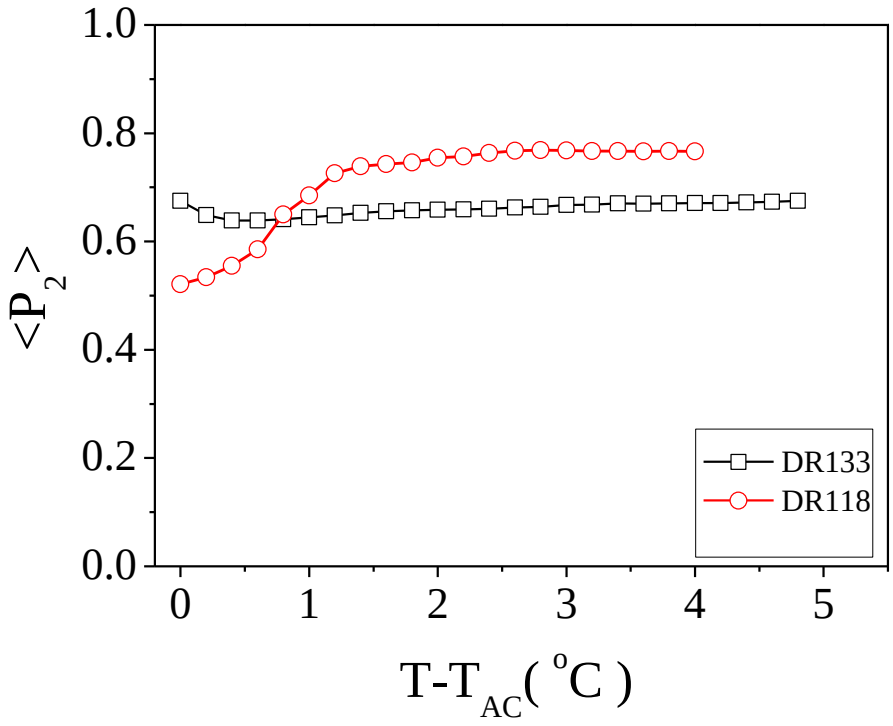

Figure 6.15 Temperature dependence order parameter <P_2> for DR133 and DR118

In the literature different techniques such as NMR [101], X-ray scattering [63,102], Raman and infrared spectroscopy [76] are used to obtain the orientational order parameters of different de Vries smectics. Raman spectroscopic measurements on a prototype de Vries smectic TSiKN65 led to <*P2*> = ~ 0.4 [76]. This is found to be rather low in magnitude for the SmA* phase. However NMR, Raman and the X-ray spectroscopic investigations of another low layer-shrinkage smectic 9HL compound yielded <P_2> as large as ~0.8, found over a wide temperature range of the SmA* phase [103]. X-ray studies of the achiral de Vries smectics C4 and C9 gave <P_2> ~0.6 [63]. Larger values of <P_2> greater than 0.6 lead to sugarloaf ODF in the SmA* phase, whereas low values of <P_2> suggest volcano-shaped ODF.

For DR133 the <P_2> ~0.67 for the temperatures close to the Iso – SmA* transition and it decreases to ~0.63 close to T=T_{AC} and for DR118 the <P_2> ~0.76 for

temperature close to the Iso – SmA* transition and it decreases to ~0.52 close to T=T_{AC}. Their decreasing tendency of the order parameter on approaching T_{AC} clearly shows the widening of the ODF, i.e. increasing the molecular tilt. Also discussed earlier, the DR118 has higher value of $\langle P_2 \rangle$ compared to DR133 suggesting dense molecular packing, at the same time close to T_{AC} DR118 shows higher tilt than DR133 as the result, the $\langle P_2 \rangle$ value of DR118 drastically drops to ~0.5.

Figure 6.16 (i) and (ii) show the 2D and 3D representations of ODF at a temperature (T_{AC} + 1) °C for DR133 and (T_{AC} + 0.6) °C for DR118, respectively. Figure 6.16 (i) is a projection of 3D ODF onto a plane normal to $\theta \cos\phi$ axis. Both figures consist of ODF obtained from different amplitudes of applied electric field. At zero electric field (Black lines) the molecules are evenly distributed with the maximum probability coinciding at a finite angle with respect to the layer normal. On applying the electric field, the molecules shift towards a favorable side (Blue lines). For higher electric fields, the distribution gets condensed to a narrow range of ϕ values leading to a single maximum in the ODF (Red lines).

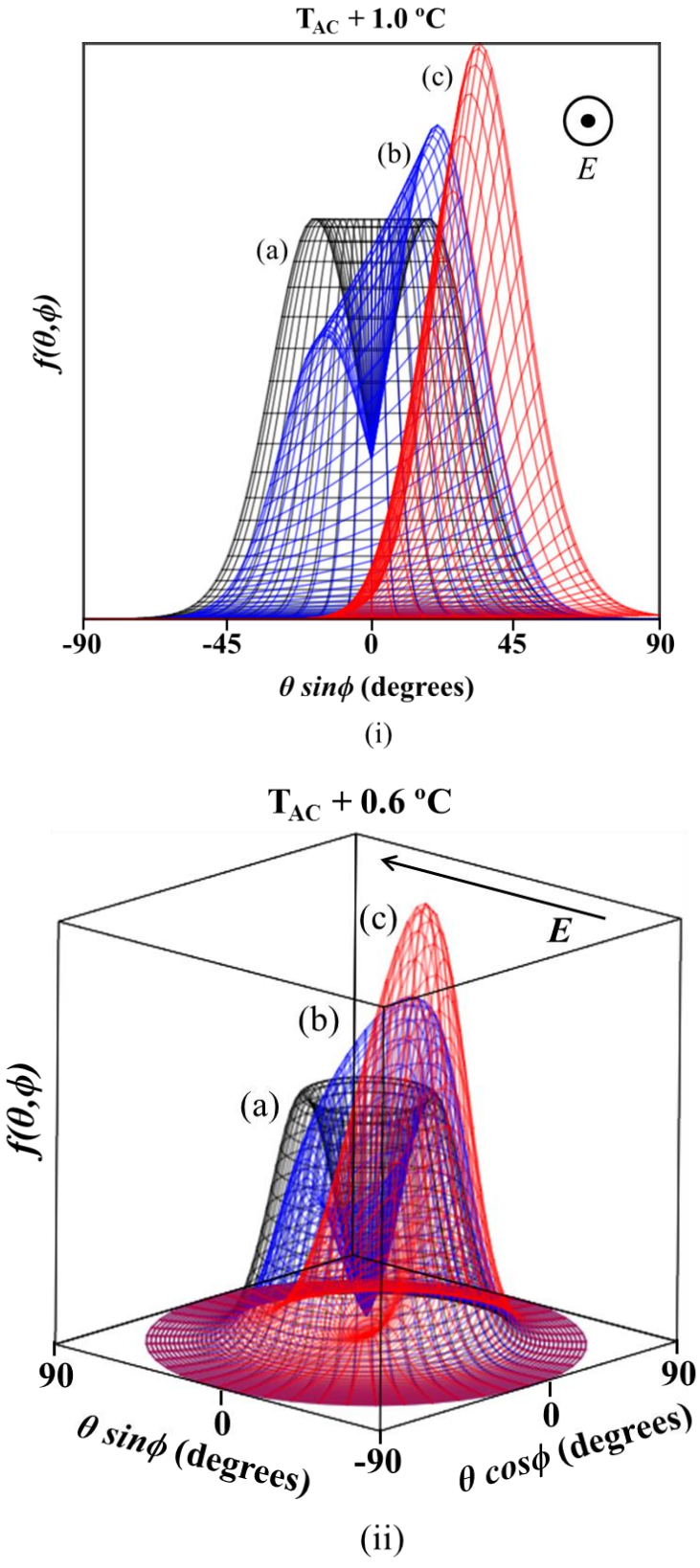

Figure 6.16 2D and 3D representations of the ODF for (i) DR133 and (ii) DR118, respectively for zero and different applied electric fields (a) 0V/µm, (b) 2V/µm and (c) 20V/µm.

Figure 6.17 and Figure 6.18 show zero field ODF from selected temperatures for DR133 and DR118 respectively. It is obvious that for temperatures close to the Iso – SmA* phase transition temperature, the distribution can be described by a single Gaussian function (i.e Sugarloaf-like) satisfactorily, the observed small depression at 0^o is due to a limitation of the model; however the depression in the ODF is negligibly small. On cooling, it is evident that the depression increases and the ODF splits into two separate Gaussian functions (*i.e.* volcano-shaped). This is observed ~2 ^oC below the Iso-SmA* transition temperature, where the contribution of θ_0 overtakes $A^2 / k_B T$ (Figure 6.19). All these factors emphasize the origin of the temperature dependencies of the molecular tilt in de Vries SmA* phase.

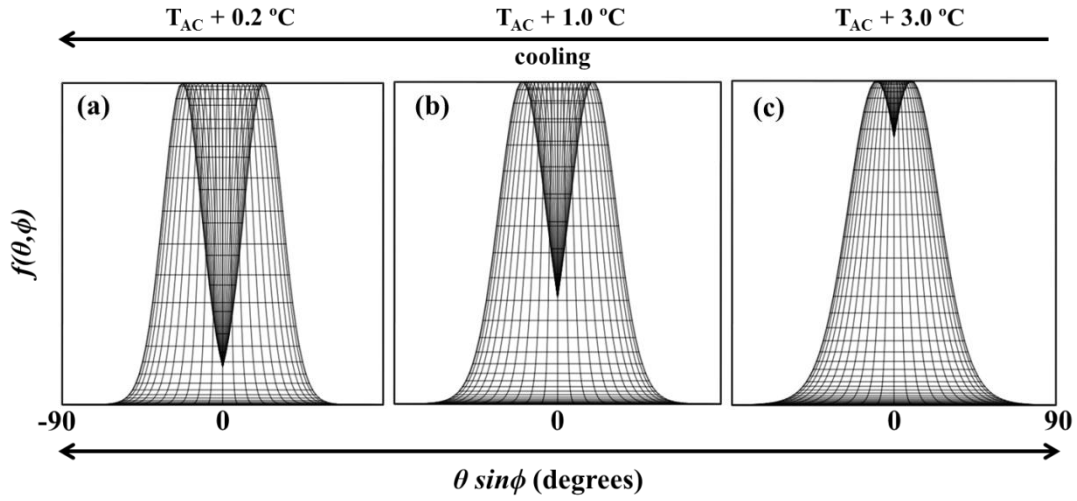

Figure 6.17 Temperature dependence of ODF for DR133 at zero electric field.

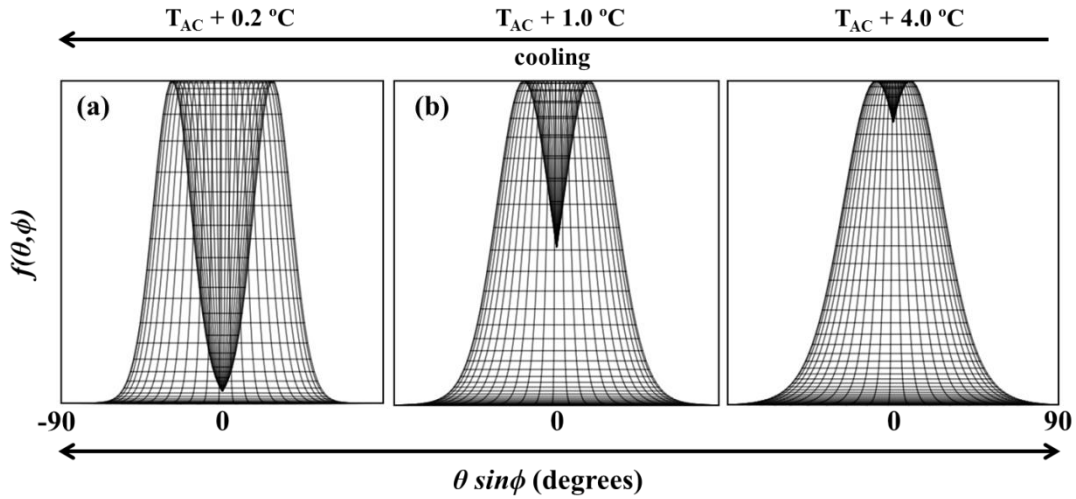

Figure 6.18 Temperature dependence of ODF for DR118 at zero electric field.

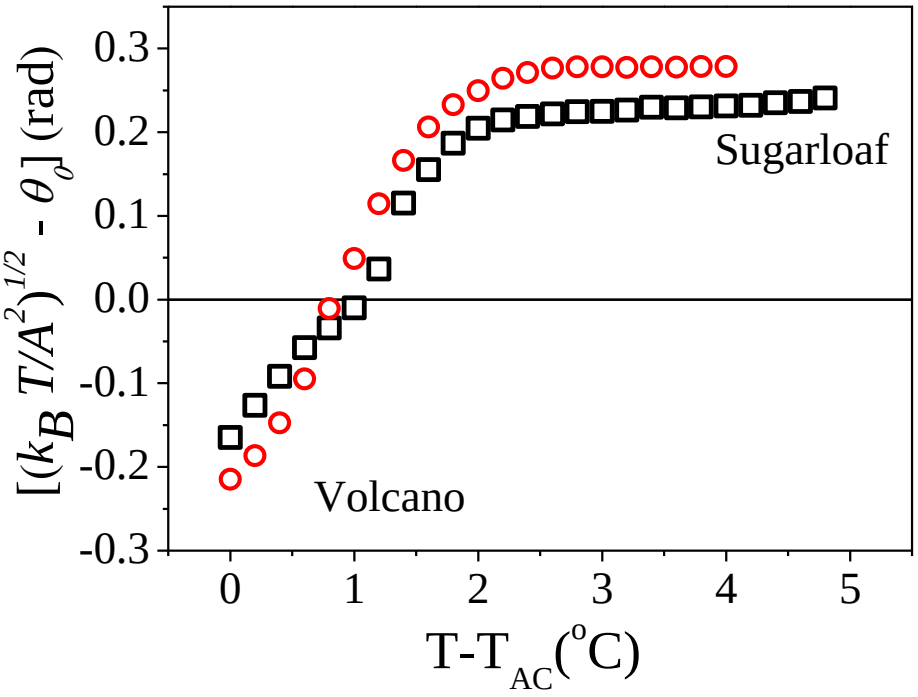

Figure 6.19 The difference between $\sqrt{k_B T}/A$ and θ_0 is plotted as a function of temperature representing the cross over between Sugarloaf and Volcano-shaped ODF for DR133 and DR118 in SmA* temperature range.

6.6 Spontaneous polarisation measurements

Figure 6.20 (a) and (b) show the measured spontaneous polarization as a function of temperature for DR133 and DR118, respectively. The measurement was carried out using the Square wave method.

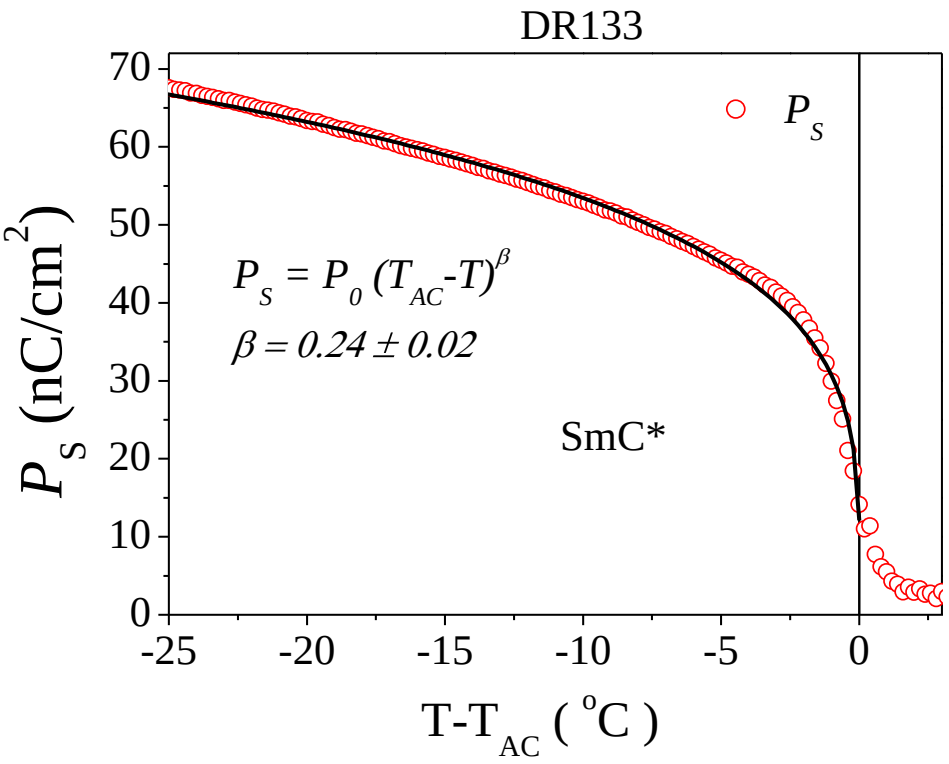

(a)

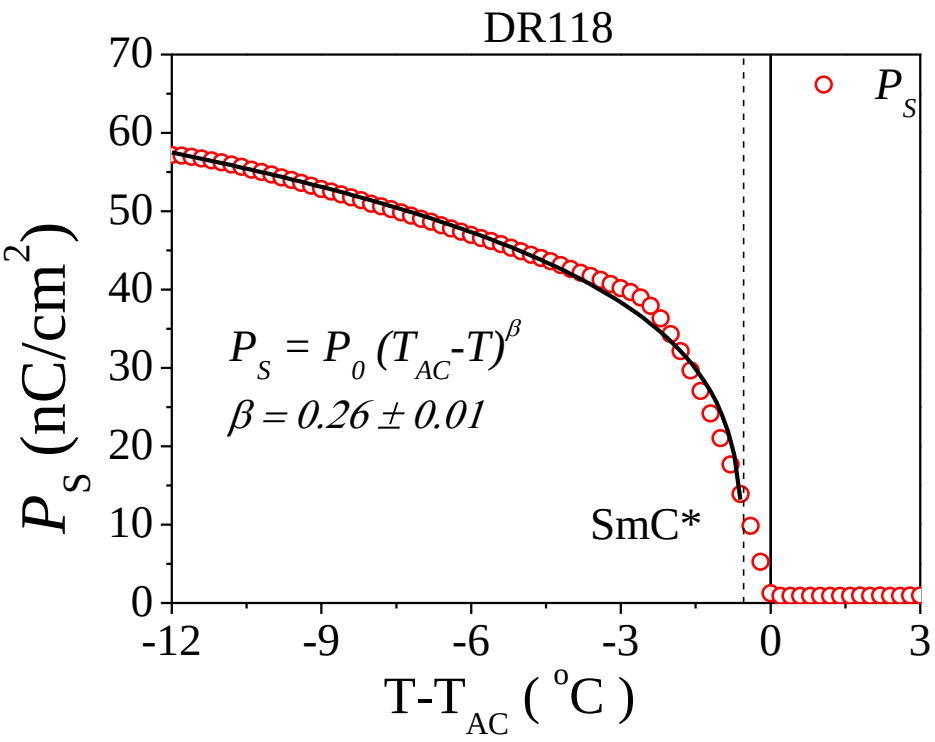

(b)

Figure 6.20 Temperature dependence of Spontaneous polarization for (a) DR133 and (b) DR118. Symbols: Experimental data; Solid line: Power law fit

DR133 shows a maximum value of $\boldsymbol{P_S}$ = 68 nC cm^{-2} for T = (T_{AC} – 25) °C and DR118 shows a maximum of $\boldsymbol{P_S}$ = 59 nC cm^{-2} for T = (T_{AC} – 12) °C. In SmC* $\boldsymbol{P_S}$ follows a power law dependence with reduced temperature as described earlier in section 4.5. The obtained values of the critical exponent for DR133 and DR118 indicate that these materials do exhibit first order SmA*-SmC* phase transition.

6.7 Unusual Phase in DR118

Here we report an unusual phase (as SmX) observed in DR118 LC below the SmC* phase and just above the crystalline phase. Figure 6.21 shows the X-ray layer thickness for the entire temperature range of DR118. On cooling from T_{AC} the layer thickness steadily increases and around 30 °C below T_{AC} we see a remarkable increasing trend in the X-ray layer thickness. Korlacki *et. al* [104] obtained similar results in 2007 and concludes that this phenomena is due to the emergence of Hexatic phase with molecular long axis parallel to the layer normal. Such a phase is given as Modulated Hexatic-B*. Few other related works can be found in the literature [105,106]. Here we label this phase as SmX, as further conclusive studies needed to find out the actual phase. Figure 6.22 shows the X-ray pattern in the low temperature region (30 °C below T_{AC}). The presence of multiple peaks shown in Figure 6.22 reflects the higher harmonics in X-ray diffraction. This implies the material exhibits high periodicity in the low temperature range.

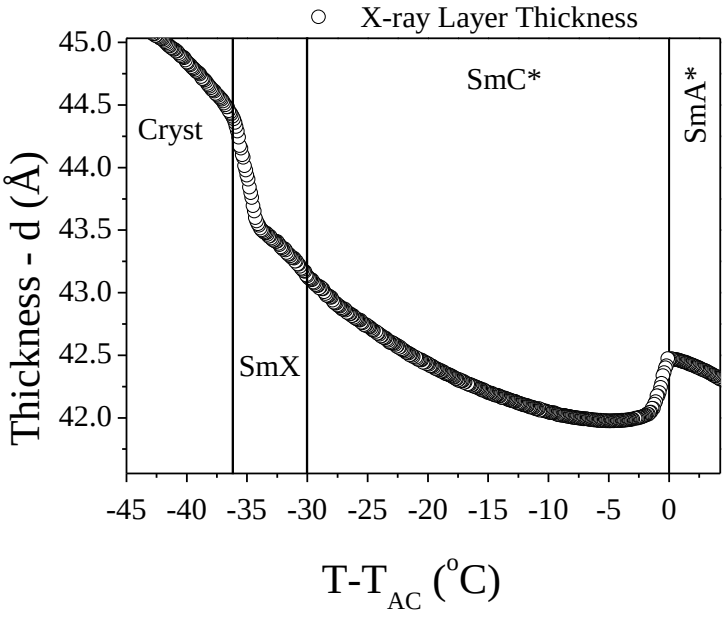

Figure 6.21 X-ray layer thickness as a function of the reduced temperature for the entire temperature range of DR118 LC.

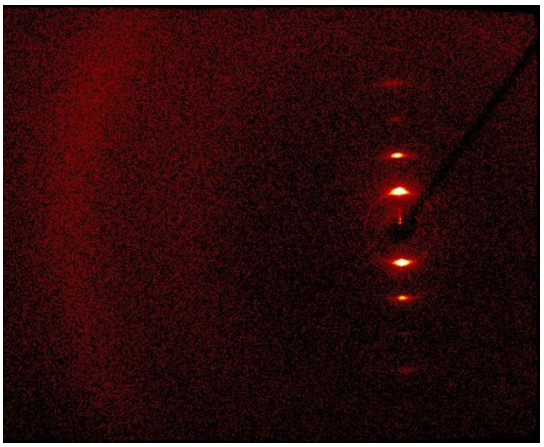

Figure 6.22 X-ray pattern obtained at 30 °C below T_{AC} showing higher harmonic peaks for DR118 LC material.

The POM image obtained from FSF of DR118 shows the presence of layer undulations before the crystalline phase on cooling. The comparison FSF images at T_{AC} and 32 °C below T_{AC} phases is shown in Figure 6.23. In Figure 6.23 (a) we observe coexistence of the phases, the dark region corresponds to the homeotropic alignment of SmA* phase and the bright schlieren texture is due to SmC* phase. Figure 6.23 (b) shows periodic strips in the FSF which possibly are due to the layer undulations [107].

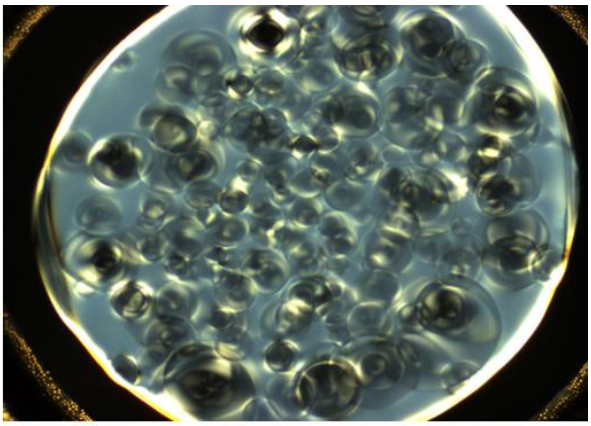

(a)

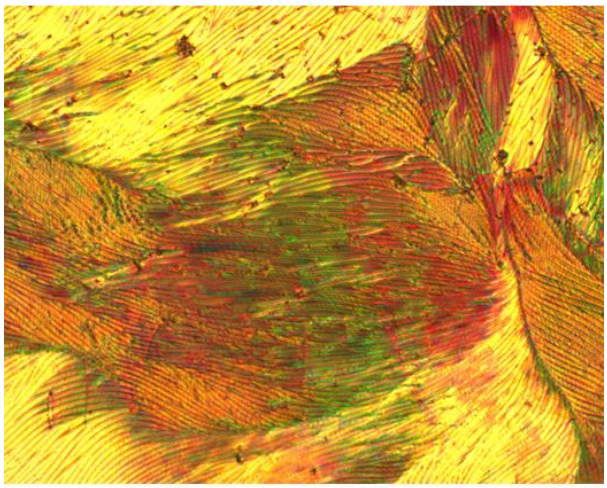

(b)

Figure 6.23 POM images obtained from DR118 FSF (a) at T_{AC} and (b) 32 °C below T_{AC}

Finally, we compare the EO response for the DR118 at different temperatures and these are shown in Figure 6.24. The EO response at 10 °C above T_{AC} is completely flat, this implies that the applied electric field does not induces any change in EO response, characteristic of conventional SmA* phase. For 1 °C above T_{AC} we can observe a prominent sigmoidal shaped response, typical for de Vries smectics LC. For 15 °C below T_{AC} in SmC* phase we see a sharp "V" shaped response with hysteresis due to bistability. However, 33 °C below T_{AC} we observe an

unusual EO response with large hysteresis. The large hysteresis could possibly be due to the high viscous nature of the unknown phase 'SmX' phase.

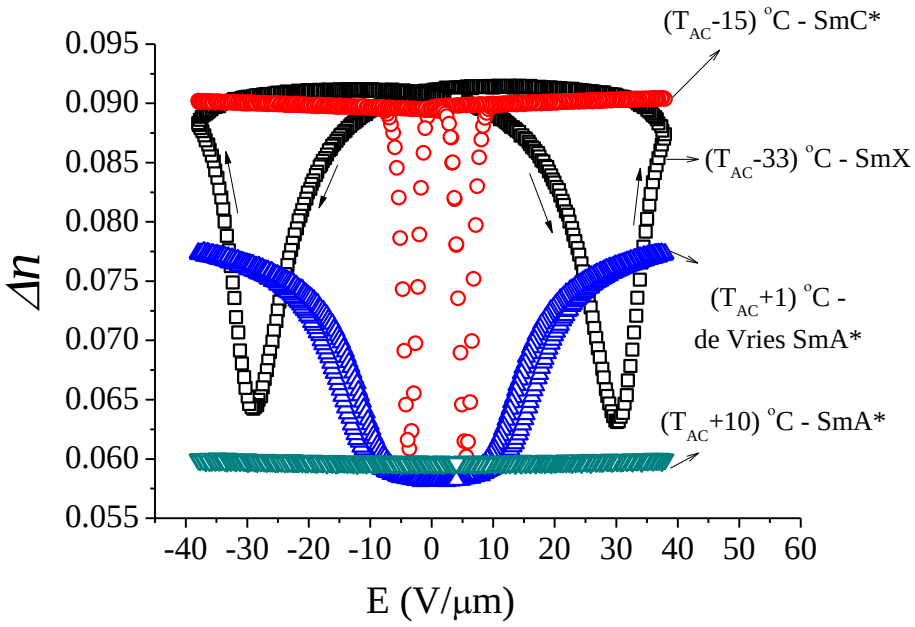

Figure 6.24 A comparison of the EO response at different temperatures for DR118.

6.8 Conclusions

Two new chiral smectic LCs DR133 and DR118 are characterised to be good de Vries smectics by using different experimental techniques. We propose a method for the FSF optical thickness to match the X-ray layer thickness data. Using this procedure we obtain the temperature dependent tilt angle that contributes to the increase in the effective refractive index of FSF. The obtained tilt angle from the procedure varies like a power law function in SmC* phase for both DR133 and DR118. Here for the first time we directly compare the EO response of a conventional smectic (Felix18/100) with de Vries smectics. The comparison clearly shows that de Vries type smectics exhibit huge EO response with large increase in

the birefringence. We also compare the EO response of DR133 at different temperatures to show distinct difference in EO response of SmA* and SmC* phases. The proposed MSLD model produces a good quality fit for both DR133 and DR118. From the EO modelling we show that de Vries smectics shows a broad sugar-loaf like distribution near the Iso phase and a wide volcano shaped distribution near T_{AC}. We also extract the order parameter from the natural ODF of DR133 and DR118. From the overall comparative studies between DR133 and DR118 LC, we make the following conclusions:

- DR133 shows higher $\boldsymbol{P_S}$ than the DR118 possibly due the presence of esterification in the mesogenic core.
- DR118 is more birefringent than DR133 due to the rigid mesogenic core.
- It is shown that the molecular packing in DR118 is more compact than DR133 from modelling results.

We report on the observation of an unusual phase in the low temperature range for DR118. From experimental results we infer that the SmX phase is highly viscous and layers undulate, as observed from POM images of a FSF.

Chapter 7

7. Conclusion and the Future Work

7.1 Conclusion and Summary

Studying and understanding the nature of chiral smectic liquid crystal is vital for the FLC based device applications. De Vries type smectic liquid crystals provide a promising path way for defect free fabrication of FLC based display. In this thesis, we have made a number of experimental and theoretical approaches to understand the anomalous nature of the de Vries type smectic LCs. A brief summary of the research work undertaken is given below:

In the first chapter we introduce the liquid crystal field of research and details about various different types of LCs. We have a given a detailed literature review of the de Vries type LCs, which emerged as an important field of research in the liquid crystal research community. In the second chapter, we have explained all the experimental methods involved to characterize the materials under concern.

In the third chapter we mainly focus on the effect of chiral doping in the achiral de Vries smectic LC. Two known de Vries type achiral materials named as C4 and C9 from a homologous series is mixed with a chiral dopant DR98S with different weight percentages. The prepared mixtures were characterized by different experimental techniques namely X-ray layer thickness, FSF optical thickness, EO and Spontaneous Polarisation. The studies from the layer thickness measurements show that by adding the chiral dopant up to 15 % w/w to the achiral host does not alter the layer thickness of the host system. On the other hand, EO and the spontaneous polarization measurements show that adding chiral dopant increases the magnitude of the response with increase in the doping concentration, making it suitable for electro-optic applications. These results show that by adding chiral dopant, the polar nature of the chiral + achiral mixture can be tailor made to the

requirements of a FLC based device while preserving the characteristic low layer shrinkage of de Vries type LCs. Also, chiral doping provides freedom to control the phase transition temperatures. By adding 20% of chiral dopant to 80% of the achiral host C4, the SmA*-SmC* phase transition is reduced by 21 °C. The field dependent EO result shows that the mixtures exhibit the characteristics of chiral de Vries type smectic LCs.

From fourth chapter onwards we present studies of chiral de Vries type LCs. We start with a well-known de Vries material MSi3MR11. MSi3MR11 is based on heptamethyltrisiloxane structure. This material exhibit direct transition to SmA* phase and shows first order SmA*-SmC* phase transition, as confirmed by DSC and POM. From X-ray layer thickness measurements we show that MSi3MR11 exhibits a maximum of 1.7% layer shrinkage and the corresponding reduction factor is 0.4. MSi_3MR11 exhibits a maximum value of $\boldsymbol{P_S}$ ~124 nC/cm^2 at 13.5 °C below T_{AC}. An anomalous trend reversal is observed in the temperature dependent FSF optical thickness and the birefringence data. The measured field dependent birefringence and apparent tilt angle show a characteristic sigmoidal shaped response near T_{AC}. The EO response data has been fitted with the GLD model proposed by Shen *et. al.* From fitting we show that the growth of the tilt correlated domain follows a power law function with critical exponent much higher than the conventional smectics. Later on we performed a detailed IR based studies for MSi3MR11 and W599. The obtained field dependent apparent tilt angle from the IR measurements is also modelled with the GLD model. From the analysis using the above model we conclude that, GLD model is quite promising in terms of reproducing the experimental EO response. This shows the advantage of the diffuse cone generalization carried out in the modelling. However, GLD model indeed has some limitation and shortcomings. The

characteristic trend reversal observed in the de Vries type smectic materials suggest that the diffuse cone angle or the θ_{min} in GLD model should also be a function of temperature in the given SmA* phase. Moreover, the artificial limiting of the molecular tilt angle to a minimum and maximum value is less physical.

In the fifth chapter, we address the above mentioned limitations of the GLD model. More over the following works are based on novel de vries smectic materials designed on the basis of the available knowledge we have so far in chemical structure of de Vries smectic LCs. In the first part we study a chiral LC DR276 a carbosilane based end tail with 5-phenyl-pyrimidine benzoate core. DR276 shows maximum layer shrinkage of ~1.9% at 10 °C below T_{AC} and the reduction factor **R** of DR276 is ~0.3. Based on the experimental results, DR276 is considered to be a good de Vries smectic material. DR276 also shows the characteristic trend reversal in the temperature dependent layer thickness and birefringence data as a function of the temperature. As a first step to improvise the EO modelling, we release the lower integration limit θ_{min} as fitting parameter for MFLD model, in order to support the speculation from the experimental results. This modification brings a good quality fit with the measured field dependent EO response. As expected the new fitting parameter 'θ_T' varies like a power law function with respect to temperature. For DR276, θ_T varies from 14º to 18º for a given temperature range in SmA* phase. As a second step on improvising the EO modelling, we propose a new MFLD model where the tilt is allowed to vary from 0 to 90° expecting a continuous ODF. Here we study another new de Vries type LC based on epoxyhexoxy backbone with 5-phenyl-pyrimidine core terminated with a tri-siloxane group named as adpc042. MFLD model is based on a Mean-Field potential consisting of a mean-field cone distribution along with the first order field dependent local dipole moment term from GLD

model. This model is used to fit the measured field dependent apparent tilt angle of adpc042. The new model produces an excellent fit with observed data. The fitting parameters obtained from the MFLD model vary like a power law function. Based on fitting results we can conclude that the de Vries type LC adpc042 the tilt-correlated domain length is estimated to be in the order of **~30nm** for temperatures close to SmA*-SmC* phase transition. We have also compared the fitting obtained from different models used for EO modelling. Figure 5.21 shows a comparison of the ODF obtained from the different models, it clearly shows that the MFLD model produces a smooth continuous diffuse cone like ODF in SmA* phase and maximum of the ODF coincides with a non-zero tilt angle.

Though MFLD model produces a continuous diffuse cone ODF for de Vries SmA* phase, the model is limited in some other attributes. First of all, the MFLD cannot work for the sigmoidal shaped EO response, as it is restricted in using only first order electric field in the Mean-Field potential. Secondly, with zero electric field molecular distribution one can estimate the order parameter of the system. The estimated order parameter $\langle P_2 \rangle$ of adpc042 from MFLD model is ~0.95 which is very high for a de Vries smectics and also for any class of LC phase. This suggests that the MFLD model overestimates the order parameter of the system which implies that the obtained ODF is very narrow.

In the sixth chapter, we modify the theoretical approach for EO model by considering the limitations in the MFLD model. In this chapter, we compare the experimental results of the two analogues chiral de Vries smectic LCs named as DR133 and DR118. Both mesogens are based on trisiloxane terminated with an alkyl spacer attached to the mesogen. The primary difference between these two compounds is the presence of esterification in the core part of DR133. As per the

results we can speculate that DR133 could form more flexible conformer's compared to DR118. Also presence of esterification increases the polar nature of the mesogen. From the X-ray layer thickness measurements we show that DR133 exhibits maximum layer shrinkage of 1.7% whereas DR118 exhibits a maximum of 1.2%. Here we propose an ad-hoc method to match the FSF optical thickness data with the X-ray layer thickness. From this procedure we estimate the number of layers in the FSF and in SmC* we can estimate the tilt causing an increase in the optical thickness compared to the X-ray layer thickness. We show that obtained tilt angle in SmC* phase varies like a power law function with an order parameter critical exponent lower than the conventional smectics. In the EO section, we compare EO response of conventional smectics (Felix 18/100) and de Vries type smectics. This comparison reveals the huge EO response of the de Vries smectics. Moreover we show that the applied electric field changes the birefringence by only 1% in conventional smectics. As a next iteration of modifying the EO modelling, we propose a new Mean-Field potential, which consists of a modified Maier-Saupe zero field distribution and field dependent Mean-Field potential from GLD model. From the simulation studies we show the importance of the parameter θ_0. MSLD model reproduces the sigmoidal shaped EO response quite well for both DR133 and DR118. The ODF shows sugar-loaf like distribution in the high temperature range in SmA* phase and a broad volcano like distribution near T_{AC}. We show that the cross-over between Sugar-loaf and Volcano shaped ODF happens around 2 °C above the $T_{AC.}$ We also report a strange phase observed in low temperature of DR118.

Overall, we emphasize the importance of diffuse cone approach in explaining the nature of the de Vries type smectic LC. From different iterations of EO modelling we clear show the origin of molecular tilt with respect to the layer normal and the

emergence of such a tilt does vary (increases) as a function of temperature on cooling in SmA* phase. The increasing tendency of the tilt splits the ODF in to two Gaussian distributions (Volcano shaped ODF) in the de Vries type SmA* phase temperature range.

7.2 Future Work

Through EO modelling we understand the molecular organization in de Vries type SmA* phase and reasons for microscopic origin of the huge EO response. However nature of the de Vries type SmA* - SmC* phase transition is still a puzzling question. The various critical exponents estimated for de Vries type smectics do not fit within the universality class of exponents proposed by de Gennes [66]. Therefore focusing on understanding the nature of the phase transition is a challenge. On the experimental side, various studies of LC systems doped with nano particles appear in the literature. This study needs to be extended to the de Vries smectics as well. A systematic study of nano doping in de Vries smectics might open new possibilities of obtaining high EO response and defect free the FLC based devices.

Appendix

A.1 Software

This section provides the list of softwares used to for the measurement and analysis of the experimental data presented in this thesis.

- **Origin® Lab (Version 7.5):** was used to for all the data analysis and graphical plot presented in this thesis
- **LabVIEW 2015:** was used to control and run the different measurement setups described in the experimental techniques
- **Maple 2015:** the mathematical software was used for the EO modelling, fitting and for all the simulations
- **Gaussian 09:** was used for the optimised geometry calculations.

A.2 Apparatus

This section provides a brief description of the main instruments used for experiments presented in this thesis.

- **Polarising optical Microscope: Olympus BX-52** (Olympus company), including the objective lens, the condenser and the microscope camera Leica DFC480 (Leica, Digital camera for microscope)
  http://www.olympusfluoview.com/brochures/pdfs/bx52.pdf
  http://www.leica-microsystems.com/
- **Optical spectrometer: Avaspec-2048** (Avantes, fast fiber optic spectrometer).
  http://www.avantes.com/

- **FTIR Spectrometer:** The system includes **FTS 6000 BIO-RAD** Infra-red spectrometer of spectral range 11,000 to 400 cm^{-1}, interchangeable KBr and quartz beam splitter.

  http://www.bio-rad.com/

A.3 EO Fitting program

This section provides the fitting program developed for the EO modelling in the thesis. The below given program is for the four parameter fitting used in the MSLD model as given in Chapter 6. The blue coloured texts are the comments indicating the functionality of that respective code.

MSLD model Program

```
> restart:
> itr:=1000:#Number of Iterations
> with(plots):
> with(Statistics):
> Digits:=12:
> ExpcsvFile := FileTools:-JoinPath( ["C:", "Users",
"swaminav", "Desktop", "vignesh documents","De
vries","clarkmodel","ClarkFourParam","Clark4Bzpo",
"Biref1up.csv"], platform = "windows" ):#Experimental
data file path
>
> ExpAlltilt:= ImportMatrix(ExpcsvFile,
source=csv):#Importing experimental data

>
>
> for nn from 1 by 1 to 28 do #Loop for multiple
temperature FIT
 tt:=ExpAlltilt[nn,1]:#Temperature
 X:= Array(ExpAlltilt[1,2..33]):#Applied Electric field
Array
 dnmax:=0.085:#Respective maximum birefringence

observedY:=(Vector(ExpAlltilt[nn,2..33]))/dnmax:#Normalis
ed Birefringence
```

```
 Biref := proc(p0, alpha, VoltArr, Dtheta,
theta0)#Birefringence Function
    kb:=1.38*(10^(-23)):
    TT:=tt+273.15:
    thetamin:=0:#Lower Integration Limit for theta
    thetamax:=3.1415965359*90/180:#Upper Integration
Limit for theta
    result:=Array(Count(VoltArr)):
    for cntr from 1 by 1 to Count(VoltArr) do#Loop for
Electric field Array
    e1:=VoltArr[cntr]:
         result(cntr):=(int((exp((-((-
p0*e1*sin(theta)*cos(phi)+Dtheta^2*(sin(theta-
theta0))^2))*(1+alpha*e1*cos(phi))/(kb*TT)))/int(exp((-
((-p0*e1*sin(theta)*cos(phi)+Dtheta^2*(sin(theta-
theta0))^2))*(1+alpha*e1*cos(phi))/(kb*TT)))*sin(theta),[
phi=0..2*3.14159265359,
theta=thetamin..thetamax]))*((cos(theta))^2-
(sin(theta))^2*(cos(phi))^2)*sin(theta),[phi=0..2*3.14159
265359,
theta=thetamin..thetamax]))/(cos(2*((0.5)*arctan((int((ex
p((-((-p0*e1*sin(theta)*cos(phi)+Dtheta^2*(sin(theta-
theta0))^2))*(1+alpha*e1*cos(phi))/(kb*TT)))/int(exp((-
((-p0*e1*sin(theta)*cos(phi)+Dtheta^2*(sin(theta-
theta0))^2))*(1+alpha*e1*cos(phi))/(kb*TT)))*sin(theta),[
phi=0..2*3.14159265359,
theta=thetamin..thetamax]))*sin(theta)*sin(2*theta)*cos(p
hi),[phi=0..2*3.14159265359,
theta=thetamin..thetamax]))/(int((exp((-((-
p0*e1*sin(theta)*cos(phi)+Dtheta^2*(sin(theta-
theta0))^2))*(1+alpha*e1*cos(phi))/(kb*TT)))/int(exp((-
((-p0*e1*sin(theta)*cos(phi)+Dtheta^2*(sin(theta-
theta0))^2))*(1+alpha*e1*cos(phi))/(kb*TT)))*sin(theta),[
phi=0..2*3.14159265359,
theta=thetamin..thetamax]))*((cos(theta))^2-
(sin(theta))^2*(cos(phi))^2)*sin(theta),[phi=0..2*3.14159
265359, theta=thetamin..thetamax])))))):
#Average Birefringence expression
    end do:
    return result:
 end proc:

 fitproc := proc(strtP0, strtAlpha, startDtheta,
starttheta0, X,observedY,stepA,stepP0,
stepDtheta,steptheta0,itr)
#Fitting Function
 with(ArrayTools):
    Yold:=Array(Count(X)):
    Ynew:=Array(Count(X)):
    sP0:=strtP0:
```

```
    sA:=strtAlpha:
    stA:=stepA:
    stP0:=stepP0:
    sDtheta:=startDtheta:
    stDtheta:=stepDtheta:
    stheta0:=starttheta0:
    sttheta0:=steptheta0:
for ctr from 0 to itr by 1 do
    Yold:=Biref(sP0, sA, X, sDtheta,stheta0):#Finding
minimum of Fitting Parameter1 : Local Dipole moment
    Ynew:=Biref(sP0+stP0, sA, X, sDtheta,stheta0):
    ChiOld:=add((Yold-observedY)*(Yold-observedY)):
    ChiNew:=add((Ynew-observedY)*(Ynew-observedY)):
    if ChiOld > ChiNew then ChiNew:=ChiOld:
sP0:=sP0+stP0:stP0:=stP0*1.1:
    else stP0:=-0.7*stP0:sP0:=sP0:ChiNew:=ChiOld:
    end if:
    Yold:=Biref(sP0, sA, X, sDtheta,stheta0):#Finding
minimum ofFitting Parameter2 : Phenomological parameter
    Ynew:=Biref(sP0, sA+stA, X, sDtheta,stheta0):
    ChiOld:=add((Yold-observedY)*(Yold-observedY)):
    ChiNew:=add((Ynew-observedY)*(Ynew-observedY)):
    if ChiOld > ChiNew then ChiNew:=ChiOld:
sA:=sA+stA:stA:=stA*1.1:
    else stA:=-0.7*stA:sA:=sA:ChiNew:=ChiOld:
    end if:
    Yold:=Biref(sP0, sA, X, sDtheta,stheta0):#Finding
minimum of Fitting Parameter3 : A^2
    Ynew:=Biref(sP0, sA, X, sDtheta+stDtheta,stheta0):
    ChiOld:=add((Yold-observedY)*(Yold-observedY)):
    ChiNew:=add((Ynew-observedY)*(Ynew-observedY)):
    if ChiOld > ChiNew then ChiNew:=ChiOld:
sDtheta:=sDtheta+stDtheta:stDtheta:=stDtheta*1.1:
    else stDtheta:=-
0.7*stDtheta:sDtheta:=sDtheta:ChiNew:=ChiOld:
    end if:
    Yold:=Biref(sP0, sA, X, sDtheta,stheta0):#Finding
minimum of Fitting Parameter4 : theta0
    Ynew:=Biref(sP0, sA, X, sDtheta,stheta0+sttheta0):
    ChiOld:=add((Yold-observedY)*(Yold-observedY)):
    ChiNew:=add((Ynew-observedY)*(Ynew-observedY)): #sum
of squares of the residuals
    if ChiOld > ChiNew then ChiNew:=ChiOld:
stheta0:=stheta0+sttheta0:sttheta0:=sttheta0*1.1:
    else sttheta0:=-
0.7*sttheta0:stheta0:=stheta0:ChiNew:=ChiOld:
    end if:

 end do:
```

```
    return array([sP0,sA,ChiNew,sDtheta,stheta0]):
 end proc:

ParamcsvFile := FileTools:-JoinPath( ["C:", "Users",
"swaminav", "Desktop", "vignesh documents","De
vries","clarkmodel","ClarkFourParam","Clark4Bzpo",
"exportparam2.csv"], platform = "windows" ):#Initial
Fitting Parameter file path
Iniparam:= ImportMatrix(ParamcsvFile, source=csv):
inip0:=Iniparam[1,1]:
inialpha:=Iniparam[1,2]:
iniDtheta:=iniparam[1,4]:#Initial values for Fitting
parameter
initheta0:=Iniparam[1,5]:


stepA1 := inialpha/100:
stepP01:= inip0/100:
stpDtheta:=iniDtheta/100:#Step for Fitting parameter
stptheta0:=initheta0/100:

fit1:= fitproc(inip0, inialpha, iniDtheta,initheta0, X,
observedY, stepA1, stepP01,stpDtheta,stptheta0,itr):#Fit1
fit2:= fitproc(fit1[1], fit1[2], fit1[4], fit1[5], X,
observedY, stepA1, stepP01,
stpDtheta,stptheta0,itr):#Fit2
fitiniplot:=Biref(inip0, inialpha, X,
iniDtheta,initheta0):
filt1plot:=Biref(fit1[1], fit1[2], X, fit1[4],fit1[5]):
filt2plot:=Biref(fit2[1], fit2[2], X, fit2[4],fit2[5]):

datab:=convert(filt2plot, Matrix):
datac:=convert(datab, matrix):
writedata[APPEND](FittedBiref3, datac, float):
dat1:=convert(fit2, Matrix):
dat3:=convert(<tt|convert(dat1, matrix)>, matrix):
writedata[APPEND](FittedParam3, dat3, float):
ExportcsvFile := FileTools:-JoinPath( ["C:", "Users",
"swaminav", "Desktop", "vignesh documents","De
vries","clarkmodel","ClarkFourParam","Clark4Bzpo","export
param2.csv"], platform = "windows" ):
Exportparam:= ExportMatrix(ExportcsvFile, dat1,
target=csv): #Saving Fitting parameters and Fitted curve

Fitini:=plot(X,fitiniplot, color=black):
Expt:= plot(X,observedY, color=blue):
Fit2:= plot(X,filt2plot, color=green):
display({Expt,Fit2,Fitini}):#Displaying Experimental and
Fitted curves.

end do:
```

A.4 FSF data correction program

This section shows the program developed for the FSF data correction with the X-ray layer thickness.

FSF data Correction

```
> restart;
> with(plots):
> with(Statistics):
> Digits:=12:
> ExpcsvFile := FileTools:-JoinPath( ["C:", "Users",
"swaminav", "Desktop","vignesh
documents","FSFCorrectionMaple","BPO", "fsfa2.csv"],
platform = "windows" ):#Experimental data file path
>
> itr:=5000:#Number of Iterations
> ExpAllFSF:= ImportMatrix(ExpcsvFile,
source=csv):#Importing experimental data
> Xaxis:= Array(ExpAllFSF[1..471,1]):#Reduced temperature
>
> RawFSF:=(Array(ExpAllFSF[1..471,3]))*10:#FSF data
before correction
> XrayY:=Array(ExpAllFSF[1..471,2]):#X-ray data
>
> thetaA:= Array(1..471):
> FSFfit:= Array(1..471):#Empty arrays
> sthetaA:= Array(0..itr):
Xaxis1:=Array(0..itr):Chi1:=Array(0..itr):ntout:=Array(0.
.itr):neffc:=Array(0..itr):
> FSFexp:=Array(ExpAllFSF[1..471,3]):#Empty arrays
> theta2:=0:#Theta at high temperature
> L:=3477.8:#Number of later guess
> no1:=1.5:
ne1:=1.586:#Refractive indices
> nt1:=
no1*ne1/sqrt(ne1^2*cos(theta2)^2+no1^2*sin(theta2)^2):#Re
fractive index as a function of theta
 neff1:= (no1 + nt1)/2:#Effective refractive index
>
>
> normFSF1:= RawFSF/L:#FSF optical thickness normalised
with number of layers
```

```
> normFSF2:=normFSF1/neff1:#FSF thickness by effective
refractive index
> H1:=plot(Xaxis,XrayY, color=black):
> G1:=plot(Xaxis,normFSF2, color=red):
> display({H1,G1}):#Plot for comparison
>
>
> theta:=0.01:#Initial theta
> for nn from 1 to 471 do#Loop for entire temperature
range
no:=1.5:
ne:=1.586:
normFSF:= 1;
sttheta:=0.0001;
ChiOld:=(XrayY[nn]-normFSF1[nn])^2;#Chi^2
for i from 0 to itr by 1 do#Loop for estimating the
optimum theta
 theta1:=theta+sttheta;
 nt:=
no*ne/sqrt(ne^2*cos(theta1)^2+no^2*sin(theta1)^2);#Fittin
g function
 neff:= (no + nt)/2;
 normFSF:= normFSF1[nn]/neff:
 ChiNew:=(XrayY[nn]-normFSF)^2:
    if ChiOld > ChiNew then
sttheta:=sttheta*1.01:theta:=theta1:ChiOld:=ChiNew:
    else sttheta:=-0.98*sttheta:ChiOld:=ChiNew:#Fitting
procedure
    end if;
sthetaA[i]:=sttheta;
Xaxis1[i]:=i;
Chi1[i]:=ChiNew;
end do:
thetaA[nn]:=theta;FSFfit[nn]:=normFSF;ntout[nn]:=nt;neffc
[nn]:=neff;


end do:
> H:=plot(Xaxis,XrayY, color=black):
> G:=plot(Xaxis,FSFexp, color=blue):
> J:=plot(Xaxis,FSFfit, color=red):
> K:=plot(Xaxis,(thetaA*180)/Pi, color=red):
> S:=plot(Xaxis,ntout, color=red):
> A:=plot(Xaxis,neffc, color=red):
>
>
> F:=plot(Xaxis1,abs(sthetaA), color=red ):
> F:=plot(Xaxis1,abs(Chi1), color=red ):
>
> display({H,J}):
> dataT:= convert(thetaA, array):
```

```
> writedata(Thetaout, dataT, float):#Saving theta values
>
> dataFSF:= convert(FSFfit, array):
> writedata(FSFfit2, dataFSF, float):#Saving corrected
FSF data
>
> dataF:= convert(normFSF2, array):
> writedata(NormFSF, dataF, float):#Saving normalised FSF
data
```

List of Publications

1. S.P Sreenilayam, D. M Agra-Kooijman, V. P. Panov, **V. Swaminathan**, J. K. Vij, Yu. P. Panarin, A. Kocot, A. Panov, D. Rodriguez-Lojo, P. J. Stevenson, Michael R. Fisch, and Satyendra Kumar. "Phase behavior and characterization of heptamethyltrisiloxane-based de Vries smectic liquid crystal by electro-optics, x rays, and dielectric spectroscopy", Phys. Rev. E **95**, 032701 (2017).
2. N. Yadav, V.P. Panov, **V. Swaminathan**, S.P. Sreenilayam, J. K. Vij, T. S. Perova, R. Dhar, A. Panov, D. Rodriguez-Lojo, and P. J. Stevenson, "Chiral smectic-A and smectic-C phases with de Vries characteristics" Phys. Rev. E **95**, 062704 (2017).
3. **V. Swaminathan**, V. P. Panov, Yu. P. Panarin, S.P. Sreenilayam, J. K. Vij, A. Panov, D. Rodriguez-Lojo, P. J. Stevenson and E. Goreka, "The effect of chiral doping in achiral smectic liquid crystals on the de Vries characteristics: smectic layer thickness, electro-optics and birefringence", Liq. Crst. **45**, 4, 513-521 (2018) DOI: 10.1080/02678292.2017.1359694
4. Kocot, J. K. Vij, T. S. Perova, K. Merkel, **V. Swaminathan**, S. P. Sreenilayam, N. Yadav, V.P. Panov, P. J. Stevenson, A. Panov, and D. Rodriguez-Lojo, "Observation of the de Vries behaviour in SmA* phase of a liquid crystal using polarised Raman scattering and infrared spectroscopy" J. Chem. Phys **147**, 094903 (2017).
5. S. P. Sreenilayam, D. Rodriguez-Lojo, V. P. Panov, **V. Swaminathan,** J. K. Vij, Yu. P. Panarin, E. Gorecka, A. Panov, and P. J. Stevenson, "Design and

investigation of de Vries liquid crystals based on 5-phenyl-pyrimidine and (R,R)-2,3-epoxyhexoxy backbone", Phys. Rev. E **96**, 042701 (2017).

6. **V. Swaminathan**, V. P. Panov, J. K. Vij, A. Kocot, A. Panov, D. Rodriguez-Lojo and P. J. Stevenson, "Orientational distribution functions and order pramameter of a chiral de Vries smectic mesogen from birefringence measurements" (Manuscript in preparation).
7. **V. Swaminathan**, V. P. Panov, J. K. Vij, S. P. Sreenilayam, Yu. P. Panarin, A. Panov, D. Rodriguez-Lojo, P. J. Stevenson and E. Gorecka, "Comparative study of two chiral de Vries type smectic mesogens" (Manuscript in preparation)
8. **V. Swaminathan,** V. P. Panov, J. K. Vij, S. P. Sreenilayam, Yu. P. Panarin, A. Panov, D. Rodriguez-Lojo, and P. J. Stevenson, "Modified Langevin-Debye model for electro-optics of de Vries type smectic liquid crystals" (Manuscript in preparation)

List of Presentations

1. **V. Swaminathan**, V. Panov, S. P. Sreenilayam, Yu. P. Panarin, J. K. Vij *et. al.* "Structure property relationship of two new chiral de Vries smectic liquid crystals" 26th International Liquid Crystal Conference, P-3-11 (Poster)
2. **V. Swaminathan**, S. P. Sreenilayam, V. Panov, Yu. P. Panarin, J. K. Vij *et. al.* "Investigations of de Vries SmA* phase and Effects of chiral doping in achiral organosiloxane mesogens" 26th International Liquid Crystal Conference, P-1-95 (Poster)

Bibliography

[1] S. Chandrasekhar, *Liquid Crystals* (Cambridge University Press, Cambridge, 1992), 2 edn.

[2] P. G. de Gennes and J. Prost, in *The Physics of Liquid Crystals* (Clarendon Press Oxford, 1993).

[3] F. Reinitzer, Monatshefte für Chemie und verwandte Teile anderer Wissenschaften **9**, 421 (1888).

[4] T. J. Sluckin, D. A. Dunmur, and H. Stegemeyer, *Crystals That Flow: Classic Papers from the History of Liquid Crystals* (Taylor & Francis, 2004).

[5] J. W. Goodby, P. J. Collings, T. Kato, C. Tschierske, H. F. Gleeson, and P. Raynes, *Handbook of liquid crystals* (Wiley, 2014).

[6] O. D. Lavrentovich and V. M. Pergamenshchik, Phys. Rev. Lett. **73**, 979 (1994).

[7] V. Borshch *et al.*, Nat. Comm. **4**, 2635 (2013).

[8] V. P. Panov, R. Balachandran, J. K. Vij, M. G. Tamba, A. Kohlmeier, and G. H. Mehl, Appl. Phys. Lett. **101**, 234106 (2012).

[9] W. D. Stevenson, Z. Ahmed, X. B. Zeng, C. Welch, G. Ungar, and G. H. Mehl, Phys. Chem. Chem. Phys. **19**, 13449 (2017).

[10] P. J. Collings and M. Hird, *Introduction to Liquid Crystals: Chemistry and Physics* (CRC Press, 1997).

[11] Iam-Choon Khoo, *Liquid Crystals, 2nd Ed,* (John Wiley and Sons, 2007).

[12] R. B. Meyer, L. Liebert, L. Strzelecki, and P. Keller, J. Phys. Lett. **36**, 69 (1975).

[13] J. W. Goodby, *Ferroelectric liquid crystals: Principles, properties, and applications* (Gordon and Breach Science Publishers, 1991).

[14] N. A. Clark and S. T. Lagerwall, Appl. Phys. Lett. **36**, 899 (1980).

[15] T. P. Rieker, N. A. Clark, G. S. Smith, D. S. Parmar, E. B. Sirota, and C. R. Safinya, Phys. Rev. Lett. **59**, 2658 (1987).

[16] J. P. F. Lagerwall and F. Giesselmann, Chem. Phys. Chem. **7**, 20 (2006).

[17] Y. Takanishi, Y. Ouchi, H. Takezoe, and A. Fukuda, Jpn. J. App.l Phys. Lett. **28**, L487 (1989).

[18] S. Kumar, Phys. Rev. A **23**, 3207 (1981).

[19] C. R. Safinya, R. J. Birgeneau, J. D. Litster, and M. E. Neubert, Phys. Rev. Lett. **47**, 668 (1981).

[20] S. Diele, P. Brand, and H. Sackmann, Mol. Cryst. Liq. Cryst. **16**, 105 (1972).

[21] A. de Vries, Mol. Cryst. Liq. Cryst. **41**, 27 (1977).

[22] Y. P. Panarin, V. Panov, O. E. Kalinovskaya, and J. K. Vij, J. Mater. Chem. **9**, 2967 (1999).

[23] A. J. Leadbetter and E. K. Norris, Mol. Phys. **38**, 669 (1979).

[24] A. de Vries, J. Chem. Phys. **71**, 25 (1979).

[25] A. de Vries, A. Ekachai, and N. Spielberg, Mol. Cryst. Liq. Cryst. **49**, 143 (1979).

[26] A. Devries, A. Ekachai, and N. Spielberg, Mol. Cryst. Liq. Cryst. **49**, 143 (1979).

[27] D. M. Walba *et al.*, J. Soc. Inf. Disp. **15**, 585 (2007).

[28] N. Kapernaum, D. M. Walba, E. Korblova, C. Zhu, C. Jones, Y. Shen, N. A. Clark, and F. Giesselmann, Chem. Phys. Chem. **10**, 890 (2009).

[29] N. Shin-ichi, O. Yukio, T. Hideo, and F. Atsuo, Jap. J. App. Phys. **26**, L1787 (1987).

[30] J. P. F. Lagerwall, F. Giesselmann, and M. D. Radcliffe, Phys. Rev. E **66**, 031703 (2002).

[31] M. S. Spector, P. A. Heiney, J. Naciri, B. T. Weslowski, D. B. Holt, and R. Shashidhar, Phys. Rev. E **61**, 1579 (2000).

[32] C. C. Huang, S. T. Wang, X. F. Han, A. Cady, R. Pindak, W. Caliebe, K. Ema, K. Takekoshi, and H. Yao, Phys. Rev. E **69**, 041702 (2004).

[33] C. V. Lobo, S. K. Prasad, and D. S. Rao, Phys. Rev. E **72**, 062701 (2005).

[34] U. Manna, J. K. Song, Y. P. Panarin, A. Fukuda, and J. K. Vij, Phys. Rev. E **77**, 041707 (2008).

[35] M. Skarabot, M. Cepic, B. Zeks, R. Blinc, G. Heppke, A. V. Kityk, and I. Musevic, Phys. Rev. E **58**, 575 (1998).

[36] M. Skarabot, K. Kocevar, R. Blinc, G. Heppke, and I. Musevic, Phys. Rev. E **59**, R1323 (1999).

[37] J. C. Roberts, N. Kapernaum, Q. Song, D. Nonnenmacher, K. Ayub, F. Giesselmann, and R. P. Lemieux, J. Am. Chem. Soc. **132**, 364 (2010).

[38] C. Bahr and G. Heppke, Phys. Rev. A **41**, 4335 (1990).

[39] K. Saunders, Phys. Rev. E **80**, 011703 (2009).

[40] K. C. Lim and J. T. Ho, Phys. Rev. Lett. **40**, 1576 (1978).

[41] N. A. Clark *et al.*, Appl. Phys. Lett. **80**, 4097 (2002).

[42] Y. Q. Shen, L. X. Wang, R. F. Shao, T. Gong, C. H. Zhu, H. Yang, J. E. Maclennan, D. M. Walba, and N. A. Clark, Phys. Rev. E **88**, 062504 (2013).

[43] Z. V. Kost-Smith, P. D. Beale, N. A. Clark, and M. A. Glaser, Phys. Rev. E **87**, 050502 (2013).

[44] K. Merkel, A. Kocot, J. K. Vij, P. J. Stevenson, A. Panov, and D. Rodriguez, Appl. Phys. Lett. **108**, 5, 243301 (2016).

[45] M. V. Gorkunov, F. Giesselmann, J. P. F. Lagerwall, T. J. Sluckin, and M. A. Osipov, Phys. Rev. E **75**, 060701 (2007).

[46] M. V. Gorkunov, M. A. Osipov, J. P. F. Lagerwall, and F. Giesselmann, Phys. Rev. E **76**, 051706 (2007).

[47] M. Osipov and G. Pajak, Phys. Rev. E **85**, 021701 (2012).

[48] M. A. Osipov, M. V. Gorkunov, H. F. Gleeson, and S. Jaradat, Eur Phys J E Soft Matter **26**, 395 (2008).

[49] O. Francescangeli *et al.*, Adv. Funct. Mater. **19**, 2592 (2009).

[50] B. Park, S. S. Seomun, M. Nakata, M. Takahashi, Y. Takanishi, K. Ishikawa, and H. Takezoe, Jpn. J. Appl. Phys. **38**, 1474 (1999).

[51] S. Huard, *Polarization of Light* (Wiley, 1997).

[52] V. M. V. a. Y. P. Panarin, Mol. Mater. **1**, 147 (1992).

[53] V. Panov, J. K. Vij, and N. M. Shtykov, Liq. Cryst. **28**, 615 (2001).

[54] L. A. Beresnev, L. M. Blinov, M. A. Osipov, and S. A. Pikin, Mol. Cryst. Liq. Cryst. **158**, 3 (1988)

[55] W. Kuczyński and H. Stegemeyer, Chem. Phys. Lett. **70**, 123 (1980) and H. Stegemeyer, A. Sprick, M. A. Osipov, V. Vill and H. W. Tunger, Phys. Rev. E **56,** 5721 (1995).

[56] L. A. Beresnev and L. M. Blinov, Ferroelectrics **33**, 129 (1981).

[57] L. A. Beresnev, L. M. Blinov, V. A. Baikalov, E. P. Pozhidayev, G. V. Purvanetskas, and A. I. Pavluchenko, Mol. Cryst. Liq. Cryst. **89**, 327 (1982).

[58] L. A. Beresnev, E. P. Pozhidaev, L. M. Blinov, A. I. Pavlyuchenko, and N. B. Etingen, Jetp. Lett. **35**, 531 (1982).

[59] G. C. a. L. N. Lisetskii, Usp. Fiz. Nauk. **134**, 279 (1981).

[60] H. S. Chang, S. Jaradat, H. F. Gleeson, I. Dierking, and M. A. Osipov, Phys. Rev. E **79**, 061706 (2009).

[61] V. Swaminathan, V. P. Panov, Y. P. Panarin, S. P. Sreenilayam, J. K. Vij, A. Panov, D. Rodriguez-Lojo, P. J. Stevenson, and E. Gorecka, Liq. Crst. **45**, 4, 513-521 (2018) DOI: 10.1080/02678292.2017.1359694

[62] D. M. Agra-Kooijman, H. Yoon, S. Dey, and S. Kumar, Phys. Rev. E **89**, 032506 (2014).

[63] H. Yoon, D. M. Agra-Kooijman, K. Ayub, R. P. Lemieux, and S. Kumar, Phys. Rev. Lett. **106**, 087801 (2011).

[64] M. D. Radcliffe, M. L. Brostrom, K. A. Epstein, A. G. Rappaport, B. N. Thomas, R. F. Shao, and N. A. Clark, Liq. Cryst. **26**, 789 (1999).

[65] V. P. Panov, J. K. Vij, Y. P. Panarin, C. Blanc, V. Lorman, and J. W. Goodby, Phys. Rev. E **75**, 042701 (2007).

[66] P. G. de Gennes, Mol. Cryst. Liq. Cryst. **21**, 49 (1973).

[67] Y. P. Panarin, O. E. Panarina, and J. K. Vij, Ferroelectrics **310**, 261 (2004).

[68] Y. P. Panarin, F. Antonelli, O. E. Panarina, Y. Semenova, J. K. Vij, M. Reihmann, and G. Galli, Ferroelectrics **310**, 255 (2004).

[69] K. L. Sandhya, Y. P. Panarin, V. P. Panov, J. K. Vij, and R. Dabrowski, Eur. Phys. J. E **27**, 397 (2008).

[70] J. V. Selinger, P. J. Collings, and R. Shashidhar, Phy. Rev. E **64**, 061705 (2001).

[71] R. Z. Qiu, J. T. Ho, and S. K. Hark, Phys. Rev. A **38**, 1653 (1988).

[72] F. Giesselmann, P. Zugenmaier, I. Dierking, S. T. Lagerwall, B. Stebler, M. Kaspar, V. Hamplova, and M. Glogarova, Phys. Rev. E **60**, 598 (1999).

[73] S. Garoff and R. B. Meyer, Phys. Rev. Lett. **38**, 848 (1977).

[74] S. Garoff and R. B. Meyer, Phys. Rev. A **19**, 338 (1979).

[75] N. A. Clark and S. T. Lagerwall, Appl. Phys. Lett. **36**, 899 (1980).

[76] N. Hayashi, T. Kato, A. Fukuda, J. K. Vij, Y. P. Panarin, J. Naciri, R. Shashidhar, S. Kawada, and S. Kondoh, Phys. Rev. E **71**, 041705 (2005).

[77] U. Manna, R. M. Richardson, A. Fukuda, and J. K. Vij, Phys. Rev. E **81**, 050701 (2010).

[78] O. E. Panarina, Y. P. Panarin, F. Antonelli, J. K. Vij, M. Reihmann, and G. Galli, J. Mater. Chem. **16**, 842 (2006).

[79] O. E. Panarina, Y. P. Panarin, J. K. Vij, M. S. Spector, and R. Shashidhar, Phys. Rev. E **67**, 051709 (2003).

[80] G. Galli, M. Reihmann, A. Crudeli, E. Chiellini, Y. Panarin, J. Vij, C. Blanc, V. Lorman, and N. Olsson, Mol. Cryst. Liq. Cryst. **439**, 2111 (2005).

[81] M. J. Frisch *et al.,* GAUSSIAN 09, *Revision E.01* (Gaussian, Inc., Wallingford, CT, 2009)

[82] A. Mochizuki and S. Kobayashi, Mol. Cryst. Liq. Cryst. **243**, 77 (1994).

[83] A. P. Hammersley, S. O. Svensson, M. Hanfland, A. N. Fitch, and D. Hausermann, High Pressure Research **14**, 235 (1996).

[84] K. Saunders, D. Hernandez, S. Pearson, and J. Toner, Phys. Rev. Lett. **98**, 197801 (2007).

[85] P. J. Collings, B. R. Ratna, and R. Shashidhar, Phys. Rev. E **67**, 021705 (2003).

[86] S. Inui, N. Iimura, T. Suzuki, H. Iwane, K. Miyachi, Y. Takanishi, and A. Fukuda, J. Mater. Chem. **6**, 671 (1996).

[87] P. Rudquist *et al.,* J. Mater. Chem. **9**, 1257 (1999).

[88] N. Yadav *et al.,* Phys. Rev. E **95**, 9, 062704 (2017).

[89] A. Kocot, R. Wrzalik, B. Orgasinska, T. Perova, J. K. Vij, and H. T. Nguyen, Phys. Rev. E **59**, 551 (1999).

[90] A. Kocot, G. Kruk, R. Wrzalik, and J. K. Vij, Liq. Cryst. **12**, 1005 (1992).

[91] A. A. Sigarev, J. K. Vij, Y. P. Panarin, P. Rudquist, S. T. Lagerwall, and G. Heppke, Liq. Cryst. **30**, 149 (2003).

[92] K. Merkel, A. Kocot, J. K. Vij, G. H. Mehl, and T. Meyer, J. Chem. Phys. **121**, 5012 (2004).

[93] S. P. Sreenilayam, D. Rodriguez-Lojo, D. M. Agra-Kooijman, J. K. Vij, V. P. Panov, A. Panov, M. R. Fisch, S. Kumar, and P. J. Stevenson, Phys. Rev. Mater. **2**, 025603 (2018).

[94] S. P. Sreenilayam, D. Rodriguez-Lojo, V. P. Panov, V. Swaminathan, J. K. Vij, Y. P. Panarin, E. Gorecka, A. Panov, and P. J. Stevenson, Phys. Rev. E **96**, 042701 (2017).

[95] V. P. Panov, S. S. Seomun, N. M. Shtykov, J. K. Vij, and H. T. Nguyen, Ferroelectrics **278**, 619 (2002).

[96] S. P. Sreenilayam *et al.*, Phys. Rev. E **95** (2017).

[97] W. H. d. Jeu and P. Bordewijk, J. Chem. Phys. **68**, 109 (1978).

[98] E. G. Hanson and Y. R. Shen, Mol. Cryst. Liq. Cryst. **36**, 193 (1976).

[99] W. K. B. Zywucki, and G. Czechowski in *Proceedings of SPIE, Liquid Crystals: Material Science and Applications*1995).

[100] I. Haller, H. A. Huggins, H. R. Lilienthal, and T. R. McGuire, J. Phys. Chem. **77**, 950 (1973).

[101] A. Marchetti, V. Domenici, V. Novotna, M. Lelli, M. Cifelli, A. Lesage, and C. A. Veracini, Chem. Phys. Chem **11**, 1641 (2010).

[102] P. Davidson, D. Petermann, and A. M. Levelut, Journal De Physique Ii **5**, 113 (1995).

[103] A. Sanchez-Castillo, M. A. Osipov, S. Jagiella, Z. H. Nguyen, M. Kaspar, V. Hamplova, J. Maclennan, and F. Giesselmann, Phys. Rev. E **85**, 061703 (2012).

[104] R. Korlacki, A. Fukuda, and J. K. Vij, Euro. Phys. Lett. **77**, 36004 (2007).

[105] Y. Ouchi, Y. Yoshioka, H. Ishii, K. Seki, M. Kitamura, R. Noyori, Y. Takanishi, and I. Nishiyama, J. Mater. Chem. **5**, 2297 (1995).

[106] S. S. Seomun, Y. Takanishi, K. Ishikawa, H. Takezoe, A. Fukuda, C. Tanaka, T. Fujiyama, T. Maruyama, and S. Nishiyama, Mol. Cryst. Liq. Cryst. **303**, 181 (1997).

[107] K. Harth, B. Schulz, C. Bahr, and R. Stannarius, Soft Matter **7**, 7103 (2011).